Università degli Studi di Napoli “Federico II”

Scuola Politecnica e delle Scienze di Base
Area Didattica di Scienze Matematiche Fisiche e Naturali

Dipartimento di Fisica “Ettore Pancini”

Laurea Magistrale in Fisica

Measurement of the CKM matrix elements $|V_{tb}|$, $|V_{ts}|$, and $|V_{td}|$ using single top quark events in proton-proton collisions at 13 TeV with the CMS experiment at the LHC

Relatore:
Dott. Alberto Orso Maria Iorio
Dott. Luca Lista
Correlatore:
Dott. Francesco Tramontano

Candidato:
Agostino De Iorio
Matricola N94/292

A.A. 2016/2017

To my family

Contents

Introduction

The Large Hadron Collider is a circular accelerator designed to provide proton-proton collisions with a luminosity of 10^{34} $\mathrm{cm}^{-2}\mathrm{s}^{-1}$ and a centre-of-mass energy of $\sqrt{s} = 14$ TeV. The LHC is equipped with four main experiments: ALICE, ATLAS, CMS, and LHCb. The aim of LHC is to provide further proofs on the validity of the Standard Model of Particle Physics and to give clues of new physics at the TeV scale.
The Standard Model of Particles Physics is the current framework in which the electroweak and strong interactions successfully find explanation. It is verified with high precision for most processes involving elementary particles and all particles foreseen by the SM have been now been discovered, with the Higgs having been found at the LHC in 2012. One of the most important particle in the Standard Model is the top quark.
The top quark is the most massive elementary particle ever discovered. For this reason it plays a special role in precision tests of the Standard Model. However it has a very short lifetime: the decay occurs before it can hadronise. So most of the top quark properties can be directly inferred from the top quark decay products, as if it was a free particle. Another notable feature of top quark physics is that a distinct hierarchy can be identified in top quark decays: it almost totally decays in a W boson and a b quark. Nevertheless decay modes in a W boson and a d or s quarks are allowed but they are so suppressed that up to now are never been studied directly. This feature stems from the fact that there is a distinct preference of top quarks for couplings with b quarks via electroweak charged current interactions. Through the study of top quark decays and electroweak couplings it is possible to extract the magnitude of the Cabibbo-Kobayashi-Maskawa matrix elements, which are other important parameters of the Standard Model to be determined. The main mechanisms for electroweak charged current production of single top quarks is the t-channel.
The aim of the present thesis work is the first direct measurement of the Cabibbo-Kobayashi-Maskawa matrix elements $|\mathrm{V_{tb}}|$, $|\mathrm{V_{ts}}|$ and $|\mathrm{V_{td}}|$ in single top quark t-channel events. The data analysed correspond to an integrated luminosity of 35.89 fb^{-1} in

proton-proton collisions with a centre-of-mass energy of $\sqrt{s} = 13$ TeV collected with the CMS experiment at the LHC during 2016.
The present thesis is organized in five chapters:
Chapter 1 briefly introduces the Standard Model of elementary particles.
Chapter 2 presents a detailed description of the LHC accelerator machine and of the CMS detector.
Chapter 3 presents the theoretical and experimental state of the art concerning the top quark physics.
Chapter 4 is concerning with definition, selection and reconstruction of the physical objects used for the analysis.
Chapter 5 is focused on the detailed description of the analysis set up for the measurements of the CKM matrix elements $|V_{tb}|$, $|V_{ts}|$ and $|V_{td}|$ in single-top t-channel events.

Chapter 1

The Standard Model of particle physics

1.1 Overview

The Standard Model (SM) of particle physics is an $SU(3)_{col} \otimes SU(2)_{is} \otimes U(1)_y$ quantum field theory that describes three of the four known fundamental interactions in a single model. Its development began in 1961 from the effort of Sheldon Glashow [1] in unifying the electromagnetic and weak interactions, carried on in 1967 by Steven Weinberg [2] and Abdus Salam [3] with the inclusion of the Higgs mechanism [4–6]. Glashow, Weinberg and Salam won the Nobel Prize in Physics in 1979 "for their contributions to the theory of the unified weak and electromagnetic interaction between elementary particles, including, inter alia, the prediction of the weak neutral current". Over the years, the SM received other contributions aimed at the inclusion of the strong interaction in the Glashow, Weinberg and Salam framework. The quantum field theory of the strong interaction is called quantum chromodynamics (QCD) and it was developed during the 60s and 70s by Murray Gell-Mann and George Zweig [7], who suggested the existence of quarks with different flavours, and Moo-Young Han with Yoichiro Nambu [8] and Oscar W. Greenberg [9], who suggested the existence of a new quantum number called *colour* introducing so the $SU(3)_{col}$ symmetry. The SM reached its present form when, in 1973, David Politzer [10] and David Gross together with Frank Wilczek [11] suggested the theory of the asymptotic freedom of strong interaction.

The main predictions of the SM were confirmed by measurements performed throughout the years, which notably include the discovery of the three massive bosons (W^+, W^- and Z) at CERN in 1983 by the UA1 and UA2 experiments [12–14], the discov-

ery of the top quark at Tevatron in 1994 by the D0 and CDF experiments [15], and finally the discovery of the Higgs boson at CERN in 2012 by the ATLAS and CMS experiments [16, 17]. Thanks also to those compelling experimental evidences the SM is widely accepted by the scientific community as the main model to describe fundamental interactions in particle physics. The SM is however not sufficient to provide a full picture of the known universe, as it fails to explain several phenomena, like the evidence for neutrino masses, dark energy and dark matter.

1.2 Particles in Standard Model

The SM treats both matter and force fields with the same formalism, since interactions are themselves regarded as mediated by particles. Particles in the SM are divided in fermions and bosons. Fermions have half-integer spin and obey the Fermi-Dirac statistics, while bosons have integer spin and obey the Bose-Einstein statistics. Fundamental matter particles in SM are categorized as either quarks or leptons, which are divided into three families with different properties. Each family, or generation, is a doublet of particles associated to an isospin quantum number.

Leptons are fermions of spin 1/2 which carry electromagnetic and weak charges. The three generations of leptons are listed in Table 1.1.

Particles			Spin	Charge
$\begin{pmatrix}\nu_e\\ e\end{pmatrix}$	$\begin{pmatrix}\nu_\mu\\ \mu\end{pmatrix}$	$\begin{pmatrix}\nu_\tau\\ \tau\end{pmatrix}$	1/2	$\begin{matrix}0\\ -1\end{matrix}$

Table 1.1: Standard Model leptons.

Quarks are fermions of spin 1/2 which carry electromagnetic, weak and strong charges. In nature six different types, or flavours, of quarks exist and they are named as: up, down, charm, strange, top and bottom. Quarks are grouped into the three generations as listed in Table 1.2. For all fermions, an antifermion is present with the

Particles			Spin	Charge
$\begin{pmatrix}\mathrm{u}\\ \mathrm{d}\end{pmatrix}$	$\begin{pmatrix}\mathrm{c}\\ \mathrm{s}\end{pmatrix}$	$\begin{pmatrix}\mathrm{t}\\ \mathrm{b}\end{pmatrix}$	1/2	$\begin{matrix}2/3\\ -1/3\end{matrix}$

Table 1.2: Standard Model quarks.

same mass and opposite quantum numbers. Each interaction described by the SM is associated to a boson multiplet, whose components are referred to as mediators for the

Interaction	Mediators	Spin	Charge
Electromagnetic	γ	1	0
Weak	W^+, W^-, Z	1	$1, -1, 0$
Strong	8 gluons (g)	1	0

Table 1.3: Standard model mediator bosons and fundamental interactions.

interaction, and to an absolutely conserved quantum number. The SM bosons are listed in Table 1.3.

1.3 Quantum electrodynamics

Quantum electrodynamics (QED) is the quantum field theory of the electromagnetic interaction. The Lagrangian density for the QED can be obtained starting from the free Lagrangian density of the Dirac field ψ:

$$\mathcal{L}_D = i\bar{\psi}\gamma^\mu\partial_\mu\psi - m\bar{\psi}\psi, \tag{1.1}$$

where the first is the kinetic term and the last is a mass term. In particular m is the fermion mass parameter, γ^μ are the Dirac matrices and ψ and $\bar{\psi}$ are the 4-components spinor and its adjoint, respectively. ψ can be written in term of its chiral components as:

$$\psi = \begin{pmatrix} \psi_R \\ \psi_L \end{pmatrix}$$

The free Lagrangian density of the electromagnetic field is:

$$\mathcal{L}_\gamma = -\frac{1}{4}F^{\mu\nu}F_{\mu\nu}, \tag{1.2}$$

where $F^{\mu\nu}$ is the field strength tensor and can be written in terms of the vector potential A^μ as:

$$F^{\mu\nu} = -F^{\nu\mu} = \partial^\mu A^\nu - \partial^\nu A^\mu. \tag{1.3}$$

So the free Lagrangian density for QED can be obtained by adding 1.1 and 1.2:

$$\mathcal{L}^0_{QED} = \mathcal{L}_\gamma + \mathcal{L}_D = i\bar{\psi}\gamma^\mu\partial_\mu\psi - m\bar{\psi}\psi - \frac{1}{4}F^{\mu\nu}F_{\mu\nu}. \tag{1.4}$$

This Lagrangian density describes the kinematics of a non-interacting fermion in an electromagnetic field and it is globally invariant under a $U(1)_q$ transformation:

$$\psi \to \psi' = e^{i\theta}\psi \tag{1.5}$$

but it does not extend in any way the theory. Instead by imposing the locally invariance under the transformation $U(1)_q$ one obtains:

$$\psi \to \psi' = e^{i\theta(x)}\psi, \tag{1.6}$$

where this time the parameter $\theta(x)$ depends on space-time coordinates. This causes an interaction term to arise:

$$\mathcal{L}_{int} = -q\bar{\psi}\gamma^\mu A_\mu \psi = -J^\mu A_\mu. \tag{1.7}$$

This term can be re-absorbed by a redefinition of the standard derivative with the covariant derivative defined as:

$$D_\mu \equiv \partial_\mu - iqA_\mu \tag{1.8}$$

in a way to re-establish the entire invariance of the Lagrangian density. Finally the Lagrangian density for the QED is:

$$\begin{aligned} \mathcal{L}_{QED} &= i\bar{\psi}(\not{D} - m)\psi - \frac{1}{4}F^{\mu\nu}F_{\mu\nu} = \\ &= i\bar{\psi}\gamma^\mu\partial_\mu\psi - m\bar{\psi}\psi - \frac{1}{4}F^{\mu\nu}F_{\mu\nu} - q\bar{\psi}\gamma^\mu A_\mu\psi, \end{aligned} \tag{1.9}$$

where $\not{D} = \gamma^\mu D_\mu$ and the fields transform, under the gauge transformation, as:

$$A_\mu \to A_\mu - \frac{1}{q}\partial_\mu\theta(x) \qquad \psi \to e^{-i\theta(x)}\psi. \tag{1.10}$$

1.4 The Electroweak theory

The original description of the weak interaction, due to Fermi (1934), was formulated as a four-fermion contact interaction, where the coupling strength is dictated by the Fermi constant $G_F = 1.16638 \times 10^{-5}$ GeV^{-2}. A dimensional coupling constant leads to divergences in the cross sections calculations, therefore this type of interaction, that was originally successful in explaining the electroweak interactions short-range interaction

approximation, was later on interpreted as the low-energy approximation of a massive bosons-mediated interaction.

1.4.1 GSW model

The model developed by Glashow and then extended by Salam and Weinberg is an $SU(2)_L$ quantum field theory. In the $SU(2)_L$ group of symmetry L stands for the left-handed chiral components of the fields, since in this theory it is the only one involved in the weak interaction. Since the generators of $SU(2)_L$ are the Pauli matrices, it is useful to adopt the formalism of the angular momentum, therefore the particles eiegenstates of the weak interaction are arranged in six doublets of weak isospin. By naming t the weak isospin and t_3 its projection along one axis, the six doublets for leptons are:

$$t = 1/2 \qquad \begin{matrix} t_3 = +1/2 \\ t_3 = -1/2 \end{matrix} \qquad \begin{pmatrix} \nu_e \\ e \end{pmatrix}_L \begin{pmatrix} \nu_\mu \\ \mu \end{pmatrix}_L \begin{pmatrix} \nu_\tau \\ \tau \end{pmatrix}_L ,$$

and for quarks are:

$$t = 1/2 \qquad \begin{matrix} t_3 = +1/2 \\ t_3 = -1/2 \end{matrix} \qquad \begin{pmatrix} \mathrm{u} \\ \mathrm{d}' \end{pmatrix}_L \begin{pmatrix} \mathrm{c} \\ \mathrm{s}' \end{pmatrix}_L \begin{pmatrix} \mathrm{t} \\ \mathrm{b}' \end{pmatrix}_L .$$

Note that d', s' and b' are the weak interaction eigenstates that are obtained as linear combination the strong interaction eigenstates (or mass eigenstates) and the mixing of different flavours is given by:

$$\begin{pmatrix} \mathrm{d}' \\ \mathrm{s}' \\ \mathrm{b}' \end{pmatrix} = V \begin{pmatrix} \mathrm{d} \\ \mathrm{s} \\ \mathrm{b} \end{pmatrix},$$

where V is the complex unitary matrix named Cabibbo-Kobayashi-Maskawa, (CKM), matrix:

$$V = \begin{pmatrix} \mathrm{V_{ud}} & \mathrm{V_{us}} & \mathrm{V_{ub}} \\ \mathrm{V_{cd}} & \mathrm{V_{cs}} & \mathrm{V_{cb}} \\ \mathrm{V_{td}} & \mathrm{V_{ts}} & \mathrm{V_{tb}} \end{pmatrix}.$$

Sec. 1.4.4 reports a detailed derivation of the CKM matrix, its parametrization, and its most significant properties. The GSW model is developed in a similar way with respect to the QED theory. A local $SU(2)_L$ gauge transformation acting on the weak isospin

doublets is imposed:

$$\begin{pmatrix} \nu_\ell \\ \ell^- \end{pmatrix}_L' = e^{-\frac{i}{2}\vec{\alpha}(x)\cdot\vec{\tau}} \begin{pmatrix} \nu_\ell \\ \ell^- \end{pmatrix}_L , \tag{1.11}$$

where $\vec{\tau}$ are the Pauli matrices and $\vec{\alpha}(x)$ is the vector of real parameters of the transformation. Three gauge fields, named W^1, W^2 and W^3, transforming as a $t = 1$ multiplet (a triplet) under the group, are introduced. Two of these can be combined together in order to give two vector bosons $W^\pm$, that are electrically charged and can induce transitions between the members of the weak isospin doublets. The third gauge boson of the triplet should be electrically neutral. This feature can be exploited to provide an unified description of electromagnetic and weak forces by introducing a new $SU(2)_{is} \otimes U(1)_y$ symmetry group. The new Abelian $U(1)_y$ group is associated with weak hypercharge just as $SU(2)_{is}$ was associated with weak isospin. Indeed, Glashow proposed that the Gell–Mann-Nishijima relation for charges should also hold for these weak analogues, giving:

$$eQ = e\left(t_3 + \frac{y}{2}\right) \tag{1.12}$$

which represent the electric charge Q (in units of e) of the t_3 member of a weak isomultiplet, assigned a weak hypercharge y. Clearly, therefore, the lepton doublets, (ν_e, e^-) etc. have $y = -1$, while the quark doublets (u, d') etc. have $y = +1/3$. When this group is gauged the charged vector bosons appear as before but there are now two neutral vector bosons, whose combination will be responsible for the weak neutral current processes and for electromagnetism. The covariant derivative, that is needed to be introduced to make the free electroweak Lagrangian density invariant under the $SU(2)_{is} \otimes U(1)_y$ group, is:

$$D_\mu = \partial_\mu + ig\frac{\vec{\tau}}{2}W_\mu + ig'yB_\mu, \tag{1.13}$$

where g and g' are the two coupling constants for the two interactions. Neglecting the mass term for now, the electroweak Lagrangian density musts include a Dirac term for fermions:

$$\mathcal{L}_{fermions} = \sum_f \bar{\psi}\gamma^\mu D_\mu \psi \tag{1.14}$$

and a term for the dynamics of the gauge boson fields

$$\mathcal{L}_{gauge} = -\frac{1}{4}W_i^{\mu\nu}W^i_{\mu\nu} - \frac{1}{4}B^{\mu\nu}B_{\mu\nu} \tag{1.15}$$

where $W_i^{\mu\nu}$ and $B^{\mu\nu}$ are the tensor fields:

$$W_i^{\mu\nu} = \partial^\mu W_i^\nu - \partial^\nu W_i^\mu \tag{1.16}$$

$$B_i^{\mu\nu} = \partial^\mu B^\nu - \partial^\nu B^\mu \tag{1.17}$$

and W^μ is a three component vector field.
The complete Lagrangian density for the electroweak processes therefore is:

$$\begin{aligned}\mathcal{L}_{EW} = &- i\psi_L\gamma^\mu\left(\partial_\mu + ig\frac{\vec{\tau}}{2}\cdot W_\mu + ig'yB_\mu\right)\psi_L + \\ &- i\psi_R\gamma^\mu\left(\partial_\mu + ig'yB_\mu\right)\psi_R + \\ &- \frac{1}{4}W_i^{\mu\nu}W^i_{\mu\nu} - \frac{1}{4}B^{\mu\nu}B_{\mu\nu} + \\ &+ \frac{1}{2}g\,\epsilon_{ijk}W_i^{\mu\nu}W_{j\mu}W_{k\nu} + \frac{1}{4}g^2\,\epsilon_{ijk}\epsilon_{imn}W_{j\mu}W_{k\nu}W_m^\mu W_n^\nu,\end{aligned} \tag{1.18}$$

where ψ_L and ψ_R are the left and right-handed chiral components of the particles, and the term in the last line terms describe the three and four-point self interactions of the vector bosons that arise because of the non-Abelian nature of the $SU(2)_{is}$ group. The four gauge fields can be combined to produce the physical vector fields for the $W^\pm, Z$ bosons and the photon:

$$W_\mu^\pm = \sqrt{\tfrac{1}{2}}\left(W_\mu^1 \mp W_\mu^2\right) \tag{1.19}$$

$$A_\mu = B_\mu\cos\theta_W + W_\mu^3\sin\theta_W \tag{1.20}$$

$$Z_\mu = -B_\mu\sin\theta_W + W_\mu^3\cos\theta_W \tag{1.21}$$

where θ_W is the Weinberg angle, or weak mixing angle, defined as:

$$\cos\theta_W = \frac{g}{\sqrt{g^2+g'^2}}, \quad \text{and} \quad \sin\theta_W = \frac{g'}{\sqrt{g^2+g'^2}} \tag{1.22}$$

The electromagnetic charge therefore is:

$$q = g'\cos\theta_W = g\sin\theta_W \tag{1.23}$$

1.4.2 Spontaneous symmetry breaking and Higgs mechanism

The electroweak theory up to now does not foresee a mass term for $W^\pm$ and Z bosons. In order for they to acquire mass, the simplest and most elegant way is the

spontaneous symmetry breaking (SSB). The SSB succeed in giving mass to particles by the introduction of another particle: the Higgs boson. The Higgs boson field is a doublet of complex scalar fields that can be written as:

$$\begin{pmatrix} \phi^+ \\ \phi^0 \end{pmatrix} = \begin{pmatrix} \phi_1 + i\phi_2 \\ \phi_3 + i\phi_4 \end{pmatrix} \tag{1.24}$$

and to this field is associate the Lagrangian density:

$$\begin{aligned} \mathcal{L}_H &= (D^\mu \phi)^\dagger D_\mu \phi - V(\phi) = \\ &= (D^\mu \phi)^\dagger D_\mu \phi - \frac{1}{2}\mu^2 \phi^\dagger \phi - \frac{1}{4}\lambda(\phi^\dagger \phi)^2, \end{aligned} \tag{1.25}$$

where $V(\phi)$ is the potential responsible of the symmetry breaking. When the covariant derivative 1.13 acts on the Higgs field produces the following Lagrangian density:

$$\mathcal{L}_H = (D^\mu \phi)^\dagger D_\mu \phi - \frac{1}{2}\mu^2 \phi^\dagger \phi - \frac{\lambda}{4}(\phi^\dagger \phi)^2 - \frac{1}{4}F^{\mu\nu}F_{\mu\nu} - \frac{1}{4}G^{\mu\nu}G_{\mu\nu}, \tag{1.26}$$

where:

$$D^\mu \phi = \left(\partial^\mu + ig\frac{\vec{\tau}}{2}W^\mu + ig' y B^\mu\right)\phi \tag{1.27}$$

$$F^{\mu\nu} = \partial^\mu W^\nu - \partial^\nu W^\mu - gW^\mu \times W^\nu \tag{1.28}$$

$$G^{\mu\nu} = \partial^\mu B^\nu - \partial^\nu B^\mu. \tag{1.29}$$

By requiring that $\mu^2 < 0$ and $\lambda > 0$ the minimum of the potential is not unique, as shown in the Figure 1.1, and the Higgs field assumes the value:

$$\phi = \begin{pmatrix} 0 \\ \frac{1}{\sqrt{2}}(v + H(x)), \end{pmatrix} \tag{1.30}$$

where:

$$v = -\sqrt{-\frac{\mu^2}{\lambda}}. \tag{1.31}$$

By substituting 1.30 in 1.26, one finds that:

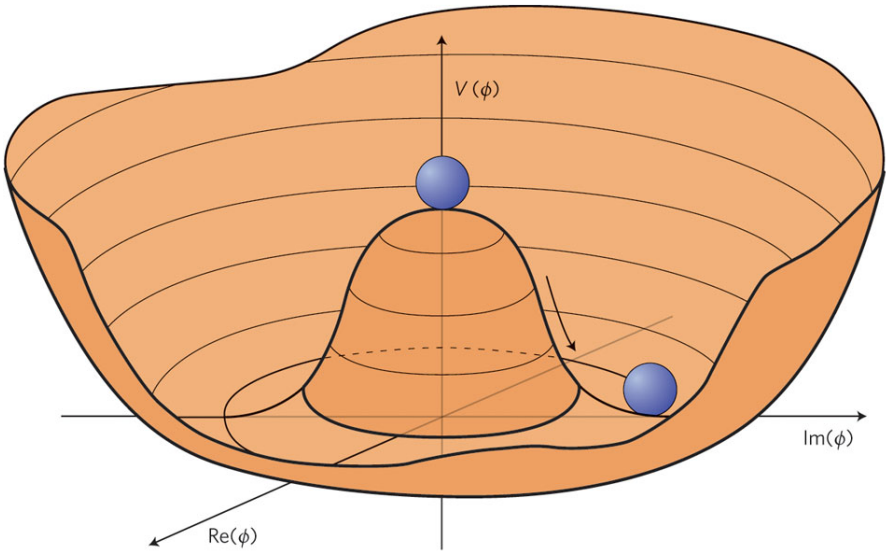

Figure 1.1: Shape of the Higgs potential for $\mu^2 < 0$.

$$\begin{aligned}\mathcal{L}_{G\Phi} = &\frac{1}{2}\partial_\mu H \partial^\mu H - \mu^2 H^2 + \\ &- \frac{1}{4}(\partial_\mu W^1_\nu - \partial_\nu W^1_\mu)(\partial^\mu W^{1\nu} - \partial^\nu W^{1\mu}) + \frac{1}{8}g^2 v^2 W^1_\nu W^{1\nu} \\ &- \frac{1}{4}(\partial_\mu W^2_\nu - \partial_\nu W^2_\mu)(\partial^\mu W^{2\nu} - \partial^\nu W^{2\mu}) + \frac{1}{8}g^2 v^2 W^2_\nu W^{2\nu} \\ &- \frac{1}{4}(\partial_\mu Z_\nu - \partial_\nu Z_\mu)(\partial^\mu Z^\nu - \partial^\nu Z^\mu) + \frac{1}{8}(g^2 + g'^2)v^2 Z_\nu Z^\nu \\ &- \frac{1}{4}F^{\mu\nu}F_{\mu\nu}.\end{aligned} \tag{1.32}$$

The first line of 1.32 shows that we have a scalar field of mass $\sqrt{2}\mu$ (the Higgs boson, again). The next two lines show that the components W^1 and W^2 of the triplet (W^1, W^2, W^3) acquire a mass:

$$M_1 = M_2 = \frac{1}{2}gv \equiv M_W. \tag{1.33}$$

The third line shows that the field Z^μ acquires a mass:

$$M_Z \equiv \frac{1}{2}v\sqrt{g^2 + g'^2} = \frac{M_W}{\cos\theta_W} \tag{1.34}$$

and, finally, the last line shows that the field A^μ has a mass:

$$M_A = 0. \tag{1.35}$$

1.4.3 Masses of leptons

The fermion mass term $-m\bar{\psi}\psi$ is not invariant under the $SU(2)_{is} \otimes U(1)_y$ group because of the different transformation of the right and left-handed chiral components of the fields. It is possible to introduce a gauge invariant mass term with a Yukawa coupling between the fermion field and the Higgs field written as:

$$\mathcal{L}_Y = g_f(\bar{\psi}_L \phi \psi_R - \bar{\psi}_R \phi^\dagger \psi_L), \tag{1.36}$$

where g_f is the Yukawa coupling constant. By substituting 1.30 in 1.36 one obtains:

$$\begin{aligned} \mathcal{L}_Y =& \frac{g_f}{\sqrt{2}}\left[(\nu_\ell,\ \ell)\begin{pmatrix}0\\ v+H\end{pmatrix}\ell_R + \ell_R(0,\ v+H)\begin{pmatrix}\nu_\ell\\ \ell\end{pmatrix}\right] = \\ =& \frac{g_f}{\sqrt{2}}(v+H)(\ell_L\ell_R + \ell_R\ell_L) \end{aligned} \tag{1.37}$$

so that the constant coefficient of $(\ell_L\ell_R + \ell_R\ell_L)$ is the mass term for leptons:

$$m_f = \frac{v}{\sqrt{2}} g_f. \tag{1.38}$$

Even if this kind of Yukawa coupling solves the problem of leptons' masses, it does not arise from a gauge principle and it is purely phenomenological.

1.4.4 Masses of quarks and CKM matrix

Analogously to the lepton case, one can write for quarks:

$$\begin{aligned} \mathcal{L}_Y =& \frac{1}{\sqrt{2}}\left[g^d_{i,j}(u_{i,L},\ d_{i,L})\begin{pmatrix}0\\ v+H\end{pmatrix} d_{j,R} + g^u_{i,j}(u_{i,L},\ d_{i,L})\begin{pmatrix}-(v+H)^*\\ 0\end{pmatrix} u_{j,R} + h.c.\right] = \\ =& \frac{1}{\sqrt{2}}(v+H)[g^u_{ij}(u_{i,L}u_{j,R} + u_{j,R}u_{i,L}) + g^d_{ij}(d_{i,L}d_{j,R} + d_{j,R}d_{i,L}) + h.c.] \end{aligned} \tag{1.39}$$

where u_i = (u, c, t) and d_i = (d, s, b), and the mass term are:

$$m^u_{ij} = -\frac{v}{\sqrt{2}} g^u_{ij} \quad m^d_{ij} = -\frac{v}{\sqrt{2}} g^d_{ij}. \tag{1.40}$$

The mass term m^u and m^d are not diagonal in this basis but they can be made diagonal with four different transformations on the triplets $u_{i,L}$, $u_{i,R}$, $d_{i,L}$, and $d_{i,R}$ written as:

$$u_{\alpha,L} = (\mathcal{U}^u_L)_{\alpha i} u_{i,L} \quad u_{\alpha,R} = (\mathcal{U}^u_R)_{\alpha i} u_{i,R} d_{\alpha,L} = (\mathcal{U}^d_L)_{\alpha i} d_{i,L} \quad d_{\alpha,R} = (\mathcal{U}^d_R)_{\alpha i} d_{i,R} \tag{1.41}$$

where α is the index in the mass diagonal basis and i is the index in the non-diagonal weak interaction basis.

$$\mathcal{L}_Y = \frac{1}{\sqrt{2}}(v+H)\left[m^u \mathrm{u}\bar{\mathrm{u}} + m^d \mathrm{d}\bar{\mathrm{d}} + m^s \mathrm{s}\bar{\mathrm{s}} + m^c \mathrm{c}\bar{\mathrm{c}} + m^t \mathrm{t}\bar{\mathrm{t}} + m^b \mathrm{b}\bar{\mathrm{b}}\right] \tag{1.42}$$

The same transformations must to be applied to the interacting term invariant under the $SU(2)_{is} \otimes U(1)_y$ symmetry that still contains the eigenkets of the weak interaction. When this operation is worked out the term of the coupling with the Z boson, i.e. neutral current coupling term, is diagonal also in the mass basis if the transformations of Eq. 1.41 are unitary, instead the term of the coupling with the W boson, i.e. charged current coupling term, is:

$$\begin{aligned}
\mathcal{L}_{CC} =& -\frac{g}{\sqrt{2}}(\bar{u}_{i,L},\ \bar{d}_{i,L})\gamma^\mu \tau_+ W^+_\mu \begin{pmatrix} u_{Li} \\ d_{Li} \end{pmatrix} + h.c. \\
=& -\frac{g}{\sqrt{2}}\bar{u}_{iL}\gamma^\mu d_{Li} W^+_\mu + h.c. \\
=& -\frac{g}{\sqrt{2}}\bar{u}_{\alpha_L}\left[(\mathcal{U}^u_L)_{\alpha i}(\mathcal{U}^d_L)^\dagger_{\beta i}\right]\gamma^\mu d_{L\beta} W^+_\mu + h.c.,
\end{aligned} \tag{1.43}$$

where the matrix:

$$V_{\alpha\beta} = \left[\mathcal{U}^u_L \mathcal{U}^{d\dagger}_L\right]_{\alpha\beta} \tag{1.44}$$

is unitary but not diagonal. V is the CKM matrix and it is a 3×3 unitary matrix. It can be parametrised by three mixing angles and the CP-violating KM phase as follow:

$$V_{\mathrm{CKM}} = \begin{pmatrix} 1 & 0 & 0 \\ 0 & c_{23} & s_{23} \\ 0 & -s_{23} & c_{23} \end{pmatrix} \begin{pmatrix} c_{13} & 0 & s_{13}e^{-i\delta} \\ 0 & 1 & 0 \\ -s_{13}e^{i\delta} & 0 & c_{13} \end{pmatrix} \begin{pmatrix} c_{12} & s_{12} & 0 \\ -s_{12} & c_{12} & 0 \\ 0 & 0 & 1 \end{pmatrix}, \tag{1.45}$$

where $s_{ij} = \sin\theta_{ij}$, $c_{ij} = \cos\theta_{ij}$ and δ is the phase responsible for all CP-violating phenomena in flavour-changing processes in the SM. The angles θ_{ij} can be chosen to lie in the first quadrant, so $s_{ij}, c_{ij} \geq 0$.

It is known experimentally that $s_{13} \ll s_{23} \ll s_{12} \ll 1$, and it is convenient to exhibit this hierarchy using the Wolfenstein parametrization. By defining:

$$\begin{aligned}
s_{12} = \lambda = \frac{\mathrm{V_{us}}}{\sqrt{|\mathrm{V_{us}}|^2 + |\mathrm{V_{us}}|^2}}, \qquad & s_{12} = A\lambda^2 = \lambda\left|\frac{\mathrm{V_{cb}}}{\mathrm{V_{us}}}\right|, \\
s_{13}e^{i\delta} = \mathrm{V^*_{us}} = A\lambda^3(\rho + i\eta) = & \frac{A\lambda^3(\bar{\rho}+i\bar{\eta})\sqrt{1-A^2\lambda^4}}{\sqrt{1-\lambda^2}[1-A^2\lambda^4(\bar{\rho}+i\bar{\eta})]}
\end{aligned} \tag{1.46}$$

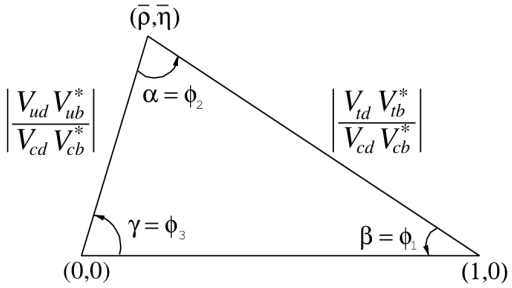

Figure 1.2: Sketch of the unitarity triangle.

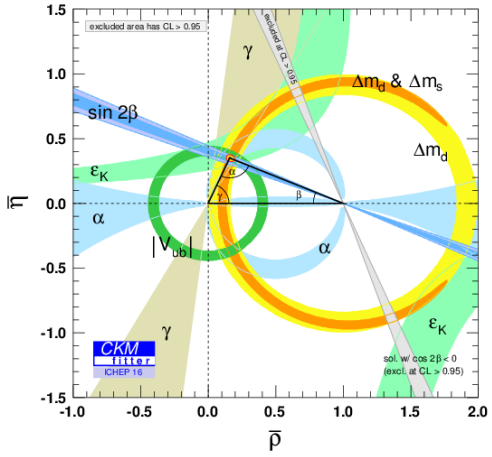

Figure 1.3: Global fit of the SM parameters.

These relations ensure that $\bar{\rho}+i\bar{\eta} = -\mathrm{V_{ud}V_{ub}^*}/\mathrm{V_{cd}V_{cb}^*}$ is phase convention independent, and the CKM matrix written in terms of λ, A, $\bar{\rho}$, and $\bar{\eta}$ is unitary to all orders in λ.

$$V_{\mathrm{CKM}} = \begin{pmatrix} 1-\lambda^2/2 & \lambda & A\lambda^3(\rho+i\eta) \\ -\lambda & 1-\lambda^2/2 & A\lambda^2 \\ A\lambda^3(1-\rho-i\eta) & -A\lambda^2 & 1 \end{pmatrix} + \mathcal{O}(\lambda^4). \tag{1.47}$$

The CKM matrix elements are fundamental parameters of the SM, so their precise determination is important. The unitarity of the CKM matrix imposes $\sum_i = V_{ij}V_{ik}^* = \delta_{jk}$ and $\sum_j = V_{ij}V_{kj}^* = \delta_{ik}$. The six vanishing combinations can be represented as triangles in a complex plane, of which those obtained by taking scalar products of neighbouring rows or columns are nearly degenerate. The areas of all triangles are the same, half of the Jarlskog invariant, J [19], which is a phase-convention-independent measure of CP violation, defined by $\mathrm{Im}[V_{ij}V_{kl}V_{il}^*V_{kj}^*] = J\sum_{mn}\epsilon_{ikm}\epsilon_{jln}$.

The most commonly used unitarity triangle, reported in Figure 1.2 arises from:

$$\mathrm{V_{ud}V_{ub}^* + V_{cd}V_{cb}^* + V_{td}V_{tb}^* = 0}, \tag{1.48}$$

by dividing each side by the best-known one, $\mathrm{V_{cd}V_{cb}^*}$.

Its vertices are exactly (0,0), (1,0), and $(\bar{\rho},\bar{\eta})$. An important goal of flavour physics is to overconstrain the CKM elements, and many measurements can be conveniently displayed and compared in the $\bar{\rho},\bar{\eta}$ plane. A global fit on the SM parameters is then

performed in order to extract, amongst the others, the elements of the CKM matrix. The most recent [20] fit, reported in Figure 1.3 gives the following values:

$$V_{\mathrm{CKM}} = \begin{pmatrix} 0.974334^{+0.000064}_{-0.000068} & 0.22508^{+0.00030}_{-0.00028} & 0.003715^{+0.000060}_{-0.000060} \\ 0.22494^{+0.00029}_{-0.00028} & 0.973471^{+0.000067}_{-0.000067} & 0.04181^{+0.00028}_{-0.00060} \\ 0.008575^{+0.000076}_{-0.000098} & 0.04108^{+0.00030}_{-0.00057} & 0.999119^{+0.000024}_{-0.000012} \end{pmatrix}. \tag{1.49}$$

The CKM matrix has a well known scale dependence above the weak scale [21, 22], below $\mu = m_{\mathrm{W}}$ the CKM elements can be treated as constants, with all μ-dependence contained in the running of quark masses and higher-dimension operators.

1.5 Quantum chromodynamics

The quantum chromodynamics, or QCD for short, is the non-Abelian quantum gauge field theory which describes the strong interaction between quarks. The symmetry group for this theory is $SU(3)_{col}$, where the subscript *col* stands for the charge associated with this symmetry, named colour. This theory is invariant under the $SU(3)_{col}$ transformation:

$$\psi \to \psi' = e^{ig_s \vec{\alpha}(x)\cdot\vec{T}}\psi, \tag{1.50}$$

where $\vec{T} = T^{\alpha}$ are the eight generators of the symmetry group, which are related to the Gell-Mann matrices:

$$T^a = \frac{1}{2}\lambda^a \tag{1.51}$$

and $\vec{\alpha}(x)$ are eight functions of the space-time coordinate x. The commutation rules of λ_a are:

$$\left[\frac{\lambda_a}{2}, \frac{\lambda_b}{2}\right] = i f_{abc}\frac{\lambda_c}{2}, \tag{1.52}$$

where f_{abc} are the structure constants of the groups and the indices run from 1 to 8. Because the generators of $SU(3)_{col}$ are represented by 3×3 matrices, the field ψ includes three additional degrees of freedom. This new degree of freedom, colour, has three possible states labelled as red, green and blue. The $SU(3)_{col}$ local phase transformation corresponds to rotating states in this colour space about an axis whose direction is different at every point in space-time. The imposition of local invariance under the $SU(3)_{col}$ group leads to the introduction of the covariant derivative:

$$D_\mu = \partial_\mu + i g_s \frac{\lambda_a}{2} G^a_\mu. \tag{1.53}$$

where G_μ^a are the 8 gluon fields that transform as:

$$G_\mu^a \to G_\mu'^a = G_\mu^a + ig_s f^{abc}\theta_b(x)G_{c,\mu} \tag{1.54}$$

When this is applied to the Dirac equation for quarks, by adding the contributions of the gluons one obtains the complete Lagrangian density for the QCD:

$$\mathcal{L}_{QCD} = \bar{\psi}\gamma^\mu\partial_\mu\psi - m\bar{\psi}\psi - igs\bar{\psi}\gamma^\mu\lambda_a\psi G_\mu^a - \frac{1}{4}G_a^{\mu\nu}G_{\mu\nu}^a \tag{1.55}$$

with $G_a^{\mu\nu}$ the tensor field defined as

$$G_a^{\mu\nu} = \partial^\mu G_a^\nu - \partial^\nu G_a^\mu - g_s f_{abc}G^{b,\mu}G^{c,\nu} \tag{1.56}$$

Also in this case, like in the Electroweak theory, some self-interaction terms arise due to the non-Abelian nature of the symmetry group.

The QCD theory exhibits two relevant properties, that significantly differentiate it from the electroweak theory: colour confinement and asymptotic freedom. Both these two properties stem from experimental evidence and are successfully described in the context of the SM explanation of the strong interactions.

The latter property has been formulated to cope with the experimental fact that no coloured hadron is observed in nature. Hadrons are interpreted as bound states of quarks in the QCD parton model and so they must be colour singlets. This imposes restrictions on the types of the bound quark state configurations can exist. All this can be summarized by saying that the quark colour degree of freedom must be confined.

The former property can be explained by looking at the running coupling constant form of strong force:

$$\alpha_s\left(|q^2|\right) = \frac{\alpha_s(\mu^2)}{\left[1 + \alpha_s(\mu^2)\frac{33-2N_f}{12\pi}\ln\frac{|q^2|}{\mu^2}\right]}, \tag{1.57}$$

where q^2 is the transferred 4-momentum, μ is a scale parameter for the strength of the coupling, N_f is the number of fermions capable of strong interactions at the scale considered. It can be seen that $\alpha_s(|q^2|)$ decreases as $|q^2|$ increases. For $|q| \sim 200$ MeV the value of α_s is large enough that any perturbative approach cannot be applied. In this region the calculations are carried on with the QCD-lattice approach.

For increasing values of $|q^2|$, $\alpha_s(|q^2|)$ decreases and one moves towards a regime in which perturbative approach is a good approximation.

1.6 Unsolved issues in the Standard Model

The SM succeeds in giving an exhaustive explanation of the three fundamental interactions: electromagnetic, weak and strong. The electroweak theory successfully predicts the existence and the features of the weak neutral current, the existence and masses of the W and Z bosons, the charm quark as required by the GIM mechanism, the existence of the top quark and its measurable contributions to radiative corrections, driven by its large mass, which are a further validation of the mathematically-consistence of renormalizable field theory. Although the original formulation didn't provide for massive neutrinos, they can be included by the addition of right-handed states ν_R (Dirac) or by introduction of Majorana neutrinos and the see-saw mechanism. Another great success is the prediction of the existence of the Higgs boson, which is the last experimental validation of the electroweak theory. Despite this the SM model fails in giving explanation of many other phenomena. Some notable problems still unsolved are:

- Gravity: the SM does not include in any way General Relativity.
- Matter-antimatter asymmetry: the sole SM CP-violation in the quark sector is not sufficient to justify the actual matter-antimatter asymmetry measured in the universe.
- Hierarchy in fermion masses: there is no explanation or prediction of fermion masses that occur in a hierarchical pattern which varies over 5 order of magnitudes between the top quark and the electron and even more mysterious are the neutrinos, which are many orders of magnitude lighter still.
- Higgs mass fine tuning: the tree-level (bare) Higgs mass receives corrections from fermion loop diagrams which are quadratically-divergent and that are not cancelled by the boson loop diagrams. With the present framework the Higgs mass should be of several orders of magnitude greater than the observed one if no new physics exists until the Plank scale $M_P = G_N^{-1/2} \sim 10^{19}$ GeV.
- Dark matter: from astrophysical observations it is found that the orbits followed by galaxies are different from which expected considering the gravitational effects of the usual matter; it could be explained with the existence of an amount of extra matter not composed of known SM particles: it is referred to that matter as dark matter.
- Dark energy: from cosmological observations, in particular from the red shift measurement, it is discovered that the Universe is accelerated. There is an unknown

form of energy, called dark energy, which is hypothesized to permeate all of space, tending to accelerate the expansion of the universe. This phenomenon has no explanation in the SM framework.

- Flavour changing neutral current: the SM doesn't predict the observed suppression of flavour changing due to neutral current.

Chapter 2

The CMS experiment at LHC

2.1 Physics motivation

The prime motivation of the Large Hadron Collider (LHC) [23] is to elucidate the nature of electroweak symmetry breaking for which the Higgs mechanism is responsible. The experimental study of the Higgs mechanism can also shed light on the mathematical consistency of the SM at energy scales above about 1 TeV. Various alternatives to the Standard Model invoke new symmetries, new forces or constituents. There are many compelling reasons to investigate the TeV energy scale: supersymmetry, dark matter or extra dimensions.

The LHC also provides high-energy heavy-ion beams at energies over 30 times higher than at the previous accelerators, allowing to further extend the study of QCD matter under extreme conditions of temperature, density, and parton momentum fraction (low-x). Hadron colliders are well suited to the task of exploring new energy domains, and the region of 1 TeV constituent centre-of-mass energy can be explored if the proton energy and the luminosity are high enough. The beam energy and the design luminosity of the LHC have been chosen in order to study physics at the TeV energy scale. A wide range of physics processes is potentially at the reach of LHC with the seven-fold increase in energy and a hundred-fold increase in integrated luminosity over the previous hadron collider experiments.

2.2 Large Hadron Collider

The LHC at CERN near Geneva is the largest circular accelerator and one of the most powerful tools for fundamental particle physics research. It is designed to collide

proton beams with a centre-of-mass energy of 14 TeV and an unprecedented luminosity of 10^{34} cm^{-2}s^{-1}. It can also collide heavy (Pb) ions with an energy of 2.8 TeV per nucleon and a peak luminosity of 10^{27} cm^{-2}s^{-1}. The aim of the LHC is to reveal the physics beyond the SM with centre of mass collision energies of up to 14 TeV.

The number of events per second generated in the LHC collisions is given by:

$$N_{event} = L\sigma_{event} \tag{2.1}$$

where σ_{event} is the cross section for the event under study and L is the machine luminosity. The machine luminosity depends only on the beam parameters and can be written, for circular proton-proton accelerators and assuming a Gaussian beam distribution, as:

$$L = \frac{N_b^2 \gamma_r f_{rev} n_b}{4\pi\epsilon_n \beta^*} F, \tag{2.2}$$

where N_b is the number of particles per bunch, n_b the number of bunches per beam, f_{rev} the revolution frequency, γ_r the relativistic gamma factor, ϵ_n the normalized transverse beam emittance, β^* the beta function at the collision point, and F the geometric luminosity reduction factor due to the crossing angle at the interaction point.

The LHC is located in an underground 26.7 km long tunnel which was originally built to host the CERN Large Electron Positron (LEP) accelerator. The tunnel is located between 45 and 170 meters below the surface, crossing the border between France and Switzerland, and it is connected to the CERN accelerating complex by two tunnels.

The CERN accelerating complex is shown in Figure 2.1 and produces proton beams of energy of 450 GeV: the first step of accelerating process is performed by LINAC 2 (LINear particle ACcelerator), which produces proton beams of energy of 50 MeV; the second step is performed by PSB (Proton Synchrotron Booster) which accelerates the beams up to 1.4 GeV; then the beams are injected in PS (Proton Synchrotron) which produces proton beams of energy of 26 GeV; finally, the last step is SPS (Super Proton Synchrotron) and the beams reach the energy of 450 GeV and can be injected in the LHC, where the beams reach their maximum energy of 7 TeV.

To accomplish to this performance the LHC is composed of 1232 dipole magnets, necessary to keep the beams in the circular ring, 392 quadrupole magnets, which focus the beams, a superconducting cavity system of radiofrequencies (RF) which accelerate the beams and some other spool piece correction magnets (sextupole and octupole/decapole). The LHC magnet system makes use of the well-proven technology based on NbTi Rutherford cables and cools the magnets to a temperature below 2 K,

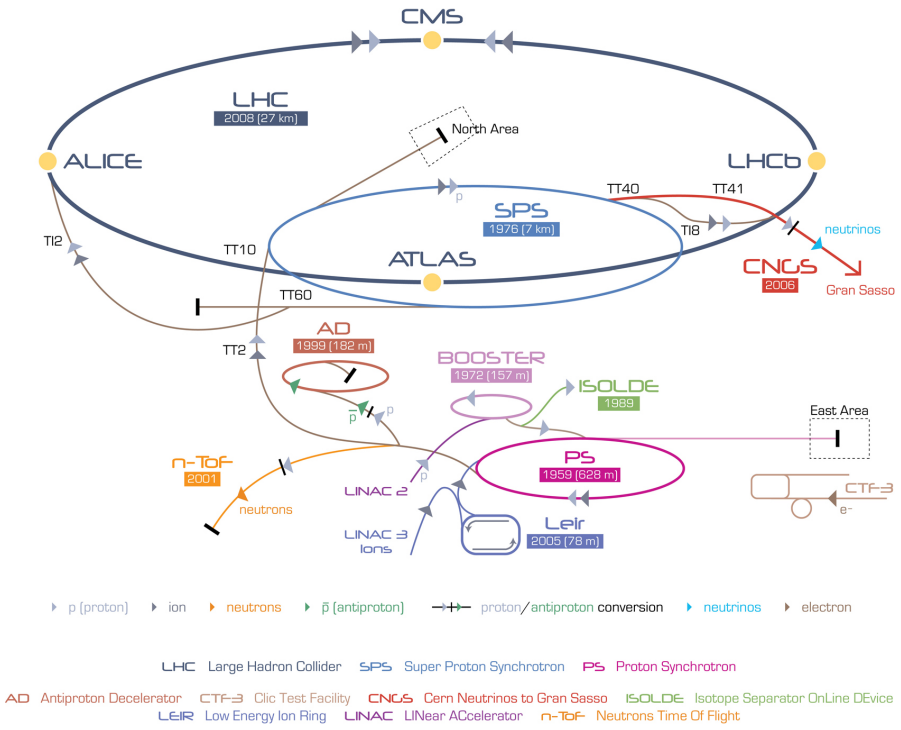

Figure 2.1: The CERN accelerating complex.

using superfluid helium, and operates at fields above 8.33 T.

Driven by the required beam lifetime and background at the experiments, the beam pipe of magnets require the vacuum. The LHC has three vacuum systems: the insulation vacuum for cryomagnets, the insulation vacuum for helium distribution (QRL), and the beam vacuum. The insulation vacua before cool-down do not have to be better than 10^{-1} mbar, but at cryogenic temperatures, in the absence of any significant leak, the pressure will stabilise around 10^{-6} mbar. In the interaction regions around the experiments, the requirements for the beam vacuum are much more stringent to minimise the background to the experiments. In the room temperature parts of the beam vacuum system, the pressure should be in the range 10^{-10} to 10^{-11} mbar.

The LHC has four main experiments:

- ALICE: *A Large Ion Collider Experiment* is a dedicated ion experiment; it works with $\sqrt{s} = 2.67$ TeV lead-lead ion collisions aiming at a peak luminosity of $L = 10^{27}$ cm^{-2}s^{-1}.

- ATLAS: *A Toroidal LHC ApparatuS* is a general-purpose detector whose targets are precision measurements of SM, the search and the study of Higgs boson, and

Period	$\sqrt{s}$ [TeV]	LHC delivered [fb^{-1}]	CMS Recorded [fb^{-1}]	CMS Validated [fb^{-1}]
Run 1 (2010)	7	40.22×10^{-2}	40.76×10^{-2}	34.68×10^{-2}
Run 1 (2011)	7	6.13	5.55	5.09
Run 1 (2012)	8	23.30	21.79	19.79
Run 2 (2015)	13	4.22	3.81	2.39
Run 2 (2016)	13	40.82	37.76	35.92

Table 2.1: The cumulative luminosity delivered by LHC, recorded by CMS and certified as Good for physics analysis, during each period of activity.

mechanisms due to new physics. It is 46 m long and has a 25 m diameter and it is the biggest experiment at LHC.

- CMS: *Compact Muon Solenoid* is described in section 2.3.
- LHCb: *LHC-beaty* is an experiment designed and optimized for the study of the b quark properties and its production mechanism. It is the only one experiment that works with asymmetric beams: one is at the LHC full energy (up to 7 TeV) and the other is at the injection energy (450 GeV).

The LHC activity started in 2010 with $\sqrt{s} = 7$ TeV pp collisions until 2011; in 2012/2013 the pp collisions was at $\sqrt{s} = 8$ TeV. The 2010-2013 activity is called LHC Run 1. In 2013 LHC stopped for the upgrade of the detectors in view of the $\sqrt{s} = 14$ TeV pp collisions. In 2015 the LHC activity started again with $\sqrt{s} = 13$ TeV pp collisions until nowadays. This last period is called LHC Run 2 and will include the $\sqrt{s} = 14$ TeV pp collisions too. The data collected during the years are reported in Table 2.1 and the CMS data collected and validated are reported too.

2.3 CMS experiment

The Compact Muon Solenoid, CMS for short, experiment is one of the four great experiments at the LHC. It is a general-purpose-detector, meaning its research program includes most of the physics at the LHC, from the SM measurements to the Higgs and new physics searches.

CMS is equipped with a huge superconducting magnet, as shown in Figure 2.2 which produces a solenoidal magnetic field of 3.8 T and from which the experiment takes its name.

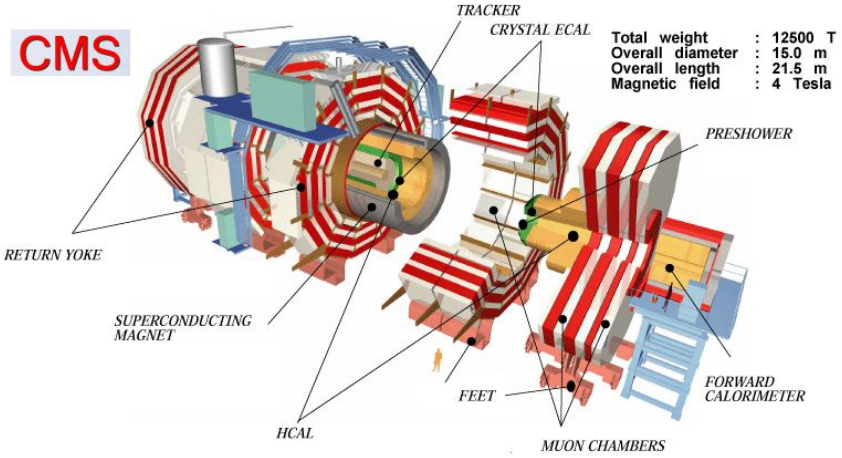

Figure 2.2: The CMS experiment.

It has a complex system of sub-detectors shown in Figure 2.3 that allows to identify different particles with an high momentum resolution on a wide energy and angular coverage. CMS has a component coaxial to the beam, named Barrel, and two components that close the barrel, named Endcaps. CMS has a cylindrical symmetry and it is 21.6 m long with a diameter of 14.6 m and a total weight of about 14500 tons.

The CMS coordinate system used to describe the detector is a right-handed Cartesian frame, centred in the interaction point and with the z axis along the beam line (this direction is referred to as longitudinal). The x axis is chosen to be horizontal and pointing towards the centre of the LHC ring, and the y axis is vertical and pointing upwards. The $x-y$ plane is called transverse plane. Given the cylindrical symmetry of the CMS design, usually a (ϕ, θ) cylindrical coordinate system is used in the reconstruction of the tracks of particles. ϕ is the polar angle, laying in the $x-y$ plane, measured from the x axis in mathematical positive direction (i.e. the y axis is at $\phi = 90°$) and the radial coordinate in this plane is referred to as r. The azimuthal angle θ is measured from the z axis towards the $x-y$ plane. The angle θ can be translated into the pseudorapidity η by:

$$\eta = -\ln\left(\tan\frac{\theta}{2}\right) \tag{2.3}$$

A longitudinal view of the CMS detector displaying the segmentation in η of the sub-detectors is shown in Figure 2.4. Using these parameters, a distance between two particle directions can be defined as:

$$\Delta R = \sqrt{(\Delta\phi)^2 + (\Delta\eta)^2} \tag{2.4}$$

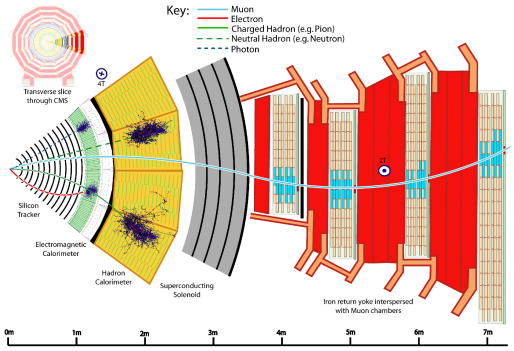

Figure 2.3: The CMS subdetectors system.

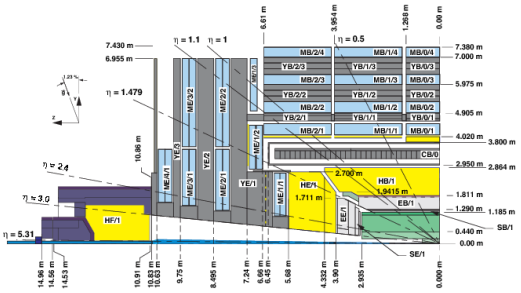

Figure 2.4: Longitudinal view of the CMS detectors.

Referring to the Cartesian system, the momentum of a particle can be divided in two components: the longitudinal momentum p_z and the transverse momentum p_{T}, defined as:

$$\vec{p_T} = \sqrt{\vec{p_x}^2 + \vec{p_y}^2} \tag{2.5}$$

The magnet bends charged tracks on the ϕ plane, so that the curvature of the tracks allows for measurements of the particles p_{T}.

For a particle of energy E, the variable rapidity (y) is also introduced, defined as:

$$y = \frac{1}{2} \ln \left(\frac{E + p_z c}{E - p_z c} \right) \tag{2.6}$$

For ultra relativistic particles rapidity can be approximated by pseudorapidity. Both rapidity and p_{T} are used because the centre-of-mass of parton-parton collisions can be boosted along the z direction; both these quantities have invariance properties under this kind of boost. The CMS sub-detector system, starting from the interaction point and going outwards, consists of: the inner tracking system, the electromagnetic calorimeter, the hadron calorimeter, the magnet, and, finally, the iron return yoke interspersed with muon chambers.

2.3.1 The tracking system

The inner tracking system of CMS is designed to provide a precise and efficient measurement of the trajectories of charged particles emerging from the LHC collisions, as well as a precise reconstruction of secondary vertices. It surrounds the interaction point and has a length of 5.8 m and a diameter of 2.5 m. The CMS solenoid provides

a homogeneous magnetic field of 3.8 T over the full volume of the tracker. The CMS tracker is composed of a pixel detector with three barrel layers at radii between 4.4 cm and 10.2 cm and a silicon strip tracker with 10 barrel detection layers extending outwards to a radius of 1.1 m. Each system is completed by endcaps which consist of 2 disks in the pixel detector and 3 plus 9 disks in the strip tracker on each side of the barrel, extending the acceptance of the tracker up to a pseudorapidity of $|\eta| < 2.5$. With about 200 m^2 of active silicon area the CMS tracker is the largest silicon tracker ever built [24, 25].

2.3.2 The electromagnetic calorimeter

The electromagnetic calorimeter of CMS (ECAL) is a hermetic homogeneous calorimeter made of 61 200 lead tungstate ($PbWO_4$) crystals mounted in the central barrel part, closed by 7324 crystals in each of the two endcaps. The characteristics of the $PbWO_4$ crystals [26] make them an appropriate choice for operation at LHC. The high density (8.28 g/cm^3), short radiation length (0.89 cm) and small Molière radius (2.2 cm) result in a fine granularity and a compact calorimeter. The scintillation decay time of these production crystals is of the same order of magnitude as the LHC bunch crossing time: about 80% of the light is emitted in 25 ns. The barrel part of the ECAL (EB) covers the pseudorapidity range $|\eta| < 1.479$, occupies a volume of 8.14 m^3 and its weight is 67.4 tons. The endcaps (EE) cover the rapidity range $1.479 < |\eta| < 3.0$, occupy a volume of 2.90 m^3 and the weight is 24.0 tons. The energy resolution of the ECAL of CMS is:

$$\left(\frac{\sigma}{E}\right)^2 = \left(\frac{2.8\%}{\sqrt{E}}\right)^2 + \left(\frac{0.12}{E}\right)^2 + (0.30\%)^2\,, \tag{2.7}$$

where E is in GeV.

2.3.3 The hadron calorimeter

The CMS detector is designed to study a wide range of high-energy processes involving diverse signatures of final states. The hadron calorimeters are particularly important for the measurement of hadron jets momenta and neutrinos or exotic particles resulting in apparent missing transverse energy. The hadron calorimeter barrel and endcaps sit behind the tracker and the electromagnetic calorimeter as seen from the interaction point. The hadron calorimeter barrel is radially restricted between the outer extent of the electromagnetic calorimeter ($r = 1.77$ m) and the inner extent of the magnet coil ($r = 2.95$ m). This constrains the total amount of material which can be put in to absorb the hadronic shower. Therefore, an outer hadron calorimeter or tail catcher

Properties of C26000	
Chemical composition	70% Cu, 30% Zn
density	8.53 g/cm^3
radiation length	1.49 cm
interaction length	16.42 cm

Table 2.2: Physical properties of the HCAL brass absorber, known as C26000/cartridge brass.

is placed outside the solenoid complementing the barrel calorimeter. Beyond $|\eta| = 3$, the forward hadron calorimeters placed at 11.2 m from the interaction point extend the pseudorapidity coverage down to $|\eta| = 5.2$ using a Cherenkov-based, radiation-hard technology. Since the calorimeter is inserted into the ends of a 3.8 T solenoidal magnet, the absorber must be made from a non-magnetic material. It must also have a maximum number of interaction lengths to contain hadronic showers, good mechanical properties and reasonable cost, leading to the choice of C26000 cartridge brass. The properties of this material are reported in Table 2.2.

2.3.4 The superconducting magnet

The superconducting magnet for CMS [27] has been designed to reach a 3.8 T field in a free bore of 6 m diameter and 12.5 m length with a stored energy of 2.6 GJ at full current. The flux is returned through a 10000 tons yoke comprising 5 wheels and 2 endcaps, composed of three disks each. The iron return yoke allows for a constant 1.8 T field also in the region outside the magnet.

2.3.5 The muon system

Muon detection is a powerful tool for recognizing signatures of interesting processes over the very high background rate expected at the LHC with full luminosity.

Therefore, as is implied by the experiment's middle name, the detection of muons is of central importance to CMS: precise and robust muon measurement was a central theme from its earliest design stages. The muon system has 3 functions: muon identification, momentum measurement and triggering. Good muon momentum resolution and trigger capability are enabled by the high-field solenoidal magnet and its flux-return yoke. The latter also serves as a hadron absorber for the identification of muons.

The CMS muon system is designed to have the capability of reconstructing the momentum and charge of muons over the entire kinematic range of the LHC. CMS uses

3 types of gaseous particle detectors for muon identification. Due to the shape of the solenoid magnet, the muon system was naturally driven to have a cylindrical, barrel section and 2 planar endcap regions. Because the muon system consists of about 25 000 m^2 of detection planes, the muon chambers had to be inexpensive, reliable, and robust.

In the barrel region, where the neutron-induced background is small, the muon rate is low, and the 3.8 T magnetic field is uniform and mostly contained in the steel yoke, drift chambers with standard rectangular drift cells are used. The barrel drift tube (DT) chambers cover the pseudorapidity region $|\eta| < 1.2$ and are organized into 4 stations interspersed among the layers of the flux return plates. The first 3 stations each contain 8 chambers, in 2 groups of 4, which measure the muon coordinate in the $r - \phi$ bending plane, and 4 chambers which provide a measurement in the z direction, along the beam line. The fourth station does not contain the z-measuring planes. The 2 sets of 4 chambers in each station are separated as much as possible to achieve the best angular resolution. The drift cells of each chamber are offset by a half-cell width with respect to their neighbour to eliminate dead spots in the efficiency. This arrangement also provides a convenient way to measure the muon time with excellent time resolution, using simple mean timer circuits, for efficient, standalone bunch crossing identification. The number of chambers in each station and their orientation were chosen to provide good efficiency for linking together muon hits from different stations into a single muon track and for rejecting background hits.

In the 2 endcap regions of CMS, where the muon rates and background levels are high and the magnetic field is large and non-uniform, the muon system uses cathode strip chambers (CSC). With their fast response time, fine segmentation, and radiation resistance, the CSCs identify muons between $|\eta|$ values of 0.9 and 2.4. There are 4 stations of CSCs in each endcap, with chambers positioned perpendicular to the beam line and interspersed between the flux return plates. The cathode strips of each chamber run radially outward and provide a precision measurement in the $r - \phi$ bending plane. The anode wires run approximately perpendicular to the strips and are also read out in order to provide measurements of η and the beam-crossing time of a muon. Each 6-layer CSC provides robust pattern recognition for rejection of non-muon backgrounds and efficient matching of hits to those in other stations and to the CMS inner tracker. Because the muon detector elements cover the full pseudorapidity interval $|\eta| < 2.4$ with no acceptance gaps, muon identification is ensured over the range corresponding to $10^\circ < \theta < 170^\circ$.

Offline reconstruction efficiency of simulated single-muon samples is typically $95 - 99\%$ except in the regions around $|\eta| = 0.25$ and 0.8 (the regions between 2 DT wheels)

and $|\eta| = 1.2$ (the transition region between the DT and CSC systems), where the efficiency drops. Negligible punchthrough reaches the system due to the amount of material in front of the muon system, which exceeds 16 interaction lengths.

Due to multiple-scattering in the detector material before the first muon station, the offline muon momentum resolution of the standalone muon system is about 9% for small values of η and p for transverse momenta up to 200 GeV. At 1 TeV the standalone momentum resolution varies between 15% and 40%, depending on $|\eta|$. A global momentum fit using also the inner tracker improves the momentum resolution by an order of magnitude at low momenta. At high momenta (1 TeV) both detector parts together yield a momentum resolution of about 5%. Note that the muon system and the inner tracker provide independent muon momentum measurements; this redundancy enhances fault finding and permits cross-checking between the systems. A crucial characteristic of the DT and CSC subsystems is that they can each trigger on the p_{T} of muons with good efficiency and high background rejection, independent of the rest of the detector. The Level-1 trigger p_{T} resolution is about 15% in the barrel and 25% in the endcap.

Because of the uncertainty in the eventual background rates and in the ability of the muon system to measure the correct beam-crossing time when the LHC reaches full luminosity, a complementary, dedicated trigger system consisting of resistive plate chambers (RPC) was added in both the barrel and endcap regions. The RPCs provide a fast, independent, and highly-segmented trigger with a sharp p_{T} threshold over a large portion of the rapidity range ($|\eta| < 1.6$) of the muon system. The RPCs are double-gap chambers, operated in avalanche mode to ensure good operation at high rates. They produce a fast response, with good time resolution but coarser position resolution than the DTs or CSCs. They also help to resolve ambiguities in attempting to make tracks from multiple hits in a chamber.

A total of 6 layers of RPCs are embedded in the barrel muon system, 2 in each of the first 2 stations, and 1 in each of the last 2 stations. The redundancy in the first 2 stations allows the trigger algorithm to work even for low-p_{T} tracks that may stop before reaching the outer 2 stations. In the endcap region, there is a plane of RPCs in each of the four stations in order for the trigger to use the coincidences between stations to reduce background, to improve the time resolution for bunch crossing identification, and to achieve a good p_{T} resolution. Finally, a sophisticated alignment system measures the positions of the muon detectors with respect to each other and to the inner tracker, in order to optimize the muon momentum resolution.

2.3.6 The trigger system

The LHC provides proton-proton and heavy-ion collisions at high interaction rates. For protons the beam crossing interval is 25 ns, corresponding to a crossing frequency of 40 MHz. Depending on luminosity, several collisions occur at each crossing of the proton bunches (approximately 20 simultaneous pp collisions at the nominal design luminosity of 10^{34} $\mathrm{cm}^{-2}\mathrm{s}^{-1}$). Since it is impossible to store and process the large amount of data associated with the resulting high number of events, a drastic rate reduction has to be achieved.

This task is performed by the trigger system, which is the start of the physics event selection process. The rate is reduced in two steps called Level-1 (L1) Trigger [28] and High-Level Trigger (HLT) [29], respectively. The Level-1 Trigger consists of custom-designed, largely programmable electronics, whereas the HLT is a software system implemented in a filter farm of about one thousand commercial processors. The rate reduction capability is designed to be at least a factor of 10^6 for the combined L1 Trigger and HLT. The design output rate limit of the L1 Trigger is 100 kHz, which translates in practice to a calculated maximal output rate of 30 kHz, assuming an approximate safety factor of three.

The L1 Trigger uses coarsely segmented data from the calorimeters and the muon system, while holding the high-resolution data in pipelined memories in the front-end electronics.

The HLT has access to the complete read-out data and can therefore perform complex calculations similar to those made in the the analysis off-line software if required for specially interesting events.

For reasons of flexibility the L1 Trigger hardware is implemented in FPGA technology where possible, but ASICs and programmable memory lookup tables (LUT) are also widely used where speed, density and radiation resistance requirements are important. A software system, the Trigger Supervisor, controls the configuration and operation of the trigger components. The L1 Trigger has local, regional and global components. At the bottom end, the Local Triggers, also called Trigger Primitive Generators (TPG), are based on energy deposits in calorimeter trigger towers and track segments or hit patterns in muon chambers, respectively. Regional Triggers combine their information and use pattern logic to determine ranked and sorted trigger objects such as electron or muon candidates in limited spatial regions. The rank is determined as a function of energy or momentum and quality, which reflects the level of confidence attributed to the L1 parameter measurements, based on detailed knowledge of the detectors and

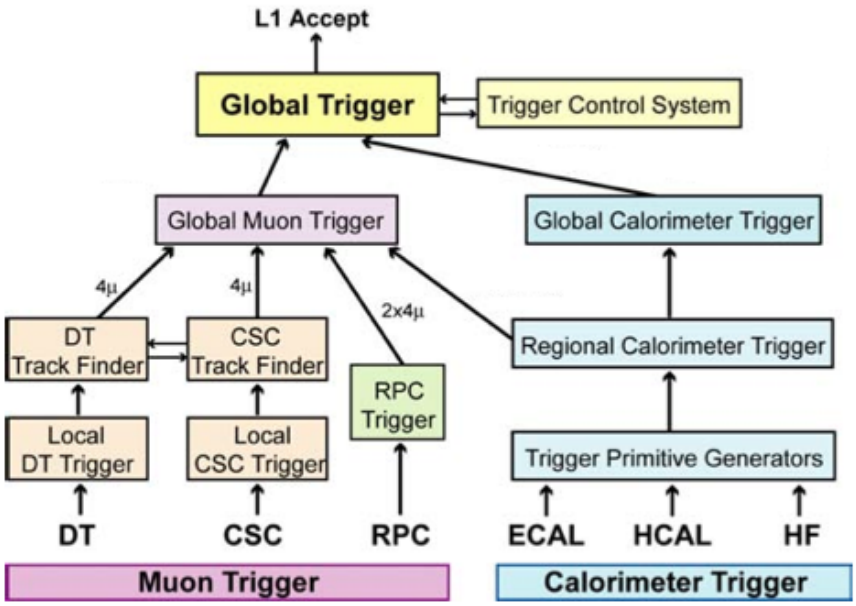

Figure 2.5: Architecture of the Level-1 Trigger.

trigger electronics and on the amount of information available. The Global Calorimeter and Global Muon Triggers determine the highest-rank calorimeter and muon objects across the entire experiment and transfer them to the Global Trigger, the top entity of the Level-1 hierarchy. The latter takes the decision to reject an event or to accept it for further evaluation by the HLT. The decision is based on algorithm calculations and on the readiness of the sub-detectors and the DAQ, which is determined by the Trigger Control System (TCS). The Level-1 Accept (L1A) decision is communicated to the sub-detectors through the Timing, Trigger and Control (TTC) system. The architecture of the L1 Trigger is depicted in Figure 2.5. The L1 Trigger has to analyse every bunch crossing. The allowed L1 Trigger latency, between a given bunch crossing and the distribution of the trigger decision to the detector front-end electronics, is 3.2 μs. The processing must therefore be pipelined in order to enable a quasi-deadtime-free operation. The L1 Trigger electronics is housed partly on the detectors, partly in the underground control room located at a distance of approximately 90 m from the experimental cavern.

Chapter 3

Top quark physics

3.1 The top quark

The top quark is the $Q = 2/3$, $t_3 = +1/2$ member of the weak-isospin doublet containing the bottom quark. Its phenomenology is driven by its large mass. Being heavier than a W boson, it is the only quark that decays weakly, i.e. into a real W boson and a d-type quark, predominantly b quarks. Therefore, it has a very short lifetime and it decays before hadronisation can occur. In addition, it is the only quark whose Yukawa coupling to the Higgs boson is order of unity. For these reasons the top quark plays a special role in the SM and in many extensions thereof. Its phenomenology provides a unique laboratory where our understanding of the strong interactions, both in the perturbative and non-perturbative regimes, can be tested. In addition, the nature of the V–A electroweak interaction at the tWb vertex means that only left-handed quarks are expected at this vertex. Thus, top quark decay products retain memory of the top quark spin orientation in their angular distributions. This turns the top quark into a powerful probe of the structure of the electroweak tWb vertex. An accurate knowledge of its properties (mass, couplings, production cross section, decay branching ratios, etc.) can bring key information on fundamental interactions at the electroweak breaking scale and beyond.

3.2 Top quark production

In hadron collisions, top quarks are produced dominantly in pairs through the processes $q\bar{q} \to t\bar{t}$ and $gg \to t\bar{t}$, at leading order in QCD, as reported in Figure 3.1. Approximately 85% of the production cross section at the Tevatron is from $q\bar{q}$ an-

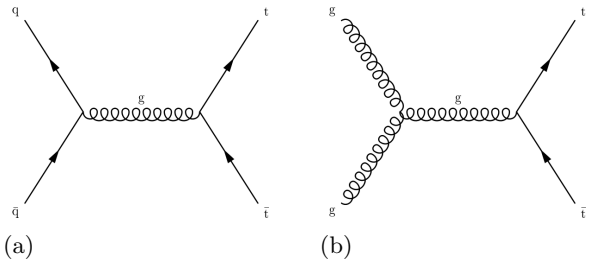

Figure 3.1: Feynman graphs for the processes of strong $t\bar{t}$ pairs production.

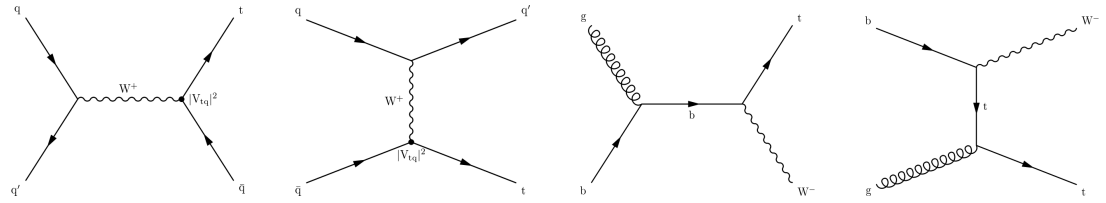

Figure 3.2: Feynman graphs for the processes of electroweak single top quark production.

nihilation, with the remainder from gluon-gluon fusion, while at LHC energies about 90% of the production is from the latter process at $\sqrt{s} = 14$ TeV ($\simeq 80\%$ at $\sqrt{s} = 7$ TeV). Assuming a top quark mass of 173.3 GeV/c^2, close to the Tevatron + LHC average [30], the resulting theoretical prediction of the top-quark pair cross-section at NNLO[1]+NNLL[2] soft gluon resummation accuracy at the Tevatron at $\sqrt{s} = 1.96$ TeV is $\sigma_{t\bar{t}} = 7.16^{+0.11}_{-0.20}(\text{scale})^{+0.17}_{-0.12}(\text{pdf})$ pb, where the first uncertainty is from scale dependence and the second from parton distribution functions. At the LHC, assuming a top quark mass of 173.2 GeV/c^2, the cross sections are: $\sigma_{t\bar{t}} = 173.6^{+4.5}_{-5.9}(\text{scale})^{+8.9}_{-8.9}(\text{pdf})$ pb at $\sqrt{s} = 7$ TeV, $\sigma_{t\bar{t}} = 247.7^{+6.3}_{-8.5}(\text{scale})^{+11.5}_{-11.5}(\text{pdf})$ pb at $\sqrt{s} = 8$ TeV and $\sigma_{t\bar{t}} = 816^{+19.4}_{-28.6}(\text{scale})^{+34.4}_{-34.4}(\text{pdf})$ pb at $\sqrt{s} = 13$ TeV [31].

Electroweak single top quark production mechanisms, namely from $q\bar{q}' \to t\bar{b}$, $qb \to q't$, mediated by virtual s-channel and t-channel W bosons, and tW-associated production, through $bg \to tW^-$, lead to smaller cross sections. Figure 3.2 reports the Feynman graphs for the processes of electroweak single top quark production. For example, t-channel production, while suppressed by the weak coupling with respect to the strong pair production, is kinematically enhanced, resulting in a sizeable cross section both at Tevatron and LHC energies. At the Tevatron, the t- and s-channel cross sec-

[1] next-to-next-to leading order
[2] next-to-next-to leading-log

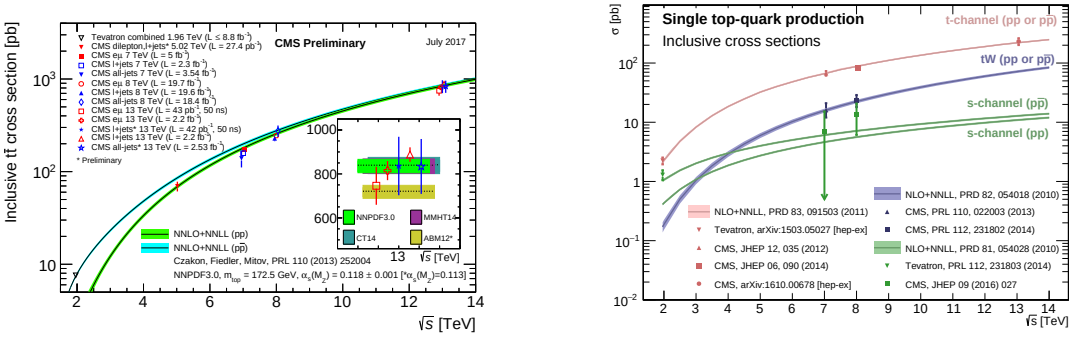

(a) (b)

Figure 3.3: The plots show the cross section measurements and predictions for inclusive $t\bar{t}$ process (a) and for single top quark process (b).

tions of top and antitop quarks are identical, while at the LHC they are not, due to the charge-asymmetric initial state. Approximate NNLO cross sections for t-channel single top quark production ($t + \bar{t}$) are calculated for $m_t = 173.3$ GeV/c^2 to be 2.06 ± 0.13 pb in $p\bar{p}$ collisions at $\sqrt{s} = 1.96$ TeV (scale and parton distribution functions uncertainties are combined in quadrature) and 65.7 ± 1.9, 87.1 ± 0.24 pb in pp collisions at $\sqrt{s} = 7$, 8 TeV, respectively, where 65% and 35% are the relative proportions of t and $\bar{t}$. Calculations at NNLO for pp collisions at $\sqrt{s} = 13$ TeV predict $\sigma_{t\text{-ch.,t}} = 134.0^{+0.7}_{-0.6}$ pb and $\sigma_{t\text{-ch.,}\bar{t}} = 80.5^{+0.3}_{-0.6}$ pb [32] (scale uncertainty is here the sole present).

For the s-channel, these calculations yield 1.03±0.05 pb for the Tevatron, and 4.5±0.2 pb, 5.5 ± 0.2 pb, and $11.36 \pm 0.18(\text{scale})^{+0.40}_{-0.45}(\text{pdf})$ pb for $\sqrt{s} = 7$, 8, and 13 TeV at the LHC, with 69% (31%) of top (antitop) quarks [33].

While negligible at the Tevatron, at LHC energies the tW-associated production becomes relevant. At $\sqrt{s} = 7$, 8, and 13 TeV, an approximate NNLO calculation gives 15.5 ± 1.2 pb, 22.1 ± 1.5 pb, and $71.7 \pm 1.8(\text{scale}) \pm 3.4(\text{pdf})$ pb ($t + \bar{t}$), with an equal proportion of top and antitop quarks [33]. Figure 3.3 reports the cross section measurements of Tevatron and LHC experiments and the predictions from the most used MC generators and shows the good agreement between measurements and predictions. Assuming $|V_{tb}| \gg |V_{td}|$, $|V_{ts}|$, the cross sections for single top production are proportional to $|V_{tb}|^2$, and no extra hypothesis is needed on the number of quark families or on the unitarity of the CKM matrix in extracting $|V_{tb}|$. In this work this assumption is released and it is followed the approach described in Sec. 5. Separate measurements of the s- and t-channel processes provide sensitivity to physics Beyond the SM (BSM).

3.3 Top quark decay

The study of the top quark decay has a central role in the SM picture. In fact, thanks to its large mass, new undiscovered particles could manifest through the top quark decay giving clues on BSM physics. Furthermore measurements of all top quark decay modes allow to constrain the magnitude of the CKM matrix elements $|V_{tb}|$, $|V_{td}|$, and $|V_{ts}|$. A deviation from the SM prediction of these physical quantities could imply a modification on the electroweak coupling or the existence of new particles.

With a mass above the Wb threshold, and $|V_{tb}| \gg |V_{td}|$, $|V_{ts}|$, the decay width of the top quark is expected to be dominated by the two-body channel $t \to Wb$. Neglecting terms of order m_b^2/m_t^2, α_s^2, and $(\alpha_s/\pi)M_W/m_t^2$ the width predicted in the SM at NLO is:

$$\Gamma_t = \frac{G_F m_t^3}{8\pi\sqrt{2}} \left(1 - \frac{M_W^2}{m_t^2}\right)^2 \left(1 + 2\frac{M_W^2}{m_t^2}\right) \left[1 - \frac{2\alpha_s}{3\pi}\left(\frac{2\pi^2}{3} - \frac{5}{2}\right)\right], \tag{3.1}$$

where m_t refers to the top quark pole mass. The width for a value of $m_t = 173.3$ GeV/c^2 is 1.35 GeV/c^2 (is used $\alpha_s(M_Z) = 0.118$) and increases with mass. The measurement performed by the CMS experiment found a value for the total decay width of $\Gamma_t = 1.36 \pm 0.02(\text{stat})^{+0.14}_{-0.11}(\text{syst})$ GeV [39]. With its correspondingly short lifetime of $\simeq 0.5 \times 10^{-24} s$, the top quark is expected to decay before top-flavoured hadrons or $t\bar{t}$-quarkonium-bound states can form. The order α_s^2 QCD corrections to Γ_t are also available, thereby improving the overall theoretical accuracy to better than 1%.

The final states for the leading pair-production process can be divided into three classes:

A. $t\bar{t} \to W^+bW^-\bar{b} \to q\bar{q}'bq''\bar{q}'''\bar{b}$, (45.7%)
B. $t\bar{t} \to W^+bW^-\bar{b} \to \ell^+\nu_\ell bq''\bar{q}'''\bar{b} + \ell^-\bar{\nu}_\ell q\bar{q}'b\bar{b}$, (43.8%)
C. $t\bar{t} \to W^+bW^-\bar{b} \to \ell^+\nu_\ell b\ell^-\bar{\nu}_\ell\bar{b}$, (10.5 %)

The quarks in the final state evolve into jets of hadrons. A, B, and C are referred to as the all-jets, lepton+jets (ℓ+jets), and dilepton ($\ell\ell$) channels, respectively. Their relative contributions, including hadronic corrections, are given in parentheses assuming lepton universality. While ℓ in the above processes refers to e, μ, or τ, most of the analyses distinguish the e and μ from the τ channel, which is more difficult to reconstruct. In addition to the quarks resulting from the top quark decays, extra QCD radiation (quarks and gluons) from coloured particles in the event can lead to extra jets. The number of jets reconstructed in the detectors depends on the decay kinematics, as well as on the algorithm for reconstructing jets used by the analysis. Information on the transverse momenta of neutrinos is obtained from the imbalance in transverse momentum measured

in each event (missing p_{T}, which is also referred to missing E_T).

The identification of top quarks in the electroweak single top quark channel is much more difficult than in the $\mathrm{t\bar{t}}$ channel, due to a less distinctive signature and significantly larger backgrounds, mostly due to $\mathrm{t\bar{t}}$ and $\mathrm{W}+\mathrm{jets}$ production. Fully exclusive predictions via Monte Carlo generators for the $\mathrm{t\bar{t}}$ and single top quark production processes at NLO accuracy in QCD, including top quark decays, are available through the *aMC@NLO* [34] and *POWHEG 2.0* [35–38] methods. Besides fully inclusive QCD or EW top quark production, more exclusive final states can be accessed at hadron colliders, whose cross sections are typically much smaller, yet can provide key information on the properties of the top quark.

3.4 Top quark properties

3.4.1 Mass

The most precisely studied property of the top quark is its mass. This is a fundamental parameter of the SM that plays a fundamental role in all radiative corrections to SM loops, due to it being the highest of all particle masses. The top quark mass has been measured in $\mathrm{t\bar{t}}$ processes in the lepton+jets, the dilepton, and the all-jets channel of by all four Tevatron and LHC experiments. The lepton+jets channel yields the most precise single measurements because of good signal to background ratio (in particular after b-tagging) and the presence of only a single neutrino in the final state. The momentum of a single neutrino can be reconstructed (up to a quadratic ambiguity) via the missing E_T measurement and the constraint that the lepton and neutrino momenta reconstruct to the known W boson mass. In the large data samples available at the LHC, measurements in the dilepton channel can be competitive and certainly complementary to those in the lepton+jets final state. The world average of measurement of the top quark mass [30] is:

$$m_{\mathrm{t}} = 173.34 \pm 0.27 \pm 0.24 \pm 0.76 \text{ GeV/c}^2.$$

ATLAS and CMS also performed measurements of the top quark mass in event samples enriched in single-top t-channel processes. In particular, CMS performed the most precise single measurement of the top quark mass corresponding to:

$$m_{\mathrm{t}} = 172.44 \pm 0.13 \pm 0.47 \text{ GeV/c}^2$$

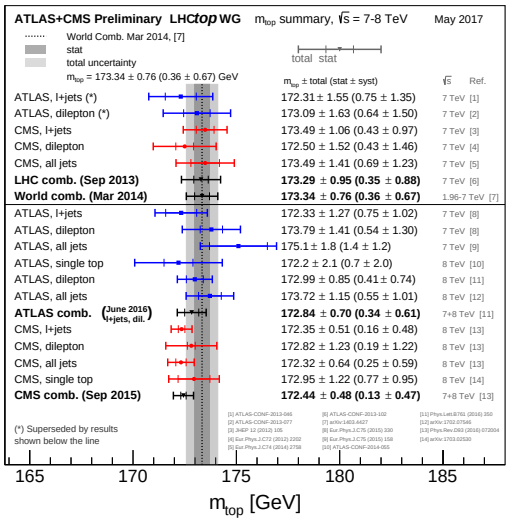

Figure 3.4: Summary of CMS and ATLAS m_{t} measurements.

Figure 3.4 reports an overview of the most precise top quark mass measurements at LHC.

3.4.2 Electric charge

The top quark is the only quark whose electric charge has not been measured through production at threshold in e^+e^- collisions. Since the CDF and D0 analyses on top quark production did not associate the b, $\bar{\mathrm{b}}$, and $\mathrm{W}^{\pm}$ uniquely to the top or antitop, decays such as $\mathrm{t} \to \mathrm{W}^+\bar{\mathrm{b}}$, $\bar{\mathrm{t}} \to \mathrm{W}^-\mathrm{b}$ were not excluded. A charge 4/3 quark of this kind is consistent with current electroweak precision data. There are some exotic BSM models that predict a charge 4/3 top quark. The measurements of the four experiments of Tevatron and LHC exclude these scenarios with high confidence level [40–43]. Those measurements do measure the strength of the $\mathrm{t}\gamma\mathrm{t}$ coupling, which is regulated by the top quark charge, in $\mathrm{t}\bar{\mathrm{t}}$ processes.

3.4.3 Spin

One of the unique features of the top quark is that it decays before its spin can be flipped by the strong interaction. Thus the top quark polarisation is directly observable via the angular distribution of its decay products. Hence, it is possible to define and measure observables sensitive to the top quark spin and its production mechanism. Although the top and antitop quarks produced by strong interactions in hadron collisions

are essentially unpolarised, the spins of t and $\bar{\text{t}}$ are correlated. For QCD production at threshold, the $\text{t}\bar{\text{t}}$ system is produced in a $^3S_1$ state with parallel spins for $\text{q}\bar{\text{q}}$ annihilation or in a $^1S_0$ state with antiparallel spins for gluon-gluon fusion. Hence, the situations at the Tevatron and at the LHC are complementary. However, at the LHC production of $\text{t}\bar{\text{t}}$ pairs at large invariant mass occurs primarily via fusion of gluons with opposite helicities, and the $\text{t}\bar{\text{t}}$ pairs so produced have parallel spins as in production at the Tevatron via $\text{q}\bar{\text{q}}$ annihilation. The direction of the top quark spin is 100% correlated to the angular distributions of the down-type fermion (charged leptons or d-type quarks) in the decay. The joint angular distribution:

$$\frac{1}{\sigma}\frac{d^2\sigma}{d(\cos\theta_+)d(\cos\theta_-)} = \frac{1+\kappa\cos\theta_+\cos\theta_-}{4}, \tag{3.2}$$

where θ_+ and θ_- are the angles of the daughters in the top quark rest frame with respect to a particular spin quantization axis, is a very sensitive observable to deviations from the SM. The maximum for κ, at the Tevatron, is found in the off-diagonal basis, while at the LHC is found in the helicity basis. In the helicity basis the spin quantization axis is along the top quark direction in the $\text{t}\bar{\text{t}}$ rest frame, instead in the off-diagonal basis, it makes an angle ψ with the direction of the beam, which is related to the diffusion angle θ by the relationship:

$$\tan\psi = \frac{\beta^2\sin\theta\cos\theta}{1-\beta^2\sin^2\theta}, \tag{3.3}$$

where β is the top quark velocity in the $\text{q}\bar{\text{q}}$ rest frame. For $\beta \to 1$ the off-diagonal basis tends to be aligned to the helicity basis. The measurements of spin correlation performed by the four experiments of Tevatron and LHC are consistent with the SM predictions [44–47].

3.4.4 Polarisation

In electroweak t-channel single top quark production the SM predicts that produced top quarks are highly polarised, as a consequence of the V–A coupling structure, along the direction of the momentum of the spectator quark (q'), which recoils against the top quark. The top quark spin asymmetry:

$$A_X \equiv \frac{1}{2}P_t\alpha_X = \frac{N(\uparrow)-N(\downarrow)}{N(\uparrow)+N(\downarrow)} \tag{3.4}$$

is used to probe the coupling structure, where p_T represents the top quark polarisation in production and α_X denotes the degree of the angular correlations of one of its decay

products, denoted as X, with respect to the spin of the top quark, the so-called spin-analysing power. For $X = \ell$, $\alpha_X = 1$, so leptons are the best candidate. The variables $N(\uparrow)$ and $N(\downarrow)$ are defined, for each top quark decay product from the decay chain $\mathrm{t} \to \mathrm{bW} \to \mathrm{b}\ell\nu$, as the number of instances in which that decay product is aligned or antialigned, respectively, relative to the direction of the recoiling spectator quark momentum. The angle between a top quark decay product X(W, ℓ, ν, or b) and an arbitrary polarisation axis $\vec{s}$ in the top quark rest frame, θ^*_X, is distributed according to the following differential cross section:

$$\frac{1}{\sigma}\frac{d\sigma}{d\cos\theta^*_X} = \frac{1}{2}(1 + P_{\mathrm{t}}^{(\vec{s})}\alpha_X \cos\theta^*_X) = \left(\frac{1}{2} + A_X \cos\theta^*_X\right), \tag{3.5}$$

where variable $P_{\mathrm{t}}^{(\vec{s})}$ denotes the single top quark polarisation along the chosen axis. CMS performed this measurements and the result, shown in Figure 3.5, is consistent with the SM predictions [48]. Measurements of the polarisation of top quarks in $\mathrm{t\bar{t}}$ production are made in one or two lepton final states, assuming that the polarisation is introduced by a CP-conserving (CPC) or maximally CP-violating (CPV) process. The polarisation is extracted through an asymmetry, A_P, in the angular distribution of the two leptons, A_P, defined as:

$$A_P = \frac{N(\cos\theta^*_\ell > 0) - N(\cos\theta^*_\ell < 0)}{N(\cos\theta^*_\ell > 0) + N(\cos\theta^*_\ell < 0)}. \tag{3.6}$$

The polarisation, P in the helicity basis is given by $P = 2A_P$ and results negligible according to the SM prediction.

In this thesis it is referred to θ^*_X as θ^*_{pol} and X stands for electron and muon.

3.4.5 W boson helicity in top quark decay

The SM dictates that the top quark has the same vector-minus-axial-vector (V–A) charged-current weak interactions $\left(-i\frac{g}{\sqrt{2}}\mathrm{V_{tb}}\gamma^\mu\frac{1}{2}(1-\gamma^5)\right)$ as all the other fermions. Nevertheless, because of its short lifetime, its spin is not lost and is accessible via the decay products. The polarisation of the W boson from top quark decays is sensitive to non-SM tWb couplings. Given the fact that the W boson is produced with left-handed, right-handed or longitudinal helicity, the relation $\Gamma(\mathrm{t} \to \mathrm{Wb}) = \Gamma_L + \Gamma_R + \Gamma_0$ holds for the corresponding partial widths of top quark decay. For a W boson decaying into a lepton and a neutrino, the variable θ^*_ℓ is defined in the top quark rest-frame as the angle between the lepton 3-momenta in the W boson rest-frame and the 3-momenta of W boson. The W helicity fractions, $F_{L,R,0} = \frac{\Gamma_{L,R,0}}{\Gamma}$, are involved in the distribution of

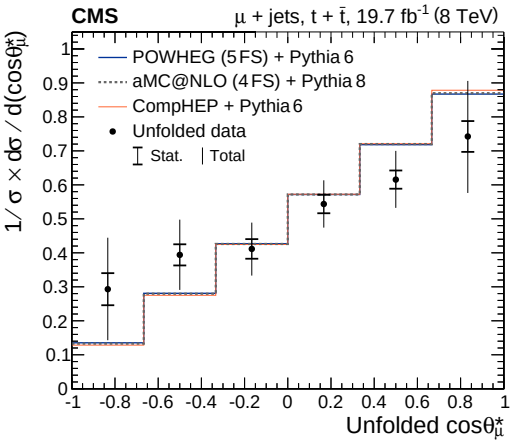

Figure 3.5: The normalised differential cross section as a function of unfolded $\cos\theta^*_\mu$ for top quark and antiquark combined, compared to the predictions.

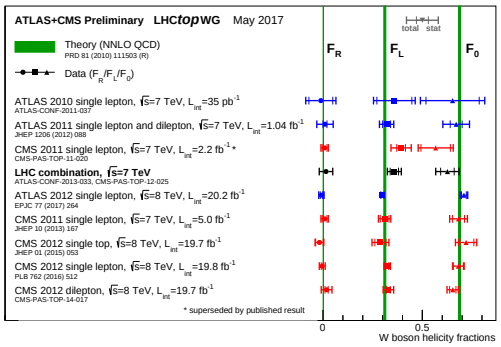

Figure 3.6: Summary of measured W helicity fractions by ATLAS and CMS at 7 and 8 TeV, compared to the respective theory predictions.

$\cos\theta^*_\ell$:

$$\rho(\cos\theta^*_\ell) \equiv \frac{1}{\Gamma}\frac{d\Gamma}{d\cos\theta^*_\ell} = \frac{3}{8}(1-\cos\theta^*_\ell)^2 F_L + \frac{3}{8}(1+\cos\theta^*_\ell)^2 F_R + \frac{3}{4}\sin^2\theta^*_\ell F_0, \qquad (3.7)$$

and therefore can be extracted from this distribution. The SM predictions for the W boson helicity fractions at next-to-next-to-leading-order (NNLO) in the strong coupling constant, including the finite b quark mass and electroweak effects, are $F_L = 0.311 \pm 0.005$, $F_0 = 0.687 \pm 0.005$, and $F_L = 0.0017 \pm 0.0001$ [49] and the experimental results [50–53] are so far in good agreement with them, as can be seen in Figure 3.6. In this thesis it is referred to θ^*_ℓ as θ^*_{hel}.

Chapter 4

Physics objects selection and reconstruction

The aim of the selection of this analysis is to obtain a single-top quark t-channel enriched sample. The final state of this process is characterized by the presence of exactly one isolated lepton, two or more jets, one or two of which can be identified as coming from the hadronisation of a b quark. The Feynman graphs of the processes sought for such events are reported in Figure 4.1. The graph depicted in Figure 4.1(a) represents the case in which the incoming gluon splits into two quarks and the top quark decays according to the usual, and more common, chain $t \to bW \to b\ell\nu$. The graph depicted in Figure 4.1(b) is the same as the 4.1(a) except for the decay that is the one according to the chain $t \to qW \to q\ell\nu$ where q can be a d or a s quark. The topology of these two graphs is called 4 flavour scheme, 4FS, in jargon and is used to produce the single-top quark t-channel MC samples. The graph depicted in Figure 4.1(c) represents the case in which the incoming d quark is a valence one and the top quark decays according to $t \to bW \to b\ell\nu$. This topology is called 5 flavour scheme, 5FS, in jargon,

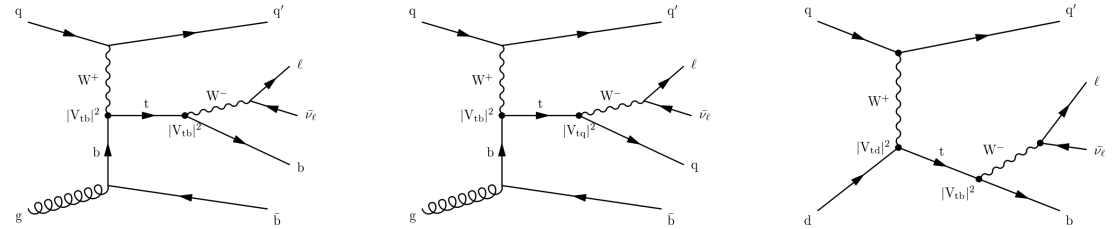

Figure 4.1: Feynman graphs for the signal:

and it is used to produce the MC samples for the single-top t-channel with a d quark in production by altering the value of $|V_{td}|^2$, which is considered equal to 1. Signal samples are produced with *POWHEG 2.0*.

4.1 Physics objects selection

The reconstruction of all physics objects is done through the Particle Flow, PF for short, algorithm [54]. The PF reconstructs and identifies all stable particles in the event, i.e., electrons, muons, photons, charged hadrons and neutral hadrons, with a thorough combination of all CMS sub-detectors towards an optimal determination of their direction, energy and type. This list of individual particles is then used, as if it came from a MC event generator, to build jets (from which the quark and gluon energies and directions are inferred), to determine the missing transverse energy $\not{E}_T$ (which gives an estimate of the direction and energy of the neutrinos and other invisible particles), to reconstruct and identify taus from their decay products, to quantify charged lepton isolation with respect to other particles, to tag b jets, etc. An interaction point is a point in which the directions of the reconstructed tracks of at least four particles converge. For a primary vertex is is required that it is reconstructed from at least four tracks, requiring the track fit to have $n_{dof} \geq 5$, with $|z_{PV}| < 24$ cm and $\rho_{PV} < 2$ cm, where $|z_{PV}|$ and ρ_{PV} are the vertex distance with regard to the nominal interaction point along the z axis, and in the transverse plane respectively. Muon and electrons must pass the High Level Trigger selection. It selects all isolated online muon candidates with $p_T > 24$ GeV/c and all online electrons candidates with $p_T > 32$ GeV/c in the $|\eta| < 2.1$ range. Efficiencies for this trigger in simulation are corrected using data-to-MC correction factors obtained from a *Tag and Probe* method.

4.1.1 Tight muons

Reconstructed muons within the pseudorapidity range of $|\eta| < 2.4$ and with a transverse momentum $p_T > 26$ GeV/c are selected. Muons must have at least one valid hit in the muon chambers to suppress muons from decays in flight and, in order to guarantee a good p_T measurement, muon candidates are required to have more than 5 valid hits in the silicon tracker, out of which at least one in the pixel detector. Additional isolation requirements are applied to discriminate between prompt muons[1] and muons coming

[1] Muons coming from a hard interaction, typically from a W, Z, decay or a Drell-Yan event.

from hadronic decays in jets, by applying a requirement on the I^{μ}_{rel} variable, defined as:

$$I^{\mu}_{\text{rel}} = \frac{I^{\text{ch.h}} + \max[(I^{\gamma} + I^{\text{n.h}} - 0.5 \times I^{\text{PU}}), 0]}{p_{\text{T}}}, \tag{4.1}$$

where $I^{\text{ch.h}}$, I^{γ}, $I^{\text{n.h}}$, and I^{PU} are respectively, the scalar p_{T} sums of the charged hadrons, photons, neutral hadrons, and charged hadrons associated with pileup vertices. The sums are computed in a cone of $\Delta R = \sqrt{(\Delta\phi)^2 + (\Delta\eta)^2} = 0.4$ around the muon direction. The isolation requirement is $I^{\mu}_{\text{rel}} < 0.06$.

4.1.2 Tight electrons

Good electron candidates with tight selection requirements ("tight" electrons) are selected by requiring an electron reconstructed matching a track with the clusters in the calorimeters, with $E_{\text{T}} > 35$ GeV, $|\eta| < 2.1$, and an additional selection chain made by 9 variables and optimized in a cut-based approach. Any event with one or more electron candidates as defined above is rejected. Additional isolation requirements are applied to discriminate between prompt electrons and electrons coming from hadronic decays in jets, by applying a requirement on the $I^{\text{e}}_{\text{rel}}$ variable, defined as:

$$I^{\text{e}}_{\text{rel}} = \frac{I^{\text{ch.h}} + \max[(I^{\gamma} + I^{\text{n.h}} - \rho \times A), 0]}{p_{\text{T}}}, \tag{4.2}$$

where ρ is the average energy density not clustered in jets, measured event-by-event, by the cone area A. The sums are computed in a cone of $\Delta R = \sqrt{(\Delta\phi)^2 + (\Delta\eta)^2} = 0.3$ around the electron direction. The isolation requirement is $I^{\text{e}}_{\text{rel}} < 0.0588$ for barrel electrons and $I^{\text{e}}_{\text{rel}} < 0.0571$ for endcap electrons.

4.1.3 Loose muons

An addition category is defined in order to veto events with further charged leptons with a looser selection requirements. Any event with a further muon, within $|\eta| < 2.4$, having $p_{\text{T}} > 10$ GeV/c, and lying within $I^{\mu}_{\text{rel}} < 0.2$, is rejected.

4.1.4 Loose electrons

The loose electron candidate selection used for the veto of secondary electrons has the kinematic requirements are $E_{\text{T}} > 15$ GeV, $|\eta| < 2.5$. The selection chain for electron identification used for such electrons is tuned to have a higher efficiency, thus resulting in a tighter cut on the veto.

4.1.5 Jets

Jets are reconstructed by applying the anti-k_{T} clustering algorithm [55] with a cone size of 0.4, on PF candidates after rejecting charged hadrons that are associated to a pileup primary vertex. These jets have standard multi-level jet energy corrections (JEC) applied and a p_{T} cut at 10 GeV/c. The jet energy is scaled by a factor that describes the detector response depending on the transverse energy and the pseudorapidity of the jet [56]. To reduce contamination from pileup events, charged particle candidates not associated to the main primary vertex are subtracted event by event. The energy of the jet is then corrected by the amount of energy deposited by neutral pileup hadrons in the jet area.

Jets within $|\eta| < 4.7$ whose calibrated transverse energy is greater than 40 GeV and which pass a set of quality requirements are selected. Muons and electrons are vetoed by requiring a distance in the $\eta - \phi$ plane of at least ΔR greater than 0.4 with respect to tight muon or electron candidate. The requirements are different depending on the pseudorapidity of the jets, as different detector technologies are involved.

4.1.6 b-Tagging

Several algorithms for identification of jets originating from b quarks are available in CMS. Some of them exploit the long B hadrons lifetime, others their semi-leptonic decay modes and others make use of kinematic variables related to the high B meson mass and hard b quark fragmentation function. More specifically, b-tagging algorithms are based on displaced tracks (*track counting taggers*, *jet probability tagger*), the presence of secondary vertices (*secondary vertex taggers*) or soft leptons (*soft lepton taggers*) or on a combination of these (*combined secondary vertex taggers*). The combined secondary vertex algorithm uses track-based lifetime information together with secondary vertices inside the jet to provide a MVA discriminator for b jet identification (*Combined MVA v2*). For this study it is used the CMVAv2 algorithm at the tight working point corresponding to a threshold set to 0.9432 and a 0.1% efficiency for jets not coming from b quarks (*mistag efficiecy*).

4.1.7 Missing transverse energy

Defined in an analogous way as PF-based jets, PF-based $\not\!\!E_{\mathrm{T}}$ is the opposite of the vectorial sum of the transverse momenta of the identified PF particles. Data-driven corrections of energy offset are also applied to PF-based $\not\!\!E_{\mathrm{T}}$.

Object	Requirements	Counts	
		μ	e
Tight muon	$p_{\mathrm{T}} > 26$ GeV/c $\quad \lvert\eta\rvert < 2.4 \quad I^{\mu}_{\mathrm{rel}} < 0.06$	1	0
Loose muon	$p_{\mathrm{T}} > 10$ GeV/c $\quad \lvert\eta\rvert < 2.4 \quad I^{\mu}_{\mathrm{rel}} < 0.2$	0	0
Tight electron	$E_{\mathrm{T}} > 35$ GeV $\quad \lvert\eta\rvert < 2.1 \quad I^{\mathrm{e}}_{\mathrm{rel}} < 0.0588$ (B) $\quad I^{\mathrm{e}}_{\mathrm{rel}} < 0.0571$ (E)	0	1
Loose electron	$E_{\mathrm{T}} > 15$ GeV $\quad \lvert\eta\rvert < 2.5 \quad I^{\mathrm{e}}_{\mathrm{rel}} < 0.2$	0	0
Jet	$E_{\mathrm{T}} > 40$ GeV $\quad \lvert\eta\rvert < 4.7$	2(3)	
b-Jet	$E_{\mathrm{T}} > 40$ GeV $\quad \lvert\eta\rvert < 2.4 \quad$ CMVA ≥ 0.9432	1(2)	

Table 4.1: Summary of all the physics objects defined, their corresponding selection requirements, and the number of candidate required for the muon and electron channels.

4.1.8 Transverse W boson mass

To further suppress contributions from processes where the muon does not come from a leptonically decaying W boson, a selection based the reconstructed transverse W boson mass $m_{\mathrm{T}}^{\mathrm{W}}$ is made. The transverse W boson mass is defined as:

$$m_{\mathrm{T}} = \sqrt{\left(p_{\mathrm{T},\ell} + \not{p}_{\mathrm{T},\nu}\right)^2 - \left(p_{x,\ell} + \not{p}_{x,\nu}\right)^2 - \left(p_{y,\ell} + \not{p}_{y,\nu}\right)^2}, \tag{4.3}$$

where the transverse momentum components of the neutrino are approximated by the components of the missing transverse energy vector, $\vec{\not{E}}_{\mathrm{T}}$.

All the physics objects and their selection requirements are summed in Table 4.1.

4.2 Top quark reconstruction

In order to analyse the kinematics of singly produced top quarks, the four-vector of the top quarks have to be reconstructed from the decay products. All top-quark decay products are reconstructed in the detector, except for the neutrino which escapes unobserved. While the transverse momentum of the neutrino can be inferred from the missing transverse energy, its longitudinal momentum has to be derived based on extra assumptions. Once the leptonically decaying W boson is reconstructed the selected jets have to be assigned to the final state quarks in the top quark decay chain.

4.2.1 W boson reconstruction

The first step in the reconstruction of the top quark from its decay products is the reconstruction of the W boson. We assume that the x and y components of the missing transverse energy are entirely due to the escaping neutrino, and apply the W-mass

constraint in order to extract the unknown z component $p_{z,\nu}$:

$$m_{\mathrm{W}}^2 = \left(E_\ell + \sqrt{\not{E}_{\mathrm{T}}^2 + p_{z,\nu}^2}\right)^2 - \left(\vec{p}_{\mathrm{T},\ell}^{\,2} + \vec{\not{E}}_{\mathrm{T}}^{\,2}\right)^2 - \left(p_{z,\ell}^2 + p_{z,\nu}^2\right)^2. \tag{4.4}$$

This equation has in general two solutions:

$$p_{z,\nu} = \frac{\Lambda \cdot p_{z,\ell}}{p_{\mathrm{T},\ell}^2} \pm \sqrt{\frac{\Lambda^2 \cdot p_{z,\ell}^2}{p_{\mathrm{T},\ell}^4} - \frac{E_\ell^2 \cdot \not{E}_{\mathrm{T}}^2 - \Lambda^2}{p_{\mathrm{T},\ell}^2}}, \tag{4.5}$$

where:

$$\Lambda = \frac{m_{\mathrm{W}}^2}{2} + \vec{p}_{\mathrm{T},\ell} \cdot \vec{\not{E}}_{\mathrm{T}}. \tag{4.6}$$

In most of the cases this leads to two real solutions for $p_{z,\nu}$ and the solution with the smallest absolute value is chosen. For some events the discriminant in Eq. 4.5 becomes negative leading to complex solutions for $p_{z,\nu}$. In this case the imaginary component is eliminated by modification of $p_{x,\nu}$ and $p_{y,\nu}$ so that $m_{\mathrm{T}} = m_{\mathrm{W}}$, while still respecting the m_{W} constraint. This is achieved by imposing that the determinant, and thus the square-root term in Eq. 4.5, are null. This condition gives a quadratic relation between $p_{x,\nu}$ and $p_{y,\nu}$ with two possible solutions, and one remaining degree of freedom. The solution is chosen by finding the neutrino transverse momentum $\vec{p}_{\mathrm{T},\nu}$ that has the minimum vectorial distance from the in the $\not{p}_x - \not{p}_y$ plane. Top quark candidates are reconstructed by selecting one of the jets to accompany the W boson decay. Multiple top quark candidates can be reconstructed, in the different regions, depending on the hypothesis on the origin of the jet in the event.

4.3 Background description

The most important backgrounds mimicking the t-channel final states are:

- $\mathrm{t\bar{t}}$: processes where a $\mathrm{t\bar{t}}$ quark pair is produced are the dominant background. In particular events where one t quark decays leptonically, namely through the chain $\mathrm{t} \to \mathrm{Wb} \to \mathrm{b}\ell\nu$, and the other top quark decays hadronically, namely through the chain $\mathrm{t} \to \mathrm{Wb} \to \mathrm{bq\bar{q}}$, have several features in common with signal events due to the presence of a real leptonic top decay. Such events are also called semi-leptonic $\mathrm{t\bar{t}}$ events in jargon. Also events with two leptonic top decay could be a background in one of the two leptons didn't pass the selection required. The $\mathrm{t\bar{t}}$ jet multiplicity is in general higher than for the t-channel, and this reduces the contamination

from this background.

- W + jets: processes where a W boson is produced in association to jets are an important source of background. In particular, processes where the W boson decays through $W \to \ell\nu$ and are produced in association to a c quark or $b\bar{b}$ or $c\bar{c}$ quark pair could be misidentified as signal events. Also events where W boson is associated to light partons (u, d, s quarks and gluons), can mimic signal events, in case one of the jets stemming from a light parton mimics the behaviour of a b jet.

- Multi-jet QCD: events where a well-isolated muon or electron is present and the jet-environment reproduces the signal topology in hard QCD scatterings are very rare, nevertheless, due to the much higher cross section of such multi-jet QCD processes, the contribution of such events to the background is not negligible. In this case the variable $m_{\mathrm{T}}^{\mathrm{W}}$ is very powerful in discriminating this type of contamination.

- *s*- and tW channels: the other single top quark processes, in particular the tW-channel, produce a non-negligible contamination in the signal region. Such backgrounds, like the $t\bar{t}$ background, share with the *t*-channel the decay chain of the top quark.

- VV, Z+jets: diboson processes like WW, WZ, and ZZ, or Z+jets processes are also minor sources of backgrounds which can reproduce in some cases the *t*-channel topology. However either the low cross section for VV processes (with V = W or Z), or the extremely narrow phase space for Z+jets processes passing the cuts, consistently limit the contamination from such processes.

- Other SM possible backgrounds (multi-boson production, multi-top production, SM Higgs) have a much smaller cross section than the *t*-channel, and in general their contribution is limited to very rare topologies. They are therefore considered negligible.

Chapter 5

Analysis strategy

There are three contributions to the inclusive single top quark t-channel cross section:

$$\begin{aligned}\sigma_{t\text{-channel}} &= \sigma_{t-\text{ch.,b}} + \sigma_{t-\text{ch.,d}} + \sigma_{t-\text{ch.,s}} = \\ &= \alpha|\mathrm{V_{tb}}|^2 + \beta|\mathrm{V_{td}}|^2 + \gamma|\mathrm{V_{ts}}|^2, \end{aligned} \tag{5.1}$$

where the term $|\mathrm{V_{tq}}|^2$, where q stands for b, s, or d is factored out from the cross section. The diagrams corresponding to each process with a different quark in the initial state can be found in Figure 4.1 of Chapter 4. The values of the quantities in Eq. 5.1 are reported in Table 5.1.

Vertex	tWb	tWd	tWs
$\lvert\mathrm{V_{tq}}\rvert$	$0.999119^{+0.000024}_{-0.000012}$	$0.008575^{+0.000076}_{-0.000098}$	$0.04108^{+0.00030}_{-0.00057}$
$\lvert\mathrm{V_{tq}}\rvert^2$	$0.998239^{+0.000048}_{-0.000024}$	$0.000074^{+0.000013}_{-0.000017}$	$0.0016876^{+0.0000025}_{-0.0000047}$
$\sigma_{t-\text{ch.,q}}$	216.99 ± 5.8	1046.29 ± 10	498.61 ± 10

Table 5.1: Values of matrix elements inferred from low energy regime measurements, with the respective values of top quark decay branching fractions in the first two rows. Cross sections for inclusive t-channel production in the third row, obtained with *POWHEG 2.0* when the respective $|\mathrm{V_{tq}}|$ is put equals to unity.

When the top quark decay modes are considered, the cross section is multiplied for

the branching fraction BR(t → Wq) that can be evaluated[1] as:

$$\mathrm{BR}(\mathrm{t} \to \mathrm{Wq}) = \frac{|\mathrm{V_{tq}}|^2}{|\mathrm{V_{td}}|^2 + |\mathrm{V_{ts}}|^2 + |\mathrm{V_{tb}}|^2}. \tag{5.2}$$

By assuming $|\mathrm{V_{td}}|^2 + |\mathrm{V_{ts}}|^2 + |\mathrm{V_{tb}}|^2 = 1$, one obtains:

$$\begin{aligned}
\sigma_{t\text{-channel}} \times \mathrm{BR}(\mathrm{t} \to \mathrm{Wq}) \approxeq{}& \alpha|\mathrm{V_{tb}}|^2|\mathrm{V_{tb}}|^2 + && (5.3)\\
&+ \alpha|\mathrm{V_{tb}}|^2\left(|\mathrm{V_{td}}|^2 + |\mathrm{V_{ts}}|^2\right) + && (5.4)\\
&+ \beta|\mathrm{V_{td}}|^2|\mathrm{V_{tb}}|^2 && (5.5)\\
&+ \gamma|\mathrm{V_{ts}}|^2|\mathrm{V_{tb}}|^2, && (5.6)
\end{aligned}$$

where the $|\mathrm{V_{tq}}|^2\ |\mathrm{V_{tq}}|^2$, with q=d, s, contributions were neglected in this approximation. When the measurement is performed the selection efficiencies, $\epsilon^{sel.}_{\mathrm{q,q}}$, obtained from the MC simulations, have to been taken into account and, finally, one has:

$$\begin{aligned}
\sigma_{t\text{-channel}} \times \mathrm{BR}(\mathrm{t} \to \mathrm{Wq}) \approxeq{}& \alpha|\mathrm{V_{tb}}|^2|\mathrm{V_{tb}}|^2\epsilon^{sel.}_{\mathrm{b,b}} + && (5.7)\\
&+ \alpha|\mathrm{V_{tb}}|^2\left(|\mathrm{V_{td}}|^2\epsilon^{sel.}_{\mathrm{b,d}} + |\mathrm{V_{ts}}|^2\epsilon^{sel.}_{\mathrm{b,s}}\right) + && (5.8)\\
&+ \beta|\mathrm{V_{td}}|^2|\mathrm{V_{tb}}|^2\epsilon^{sel.}_{\mathrm{d,b}} && (5.9)\\
&+ \gamma|\mathrm{V_{ts}}|^2|\mathrm{V_{tb}}|^2\epsilon^{sel.}_{\mathrm{s,b}}. && (5.10)
\end{aligned}$$

All the previous approaches[57, 58] consider $|\mathrm{V_{tb}}| \gg |\mathrm{V_{td,s}}|$ and neglect the latter terms. This assumption stems from the indirect determinations of $\mathrm{V_{td}}$ and $\mathrm{V_{ts}}$ from independent lower energy measurements. However, this assumption ignores any BSM modifications to the magnitude of $\mathrm{V_{td}}$ and $\mathrm{V_{ts}}$ happening in production, and does introduce biases in measurements of $|\mathrm{V_{tb}}|$.

5.1 Signal and control regions

The majority of t-channel events populate categories with 2 or 3 jets, as defined in Sec. 4.1. The category with 2-jets–1-tag is populated by events with $\mathrm{V_{tb}}$ in production and decay, where the one reconstructed b jet comes in the majority of cases (85%) from top quark decays, and for the remaining cases from the second b jet from gluon splitting. This means that the jet from the second b quark hadronisation fails either the jet p_{T}

[1] This is an approximation neglecting all non-W decays of top quarks and the difference in mass between b, s, and d quarks.

requirement or the b-tag requirement, or both. Events where either in production or in decay the V_{td} or V_{ts} are present do populate this region as well, with the selected b jet either coming from top quark decay, or it coming from the secondary b quark from gluon splitting. The category with 3-jets–1-tag is also populated by t-channel processes, and differs from the 2-jets–1-tag in the fact that it accommodates events in the higher end of the p_{T} spectrum of the jet from gluon splitting. For both the 2-jets–1-tag and 3-jets–1-tag categories, for processes where the top decays happen through tWd, s vertexes, the jet coming from the top quark should not pass the b-tagging requirement as it does stem from the hadronisation of a light quark, while it is expected to pass the b-tagging requirement in all other cases according to the efficiency of the tagging algorithm. In order to discriminate amongst signal processes, top quark candidates are therefore defined for each jet of the event, and variables stemming from properties of the top quark and its decays are used to discriminate between top quark candidate hypotheses. To recover discriminating power amongst the different t-channel processes, in the 2-jets–1-tag additional jets with $20 < p_{\mathrm{T}} < 40$ GeV/c are studied and the hardest amongst them is used to reconstruct a corresponding top quark candidate. For signal events, one of the distinct features that allows to discriminate between jets from top quark decays and jets produced from the light quark recoiling against the top quark is the pseudorapidity of the jet. In order to reduce combinatoric background due to top quark reconstructed from the spectator jet, the signal region is therefore defined by requiring the most forward jet to have $|\eta| > 2.4$, and thus removing this jet from the list of candidates for top quark reconstruction.

Instead the 3-jets–2-tags is dominated in a relevant way by the $\mathrm{t\bar{t}}$ processes or single top quark t-channel processes with the presence of the tWb vertex both in production and decay. This category is used as an enriched region in $\mathrm{t\bar{t}}$ and single top quark with tWb in production as decay in the fit procedure described in the Sec. 5.7.

The variables used for this analysis are the following:

- $|\eta_{j'}|$: the absolute value of the pseudorapidity of the light jet recoiling from the top quark;
- $m_{\mathrm{T}}^{\mathrm{W}}$: the reconstructed W boson transverse mass defined as in the Sec. 4.1.8;
- m_{tX}: the reconstructed top quark mass as defined in Sec. 4.2, where X is the b jet and the extra jet for the n-jets–1-tag and it is the first and the second b jet in the 3-jets–2-tags;
- $m_{\ell\mathrm{j}}$: the lepton + the extra jet reconstructed mass;

- $m_{\ell \mathrm{j}'}$: the lepton + the light jet reconstructed mass;
- $m_{\ell \mathrm{b}}$: the lepton + the b jet reconstructed mass;
- $\not{E}_{\mathrm{T}}$: the amount of the missing energy in each event in the transverse plane $\eta - \phi$;
- CMVAv2 extra jet: is the value of the CMVAv2 b-tagging algorithm for the extra jet;
- $\cos\theta^*_{hel}$: the cosine in the top rest frame of the angle between the lepton 3-momenta in the W boson rest frame and the W boson 3-momenta;
- $\cos\theta^*_{pol}$: the cosine of the angle between the lepton and W boson in the top rest frame;
- $|\Delta\eta_{b-b}|$: is the absolute value of the difference between the pseudorapidity of the two b jets in the 3-jets–2-tags.

5.2 QCD

A QCD enriched control region is defined by reverting the isolation requirements on the lepton in order to extract the contribution of this type of process, difficult to accurately reproduce in simulation, from data. All non QCD processes are subtracted from the data according to their contribution obtained by simulation, therefore obtaining a data-based QCD template for each distribution sought for. The templates obtained in this way are then normalized to the number of events in the isolated region obtained by MC in a first step. The method is validated by verifying on the simulation that there is no significant bias in using the template from the control region. This way to proceed is called data driven estimation of QCD.

For the muon channel it is sufficient follow the above procedure for the subtraction. Instead for the electron channel, a scale factor needs to be applied. This scale factor is necessary because the phase space region in which the subtraction is performed is far away from the region where the electron selection is tuned, therefore no appropriate corrections to the simulation are present and the amount of events in the QCD control region is not reliably predicted by MC. This scale factor is obtained by looking at the tail of the $m_{\mathrm{T}}^{\mathrm{W}}$ variable in the anti-isolation region, after performing a cut on $m_{\mathrm{T}}^{\mathrm{W}} > 200$ GeV/c^2 to completely remove the QCD contribution. For the normalisation a fit in the $m_{\mathrm{T}}^{\mathrm{W}}$ variable is performed both for muon and electron channels and the samples are normalised at the numbers of events given by the fit.

In the 2-jets–1-tag and in the 3-jets–1-tag to discriminate between QCD and other channels the variable used is the transverse mass of the W boson. Figure 5.1 allows to appreciate the discriminating power of the $m_{\mathrm{T}}^{\mathrm{W}}$ variable against QCD events.

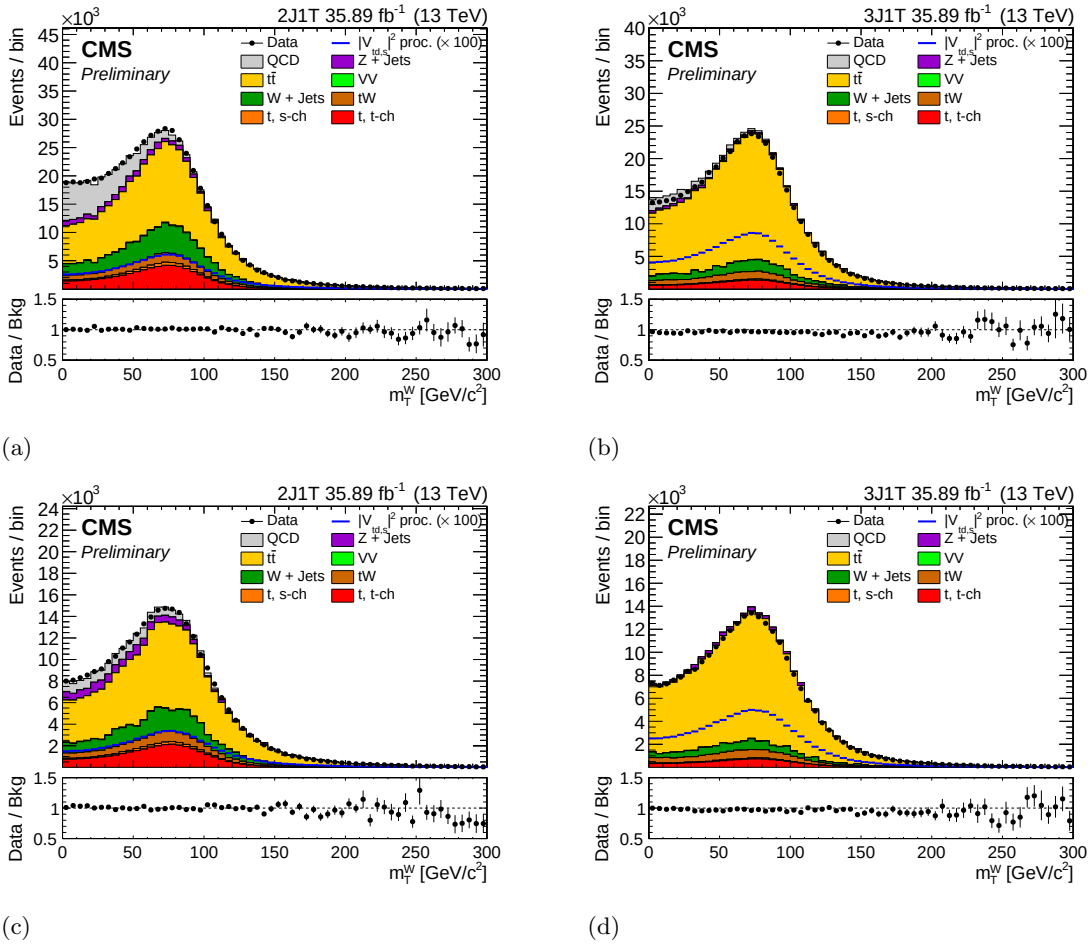

Figure 5.1: Discriminating power against QCD events of the transverse mass of the W boson in the 2-jets–1-tag and in the 3-jets–1-tag: (a) and (b) are for the muon channel while (c) and (d) are for the electron channel.

The region obtained after performing a cut on $m_{\mathrm{T}}^{\mathrm{W}} > 50$ GeV/c^2 is henceforth referred to as **QCD-depleted region**. Then the QCD-depleted region is divided into two subregions with a $|\eta_{j'}|$ cut: a QCD-depleted-central region with a $|\eta_{j'}| < 2.4$ requirement and a QCD-depleted-forward region with $|\eta_{j'}| > 2.4$ requirement.

5.3 Multivariate analysis

Since the signal yield is much smaller compared to the background yields, it is necessary to best exploit all kinematic variables described in Sec. 5.1 and the respective correlations to discriminate between the different signals amongst themselves and against other processes. For this reason, a multivariate analysis, MVA for short, is performed, by training some Boost Decision Trees (BDTs) using the TMVA tool of ROOT. In BDTs, the selection is done on a majority vote on the result of several decision trees, which are all derived from the same training sample by supplying different event weights during the training. Successive decision nodes are used to categorize the events out of the sample as either signal or background. Each node uses only a single discriminating variable to decide if the event is signal-like ("goes right") or background-like ("goes left"). This forms a tree like structure with "baskets" at the end (leave nodes), and an event is classified as either signal or background according to whether the basket where it ends up has been classified signal or background during the training. Training of a decision tree is the process to define the *cut criteria* for each node. The training starts with the root node. Here one takes the full training event sample and selects the variable and corresponding cut value that gives the best separation between signal and background at this stage. Using this cut criterion, the sample is then divided into two subsamples, a signal-like (right) and a background-like (left) sample. Two new nodes are then created for each of the two sub-samples and they are constructed using the same mechanism as described for the root node. The division is stopped once a certain node has reached either a minimum number of events, or a minimum or maximum signal purity. These leave nodes are then called signal or background if they contain more signal respective background events from the training sample. The idea behind the boosting is, that signal events from the training sample, that end up in a background node (and vice versa) are given a larger weight than events that are in the correct leave node. This results in a re-weighed training event sample, with which then a new decision tree can be developed. The boosting can be applied several times (typically 100-500 times) and one ends up with a set of decision trees (a forest). More information about the specific algorithm implemented in this tool can be found in [60].

5.4 Variables in 2-jets–1-tag

5.4.1 QCD-depleted-central region

In the 2-jets–1-tag to discriminate between the single top t-channel with b quarks both in production and in decay, $ST^{\mathrm{2J1T}}_{\mathrm{(b,b)}}$ for short, and the single top t-channel with only one b quark in production or in decay, $ST^{\mathrm{2J1T}}_{\mathrm{(b,q)}}$for short, variables of interest are chosen that involve the correct or wrong top quark assignment, depending on the origin of the b jet that was selected in the 2-jets–1-tag. Additional jets are selected within the range $20 < p_{\mathrm{T}} < 40$ GeV/c and having $|\eta_{j'}| < 2.4$. The leading extra jet is used to reconstruct a top quark candidate. In case it is an event of the $ST^{\mathrm{2J1T}}_{\mathrm{(b,q)}}$ type, the b jet of the 2-jets–1-tag will be stemming from gluon splitting, and the additional jet will have a high chance of being the one stemming from top quark decay to s/d quarks. Variables of interest in this sense are, for example, the mass between the lepton and either jet (the b jet or the leading extra jet), the top quark kinematic distributions built using the combination of the leading extra jet, $\not\!\!E_{\mathrm{T}}$ and the lepton. Figure 5.2 shows some of the most discriminating variables for the muon and electron channels in the region with $m^{\mathrm{W}}_{\mathrm{T}} > 50$ and $|\eta_{j'}| < 2.4$.

In the QCD-depleted-central region the two main backgrounds, $\mathrm{t\bar{t}}$ and $\mathrm{W}+\mathrm{jets}$, have different topologies, and so two different MVA studies are performed against these samples. Table 5.2 reports the results of the MVA in which single top quark t-channel in considered as signal and $\mathrm{t\bar{t}}$ is considered as background, both for the muon channel and the electron channel. The variables used, the relative importance of each of them, and the correlation of each of them to the MVA discriminator are the most interesting parameters of the training and are reported in all the following tables.

Table 5.3 shows the results of the second MVA in the QCD-depleted-central region in which single top quark t-channel is considered as signal and $\mathrm{W}+\mathrm{jets}$ is considered as background, both for the muon channel and the electron channel.

Figure 5.3 shows the distribution of the two discriminators in the QCD-depleted-central region: good agreement between data and MC.

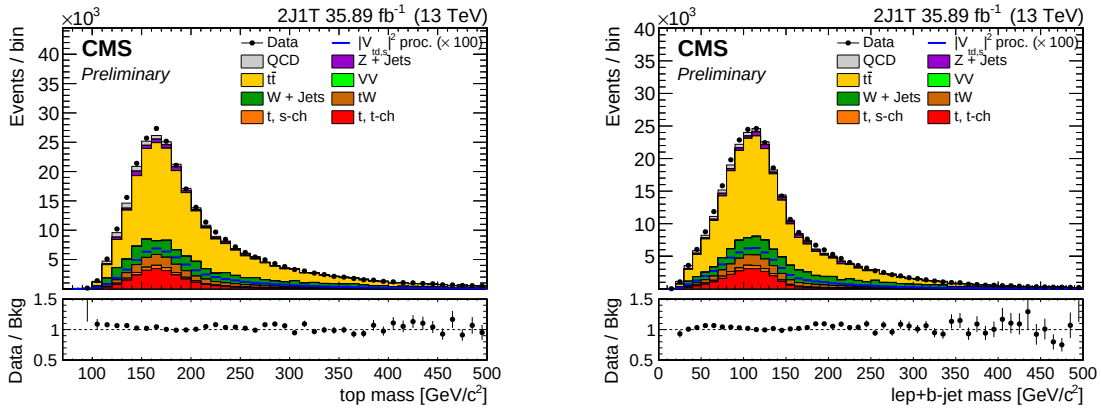

(a)

(b)

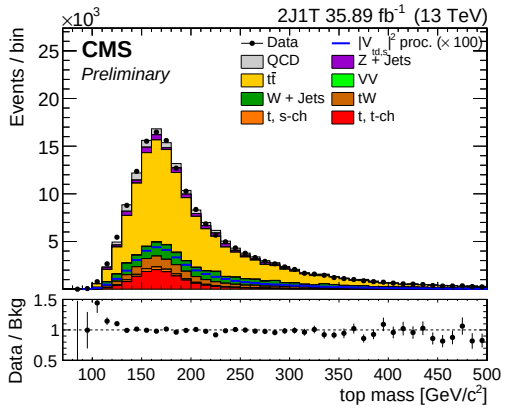

(c)

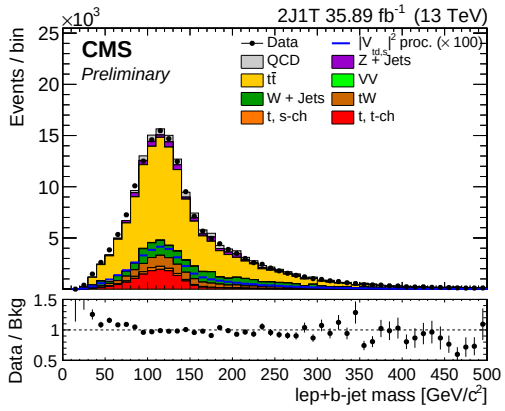

(d)

Figure 5.2: Variables for discrimination in the 2-jets–1-tag region with $m_{\mathrm{T}}^{\mathrm{W}} > 50$ GeV/c^2 and $|\eta_{j'}| < 2.4$: (a) and (b) are for the muon channel while (c) and (d) are for the electron channel.

Table 5.2: Input variables for the BDTs trained for the single top quark t-channel versus $t\bar{t}$, ranked according to their importance in the muon channel, in the 2-jets–1-tag QCD-depleted-central region.

Rank	Variable	Muon			Electron		
		Rel. imp. [%]	Corr. to BDT		Rel. imp. [%]	Corr. to BDT	
			Sig.	Back.		Sig.	Back.
1	W boson transverse mass	16.4	-0.06	-0.25	16.1	-0.08	-0.27
2	no. extra jets	9.2	-0.66	-0.58	6.0	-0.65	-0.55
3	lepton + b jet mass	9.0	-0.20	-0.25	8.1	-0.21	-0.23
4	lepton + light jet mass	8.5	+0.37	+0.08	7.6	+0.38	+0.13
5	$\lvert\eta\rvert$ light jet	8.3	+0.51	+0.41	9.6	+0.56	+0.41
6	top quark mass	8.2	-0.27	-0.24	7.4	-0.29	-0.23
7	$\not\!\!E_{\mathrm{T}}$	7.2	-0.13	-0.24	7.7	-0.13	-0.28
8	CMVA extra jet	6.5	-0.58	-0.46	9.1	-0.58	-0.43
9	$\cos\theta^*_{pol}$	6.1	+0.02	+0.07	6.7	+0.12	+0.13
10	$\cos\theta^*_{hel}$ extra	4.8	-0.59	-0.45	3.8	-0.59	-0.42
11	$\cos\theta^*_{hel}$	4.8	-0.15	+0.07	6.1	+0.12	+0.05
12	top quark mass extra	4.1	-0.55	-0.40	3.4	-0.58	-0.38
13	lepton + extra jet mass	3.7	-0.49	-0.36	3.5	-0.53	-0.35
14	$\cos\theta^*_{pol}$ extra	3.1	-0.59	-0.46	5.0	-0.58	-0.42

Table 5.3: Input variables for the BDTs trained for the single top quark t-channel versus W + jets ranked according to their importance in the muon channel in the 2-jets–1-tag QCD-depleted-central region.

Rank	Variable	Muon			Electron		
		Rel. imp. [%]	Corr. to BDT		Rel. imp. [%]	Corr. to BDT	
			Sig.	Back.		Sig.	Back.
1	lepton + b-jet mass	12.5	-0.38	-0.65	11.9	-0.41	-0.59
2	top quark mass	12.2	-0.37	-0.59	10.3	-0.33	-0.49
3	lepton + light jet mass	9.8	+0.39	-0.03	9.7	+0.48	-0.00
4	$\lvert\eta\rvert$ light jet	7.7	+0.47	+0.29	9.6	+0.57	+0.36
5	$\cos\theta^*_{hel}$	7.6	+0.02	-0.06	7.3	-0.17	-0.26
6	CMVA extra jet	7.3	-0.08	-0.05	7.0	-0.02	+0.03
7	$\cos\theta^*_{pol}$	7.2	-0.09	-0.10	7.3	+0.07	+0.16
8	$\not\!\!E_{\mathrm{T}}$	7.1	+0.16	+0.01	7.0	+0.11	+0.00
9	W-boson transverse mass	6.6	+0.09	-0.10	6.0	-0.01	-0.11
10	lepton + extra jet mass	5.0	-0.14	-0.18	5.5	-0.08	-0.11
11	top quark mass extra	4.8	-0.13	-0.14	5.6	-0.06	-0.05
12	$\cos\theta^*_{pol}$ extra	4.7	-0.13	-0.09	4.8	-0.06	+0.01
13	$\cos\theta^*_{hel}$ extra	4.6	-0.14	-0.06	4.2	-0.07	-0.00
14	no. extra jets	3.0	-0.12	-0.04	3.7	-0.06	+0.03

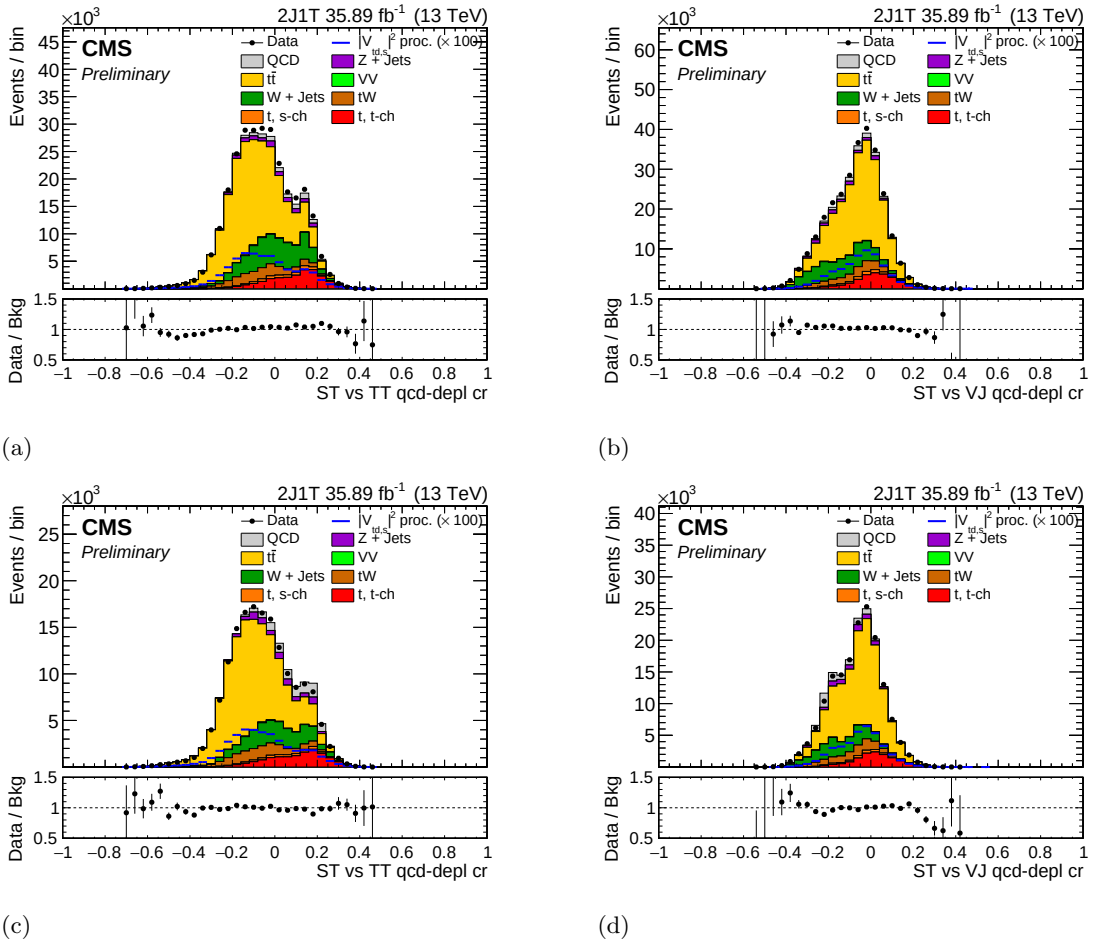

Figure 5.3: Distribution of the two discriminators in the 2-jets–1-tag QCD-depleted-central region: the ones on the left represents the single top quark t-channel versus the $t\bar{t}$, (a) is for the muon channel and (c) is for the electron channel, and the ones on the right represents the single top quark t-channel versus the $W + jets$, (b) is for the muon channel and (d) is for the electron channel.

5.4.2 QCD-depleted-forward region

Selecting events with a high value of the η of the non-b-tagged jet, makes the discrimination between top quarks to be more powerful as a cut on $|\eta_{j'}| > 2.4$ as favours events where the $|\eta_{j'}|$ is stemming actually from the light quark recoiling against the top quark. This is why this forward region is also referred to as **signal-enriched region**. Figure 5.4 shows the discriminating variables in the region with $m_{\mathrm{T}}^{\mathrm{W}} > 50$ and $|\eta_{j'}| > 2.4$ for muons and electrons.

Other MVA analyses are performed in this region in order to increase the separation between $ST^{\mathrm{2J1T}}_{\mathrm{(b,b)}}$ and $ST^{\mathrm{2J1T}}_{\mathrm{(b,q)}}$ but this time the signals are single top quark t-channel decaying to, or produced via s/d quarks and $\mathrm{t\bar{t}}$ one of them decaying to s/d quarks and the backgrounds are single top quark produced via and decaying to b quarks for the first one and $\mathrm{t\bar{t}}$ both decaying to b quarks plus $\mathrm{W}+\mathrm{jets}$ for the second one.

Table 5.4 shows the results of the MVA in which single top quark t-channel decaying to, or produced via s/d quarks and $\mathrm{t\bar{t}}$ one of them decaying to s/d quarks are considered as signal and single top quark t-channel decaying to b quarks is considered as background.

Table 5.5 shows the results of the MVA in which single top quark t-channel decaying to, or produced via s/d quarks and $\mathrm{t\bar{t}}$ one of them decaying to s/d quarks are considered as signal and $\mathrm{t\bar{t}}$ both decaying to b quarks and $\mathrm{W}+\mathrm{jets}$ are considered as background.

Figure 5.5 shows the distributions of the discriminators in the signal-enriched region: good agreement between data and MC.

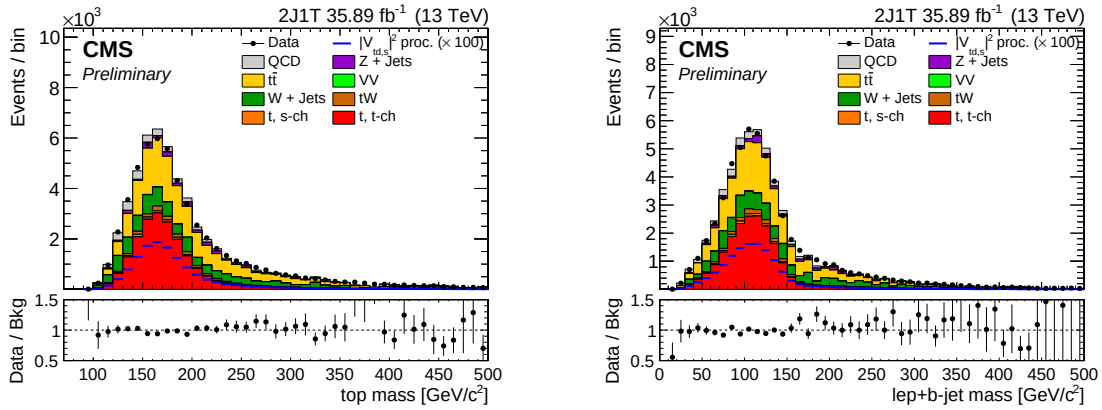

(a) (b)

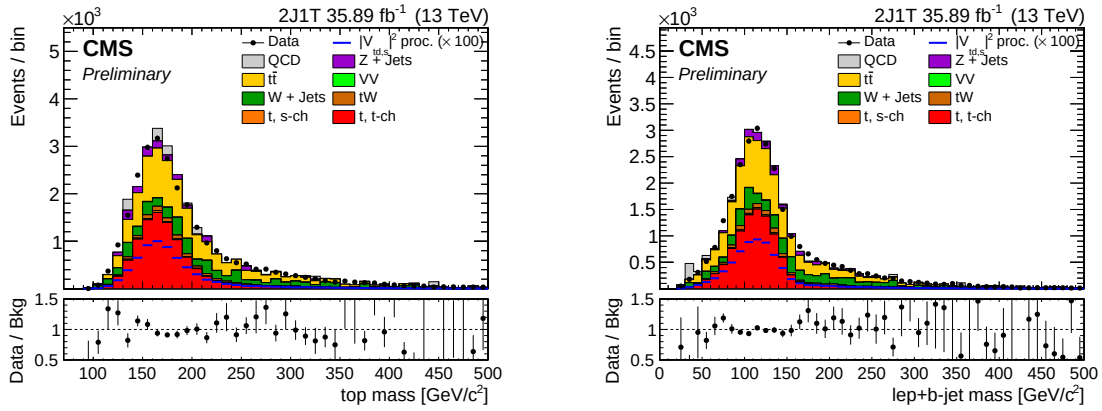

(c) (d)

Figure 5.4: Variables for $ST^{\mathrm{2J1T}}_{\mathrm{(b,q)}} - ST^{\mathrm{2J1T}}_{\mathrm{(b,b)}}$ discrimination in the 2-jets–1-tag region with $m^{\mathrm{W}}_{\mathrm{T}} > 50$ GeV/c^2 and $|\eta_{j'}| > 2.4$: (a) and (b) are for the muon channel while (c) and (d) are for the electron channel.

Table 5.4: Input variables for the BDTs trained for the single top quark t-channel decaying to, or produced via s/d quarks and $t\bar{t}$ one of them decaying to s/d quarks versus single top quark t-channel produced via and decaying to b quarks ranked according to their importance in the muon channel in the 2-jets–1-tag QCD-depleted-forward region.

Rank	Variable	Muon			Electron		
		Rel. imp. [%]	Corr. to BDT		Rel. imp. [%]	Corr. to BDT	
			Sig.	Back.		Sig.	Back.
1	W-boson transverse mass	23.5	+0.25	+0.10	24.3	+0.29	+0.11
2	no. extra jets	9.7	+0.64	+0.58	8.5	+0.60	+0.55
3	CMVA extra jet	9.5	+0.40	+0.35	7.4	+0.35	+0.30
4	lepton + b-jet mass	8.3	+0.18	+0.07	7.3	+0.11	-0.00
5	$\not{E}_{\mathrm{T}}$	7.4	+0.21	+0.10	7.6	+0.21	+0.07
6	top quark mass	6.5	+0.22	+0.16	6.1	+0.14	+0.07
7	$\lvert\eta\rvert$ light jet	5.6	-0.45	-0.43	5.6	-0.43	-0.43
8	$\cos\theta^*_{pol}$	5.6	-0.10	-0.10	7.0	-0.21	-0.22
9	$\cos\theta^*_{hel}$ extra	4.9	+0.50	+0.46	4.3	+0.47	+0.42
10	lepton + light jet mass	4.1	-0.24	-0.25	4.5	-0.25	-0.26
11	$\cos\theta^*_{hel}$	3.9	-0.08	-0.09	5.7	-0.06	-0.09
12	top quark mass extra	3.8	+0.48	+0.42	4.9	+0.45	+0.40
13	$\cos\theta^*_{pol}$ extra	3.8	+0.48	+0.43	3.6	+0.42	+0.38
14	lepton + extra jet mass	3.3	+0.43	+0.37	3.1	+0.43	+0.37

Table 5.5: Input variables for the BDTs trained for the single top quark t-channel decaying to, or produced via s/d quarks and $t\bar{t}$ one of them decaying to s/d quarks are considered as signal and $t\bar{t}$ both decaying to b quarks and W + jets ranked according to their importance in the muon channel in the 2-jets–1-tag QCD-depleted-forward region.

Rank	Variable	Muon			Electron		
		Rel. imp. [%]	Corr. to BDT		Rel. imp. [%]	Corr. to BDT	
			Sig.	Back.		Sig.	Back.
1	$\cos\theta^*_{pol}$	10.3	+0.12	+0.12	9.4	+0.30	+0.34
2	$\lvert\eta\rvert$ light jet	9.6	+0.51	+0.13	8.5	+0.56	+0.20
3	lepton + b-jet mass	9.2	-0.37	-0.38	9.7	-0.35	-0.33
4	top quark mass	8.7	-0.38	-0.34	9.3	-0.37	-0.31
5	CMVA extra jet	8.1	-0.39	-0.18	6.6	-0.43	-0.22
6	W-boson transverse mass	7.6	+0.02	+0.03	7.3	-0.05	+0.01
7	lepton + light jet mass	7.5	+0.28	+0.06	6.1	+0.37	+0.04
8	$\not{E}_{\mathrm{T}}$	6.5	+0.05	+0.11	6.6	-0.04	+0.06
9	$\cos\theta^*_{hel}$	6.5	-0.01	-0.09	6.9	+0.02	-0.05
10	no. extra jets	6.3	-0.37	-0.10	5.2	-0.42	-0.15
11	top quark mass extra	6.1	-0.33	-0.09	5.9	-0.39	-0.13
12	$\cos\theta^*_{pol}$ extra	4.9	-0.34	-0.07	6.8	-0.38	-0.06
13	$\cos\theta^*_{hel}$ extra	4.5	-0.37	-0.11	5.5	-0.41	-0.12
14	lepton + extra jet mass	4.3	-0.31	-0.11	6.1	-0.36	-0.13

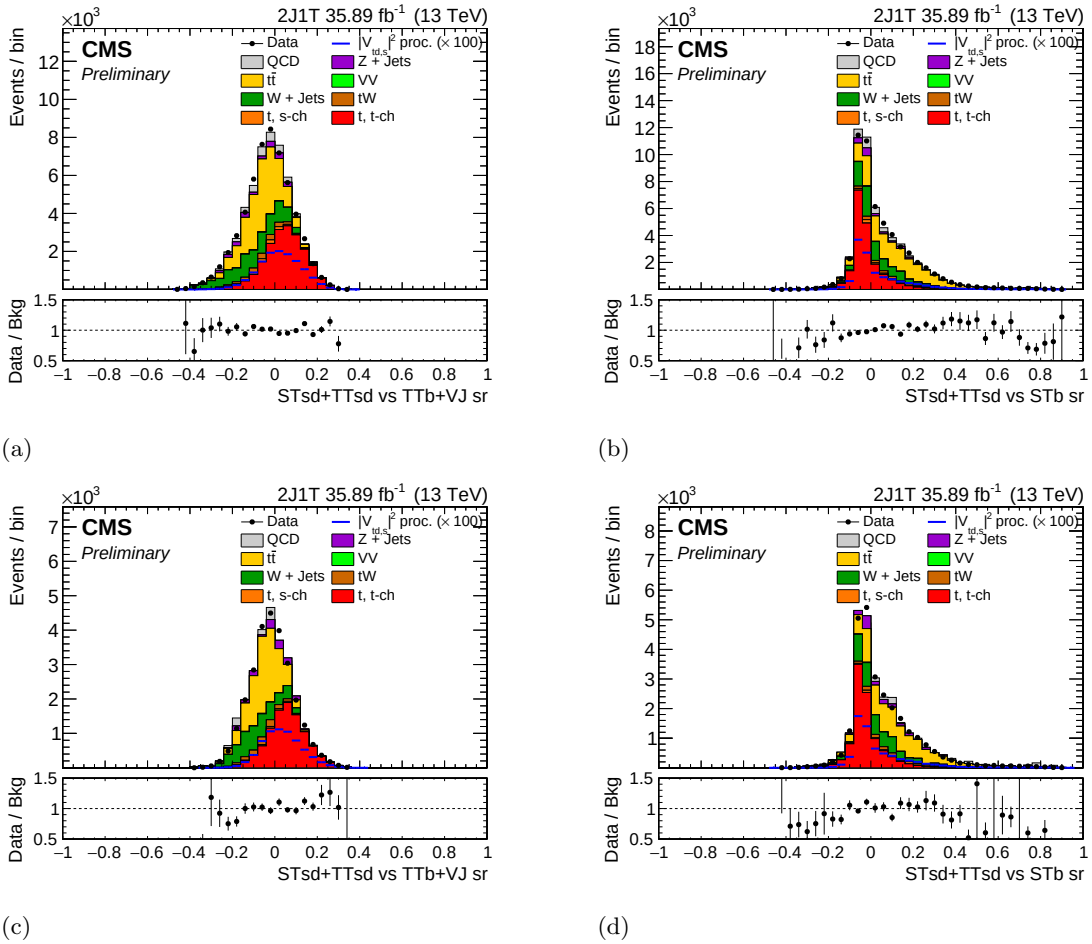

(a) (b)

(c) (d)

Figure 5.5: Distribution of the two discriminators in the 2-jets–1-tag QCD-depleted-forward region: the ones on the left represents the single top quark t-channel decaying to, or produced via s/d quarks and $t\bar{t}$ one of them decaying to s/d quarks versus the $t\bar{t}$ both of them decaying to b quarks and W + jets, (a) is for the muon channel and (c) is for the electron channel, and the ones on the right represents the single top quark t-channel decaying to, or produced via s/d quarks versus the single top quark t-channel produced via and decaying to b quarks, (b) is for the muon channel while (d) is for the electron channel.

5.5 Variables in 3-jets–1-tag

5.5.1 QCD-depleted-central region

The 3-jets–1-tag case is very similar to the 2-jets–1-tag one. After the $m_{\mathrm{T}}^{\mathrm{W}} > 50$ GeV/c^2 cut the most discriminating variables are, for example, the CMVA value for the extra jet or the transverse mass of the W boson. Figure 5.6 shows the discriminating variables in the QCD-depleted-central region.

Like as the 2-jets–1-tag, also in the 3-jets–1-tag two MVA studies are performed considering single top quark t-channel as signal and $\mathrm{t\bar{t}}$ and $\mathrm{W}+\mathrm{jets}$ as background, in the QCD-depleted-central region. Table 5.6 shows the results of the MVA study in which single top quark t-channel is considered as signal and $\mathrm{t\bar{t}}$ is considered as background.

Table 5.7 shows the results of the MVA study in which single top quark t-channel is considered as signal and $\mathrm{W}+\mathrm{jets}$ is considered as background.

Figure 5.7 shows the distribution of the two discriminators in the QCD-depleted-central region: good agreement between data and MC.

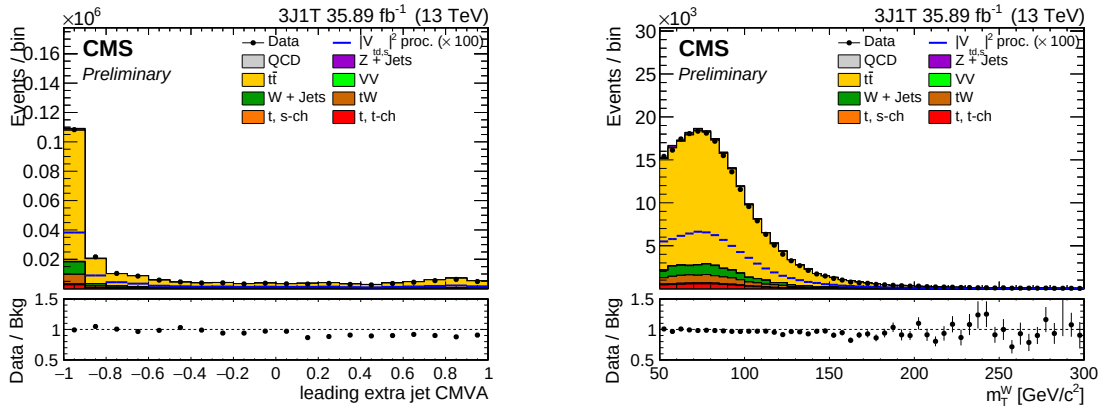

(a)

(b)

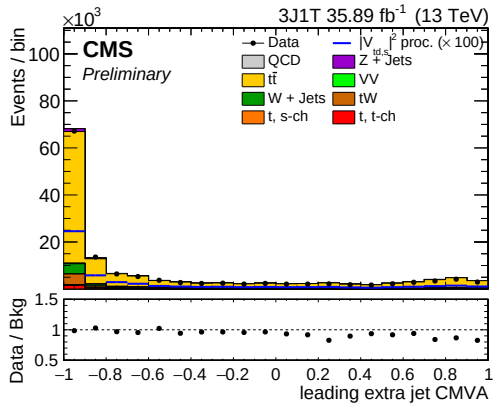

(c)

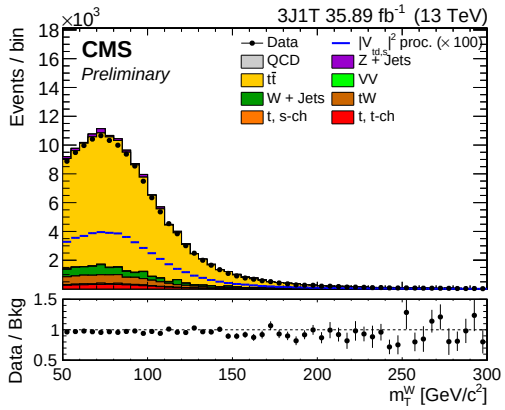

(d)

Figure 5.6: Variables for $ST^{\mathrm{3J1T}}_{\mathrm{(b,q)}} - ST^{\mathrm{3J1T}}_{\mathrm{(b,b)}}$ discrimination in the 3-jets–1-tag region with $m_{\mathrm{T}}^{\mathrm{W}} > 50$ and $|\eta_{j'}| < 2.4$: (a) and (b) are for the muon channel while (c) and (d) are for the electron channel.

Table 5.6: Input variables for the BDTs trained for the single top quark t-channel versus $t\bar{t}$ ranked according to their importance in the muon channel in the 3-jets–1-tag QCD-depleted-central region.

Rank	Variable	Muon			Electron		
		Rel. imp. [%]	Corr. to BDT		Rel. imp. [%]	Corr. to BDT	
			Sig.	Back.		Sig.	Back.
1	W-boson transverse mass	11.4	-0.07	-0.10	10.8	-0.02	-0.44
2	$\|\eta\|$ light jet	9.4	+0.54	+0.61	8.9	+0.57	+0.33
3	no. extra jets	8.5	-0.52	-0.42	9.1	-0.50	-0.19
4	lepton + light jet mass	8.2	+0.34	+0.23	7.4	+0.36	+0.02
5	$\cos\theta^*_{pol}$	8.1	-0.01	+0.01	8.3	+0.09	-0.12
6	top quark mass extra	7.3	+0.15	+0.05	6.8	+0.08	-0.02
7	$\cos\theta^*_{pol}$ extra	7.2	+0.23	+0.05	7.0	+0.29	+0.20
8	lepton + extra jet mass	6.9	+0.14	-0.00	6.2	+0.11	-0.13
9	lepton + b-jet mass	6.7	-0.07	-0.14	6.9	-0.07	+0.01
10	top quark mass	6.1	-0.11	-0.13	6.1	-0.11	-0.03
11	$\not{E}_{\mathrm{T}}$	5.4	-0.07	-0.11	5.8	-0.09	-0.39
12	CMVA extra jet	5.3	+0.20	+0.09	6.3	+0.22	+0.16
13	$\cos\theta^*_{hel}$ extra	4.9	+0.19	+0.14	5.4	+0.20	-0.09
14	$\cos\theta^*_{hel}$	4.5	+0.11	+0.11	4.9	+0.10	+0.26

Table 5.7: Input variables for the BDTs trained for the single top quark t-channel versus W + jets ranked according to their importance in the muon channel in the 3-jets–1-tag QCD-depleted-central region.

Rank	Variable	Muon			Electron		
		Rel. imp. [%]	Corr. to BDT		Rel. imp. [%]	Corr. to BDT	
			Sig.	Back.		Sig.	Back.
1	CMVA extra jet	9.5	+0.56	+0.22	8.9	+0.58	+0.29
2	lepton + b-jet mass	9.2	-0.33	-0.65	9.1	-0.21	-0.54
3	$\|\eta\|$ light jet	8.5	+0.32	+0.28	8.3	+0.40	+0.35
4	top quark mass	8.3	-0.30	-0.59	7.4	-0.22	-0.45
5	lepton + extra jet mass	7.5	+0.10	-0.23	5.5	+0.05	-0.22
6	$\cos\theta^*_{pol}$	7.3	-0.09	+0.03	7.9	-0.04	+0.08
7	$\not{E}_{\mathrm{T}}$	7.1	+0.09	-0.03	6.8	+0.00	-0.03
8	lepton + light jet mass	7.1	+0.24	-0.11	7.8	+0.38	+0.01
9	$\cos\theta^*_{pol}$ extra	6.8	-0.05	-0.04	6.7	+0.00	+0.04
10	top quark mass extra	6.4	+0.11	-0.16	6.1	+0.03	-0.15
11	$\cos\theta^*_{hel}$	6.0	+0.02	-0.08	7.7	+0.02	-0.19
12	$\cos\theta^*_{hel}$ extra	5.8	+0.14	+0.11	7.4	+0.16	+0.05
13	W-boson transverse mass	5.6	+0.10	-0.12	5.2	+0.11	-0.11
14	no. extra jets	4.9	-0.12	+0.04	5.2	-0.13	+0.01

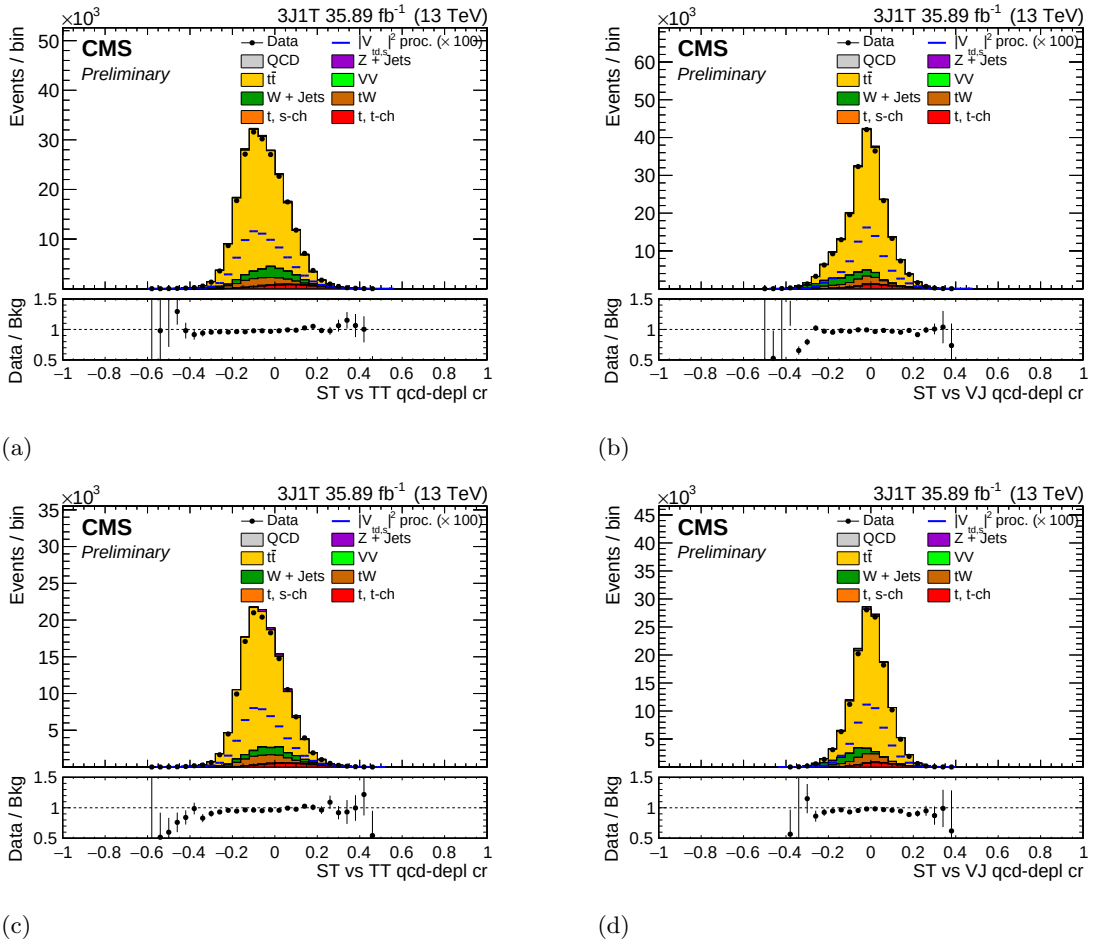

(a) (b)

(c) (d)

Figure 5.7: Distribution of the two discriminators in the 3-jets–1-tag QCD-depleted-central region: the ones on the left represents the single top quark t-channel versus the $\mathrm{t\bar{t}}$, (a) is for the muon channel and (c) is for the electron channel, and the ones on the right represents the single top quark t-channel versus the $\mathrm{W}+\mathrm{jets}$, (b) is for the muon channel and (d) is for the electron channel.

5.5.2 QCD-depleted-forward region

After this step, it is applied a selection on the value of the $|\eta_{j'}|$ of the non-b-tagged jet in order to be more sensible to $ST^{3J1T}_{(b,q)}$ events. Figure 5.8 shows the discriminating variables in the region with $m_T^W > 50$ GeV/c^2 and $|\eta_{j'}| > 2.4$.

Table 5.8 shows the results of the MVA in which single top quark t-channel decaying to, or produced via s/d quarks and $t\bar{t}$ one of them decaying to s/d quarks are considered as signal and single top quark t-channel produced via and decaying to b quarks is considered as background in the 3-jets–1-tag QCD-depleted-forward region.

Table 5.9 shows the results of the MVA in which single top quark t-channel decaying to, or produced via s/d quark and $t\bar{t}$ one of them decaying to s/d quarks are considered as signal and $t\bar{t}$ both of them decaying to b quarks and W + jets are considered as background.

Figure 5.9 shows the distribution of the discriminator in the signal-enriched region: good agreement between data and MC.

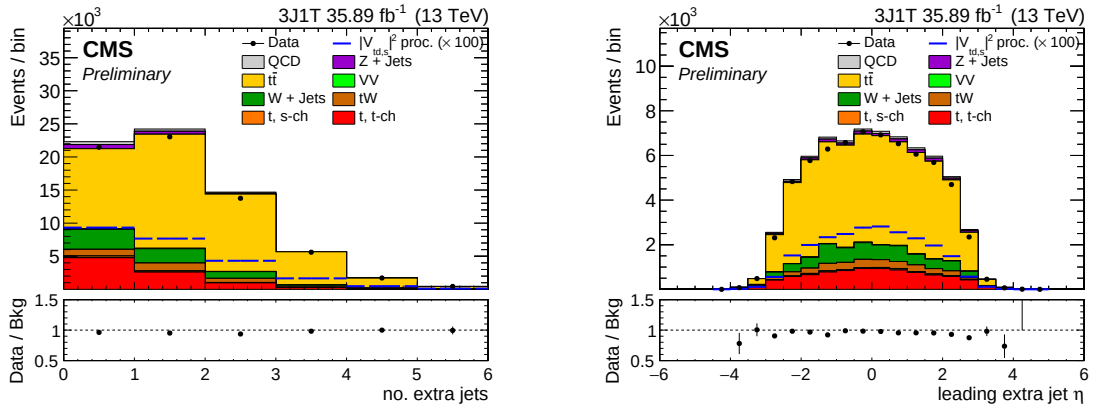

(a) (b)

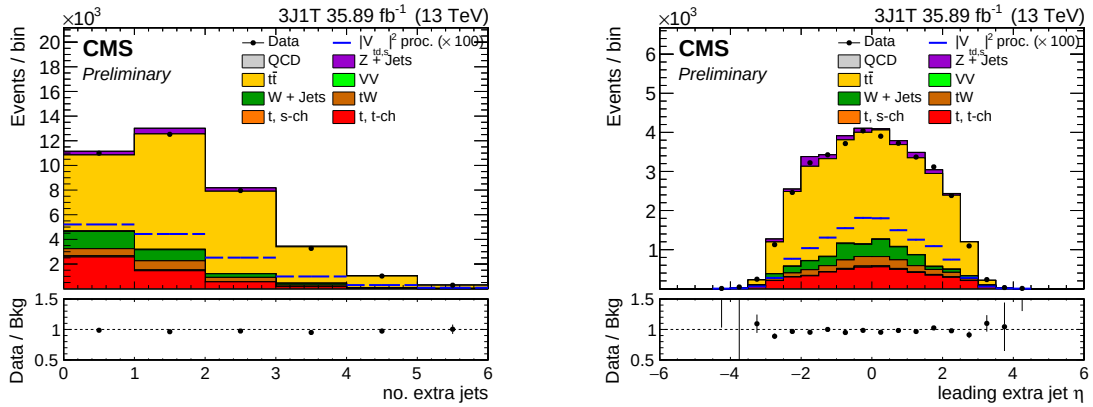

(c) (d)

Figure 5.8: Variables for $ST^{\mathrm{3J1T}}_{\mathrm{(b,q)}} - ST^{\mathrm{3J1T}}_{\mathrm{(b,b)}}$ discrimination in the 3-jets–1-tag region with $m^{\mathrm{W}}_{\mathrm{T}} > 50$ GeV/c^2 and $|\eta_{j'}| > 2.4$: (a) and (b) are for the muon channel while (c) and (d) are for the electron channel.

Table 5.8: Input variables for the BDTs trained for the single top quark t-channel decaying to, or produced via s/d quarks and $t\bar{t}$ decaying to s/d quarks versus single top quark t-channel produced via and decaying to b quarks, ranked according to their importance in the muon channel in the 3-jets–1-tag QCD-depleted-forward region.

Rank	Variable	Muon			Electron		
		Rel. imp. [%]	Corr. to BDT		Rel. imp. [%]	Corr. to BDT	
			Sig.	Back.		Sig.	Back.
1	$\|\eta\|$ extra jet	12.6	+0.00	+0.00	10.9	-0.02	-0.01
2	no. extra jets	8.4	+0.60	+0.50	8.6	+0.58	+0.50
3	top quark transverse mass	8.3	+0.30	+0.24	9.7	+0.29	0.25
4	top quark mass	7.9	+0.26	+0.21	6.8	+0.25	+0.22
5	$\cos\theta^*_{pol}$ extra	7.7	-0.27	-0.34	9.2	-0.30	-0.37
6	$\|\eta\|$ b-jet	6.6	-0.01	-0.01	6.9	-0.02	-0.02
7	top quark transverse mass extra	6.6	-0.12	-0.29	6.7	-0.12	-0.25
8	top quark mass extra	5.9	-0.17	-0.33	5.9	-0.17	-0.30
9	lepton + extra jet mass	5.7	-0.17	-0.33	5.4	-0.18	-0.32
10	b-jet p_t	5.6	-0.01	+0.01	5.3	-0.00	+0.03
11	$\cos\theta^*_{pol}$	5.2	-0.09	-0.02	6.0	-0.18	-0.09
12	lepton + b-jet mass	5.0	+0.22	+0.17	6.2	+0.23	+0.20
13	CMVA extra jet	5.0	-0.15	-0.05	5.2	-0.18	-0.08
14	$\cos\theta^*_{hel}$ extra	4.8	-0.21	-0.24	3.7	-0.18	-0.22
15	$\cos\theta^*_{hel}$	4.1	-0.10	-0.06	3.6	-0.02	-0.00

Table 5.9: Input variables for the BDTs trained for the single top quark t-channel decaying to, or produced via s/d quarks and $t\bar{t}$ one of them decaying to s/d quarks versus $t\bar{t}$ both of them decaying to b quarks and $W+$jets, in the 3-jets–1-tag QCD-depleted-forward region, ranked according to their importance in the muon channel.

Rank	Variable	Muon			Electron		
		Rel. imp. [%]	Corr. to BDT		Rel. imp. [%]	Corr. to BDT	
			Sig.	Back.		Sig.	Back.
1	no. extra jets	10.3	-0.34	-0.20	10.5	-0.40	-0.28
2	CMVA extra jet	9.2	+0.41	+0.31	8.7	+0.36	+0.25
3	top quark mass extra	8.9	-0.15	-0.19	8.0	-0.18	-0.23
4	$\|\eta\|$ light jet	8.4	+0.40	+0.17	7.3	+0.37	+0.14
5	top quark mass	7.9	-0.19	-0.29	7.4	-0.11	-0.15
6	$\cos\theta^*_{pol}$	7.4	+0.08	+0.09	6.8	+0.08	+0.04
7	lepton + b-jet mass	7.3	-0.18	-0.31	7.8	-0.09	-0.15
8	lepton + extra jet mass	6.3	-0.16	-0.22	7.2	-0.18	-0.24
9	$\not{E}_{\mathrm{T}}$	6.2	-0.04	+0.01	6.5	-0.07	-0.02
10	$\cos\theta^*_{pol}$ extra	6.2	+0.12	+0.09	6.8	+0.17	+0.11
11	lepton + light jet mass	6.0	+0.22	+0.04	7.7	+0.25	+0.07
12	$\cos\theta^*_{hel}$	5.4	+0.06	+0.01	5.2	+0.06	+0.02
13	W-boson transverse mass	5.3	+0.01	+0.03	4.9	+0.00	+0.03
14	$\cos\theta^*_{hel}$ extra	5.1	+0.05	+0.00	5.3	+0.01	-0.03

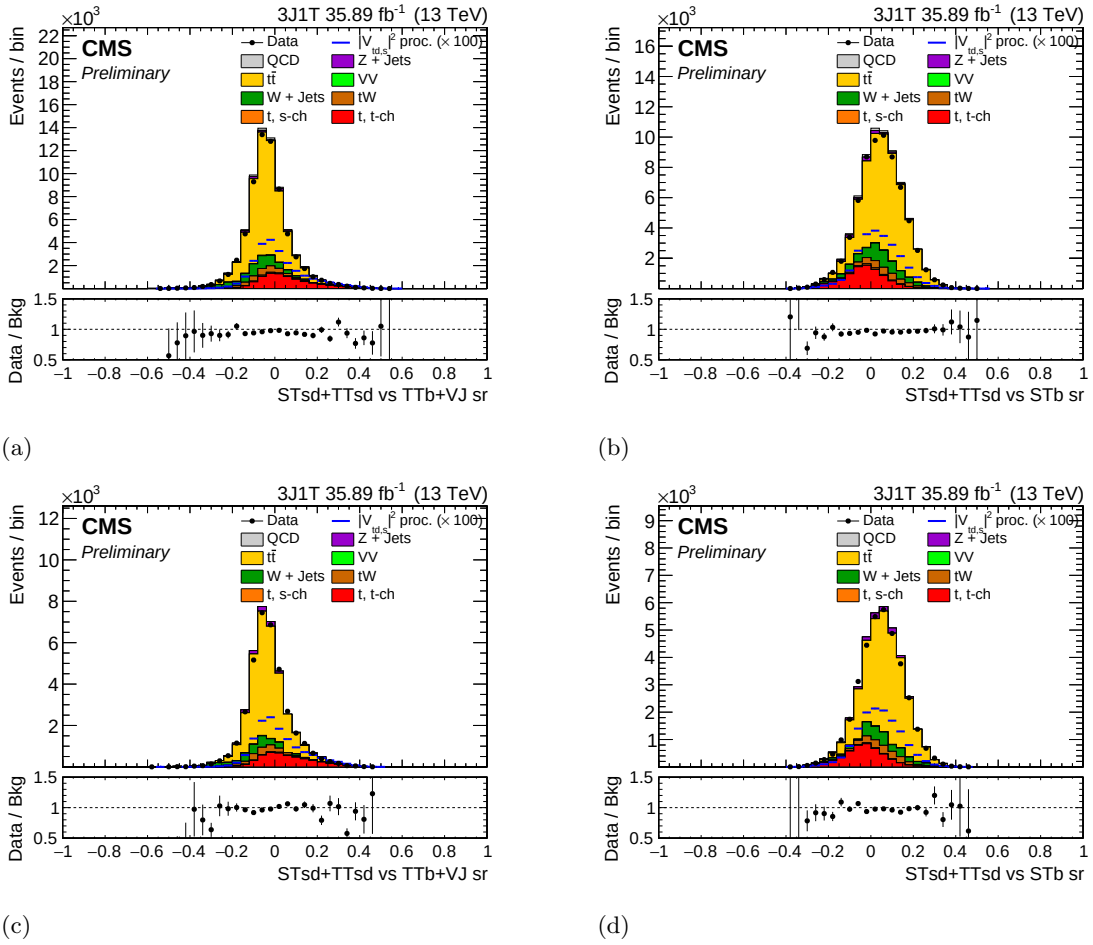

Figure 5.9: Distribution of the two discriminators in the 3-jets–1-tag QCD-depleted-forward region: the ones on the left represents the single top quark t-channel decaying to, or produced via s/d quarks and $t\bar{t}$ one of them decaying to s/d quarks versus the $t\bar{t}$ both of them decaying to b quarks, (a) is for the muon channel and (c) is for the electron channel, and the ones on the right represents the single top quark t-channel decaying to, or produced via s/d quarks versus the single top quark t-channel produced via and decaying to b quarks, (b) is for the muon channel while (d) is for the electron channel.

5.6 Variables in 3-jets–2-tags

In the 3-jets–2-tags there are two b jets one stemming from the top quark decay and one stemming from the gluon splitting. Both b jets are used to reconstruct a top quark candidate and its correlated variables. In this case it is unnecessary to apply the $m_{\mathrm{T}}^{\mathrm{W}} > 50$ GeV/c^2 cut because the contribution of QCD-multijet events is negligible. Also the cuts on $|\eta_{j'}|$ are irrelevant because this case is dominated by $\mathrm{t\bar{t}}$ and single top t-channel with a b quark both in production and decay samples. So only the MVA study of single top quark t-channel versus $\mathrm{t\bar{t}}$ is performed. Figure 5.11 shows the distribution of the discriminator: good agreement between data and MC.

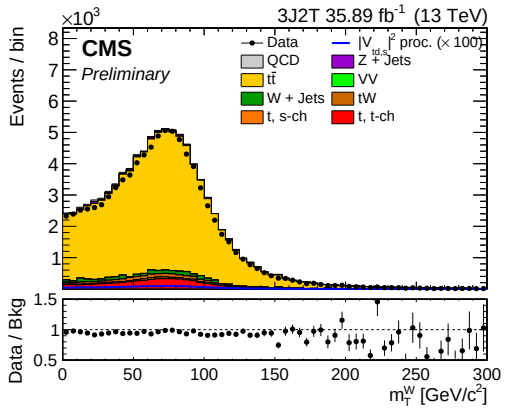

(a)

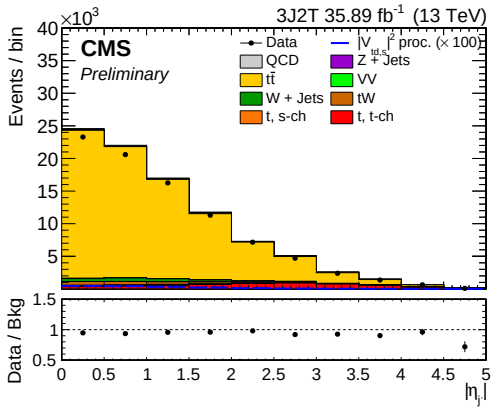

(b)

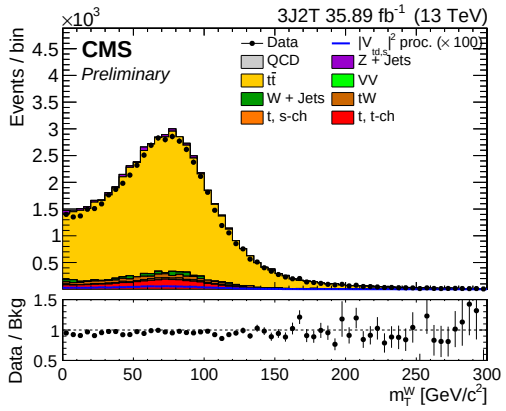

(c)

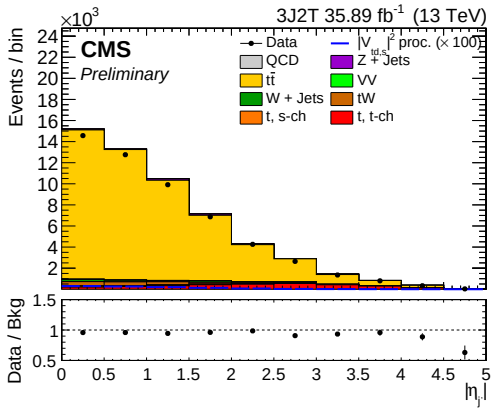

(d)

Figure 5.10: Variables for the single top quark t-channel- $\mathrm{t\bar{t}}$ discrimination in the 3-jets–2-tags region: (a) and (b) are for the muon channel while (c) are and (d) for the electron channel.

Table 5.10 shows the results of the MVA in which single top quark t-channel is considered as signal and $t\bar{t}$ is considered as background.

Table 5.10: Input variables for the BDTs trained for the single top quark t-channel versus $t\bar{t}$ ranked according to their importance in the muon channel.

Rank	Variable	Muon			Electron		
		Rel. imp. [%]	Corr. to BDT		Rel. imp. [%]	Corr. to BDT	
			Sig.	Back.		Sig.	Back.
1	$\|\eta\|$ light jet	12.5	+0.76	+0.65	11.1	+0.76	+0.65
3	lepton + light jet mass	10.4	+0.39	+0.27	9.8	+0.47	+0.32
2	W-boson transverse mass	10.4	-0.05	-0.12	10.4	-0.06	-0.16
4	no. extra jets	9.5	-0.48	-0.42	9.1	-0.48	-0.41
5	$\cos\theta^*_{pol}$ second	7.7	+0.18	+0.12	7.8	+0.24	+0.14
6	$\cos\theta^*_{pol}$ leading	6.9	+0.11	+0.12	7.0	+0.19	+0.14
7	lepton + leading b-jet mass	6.2	+0.01	-0.01	6.9	+0.03	+0.01
8	$\not{E}_{\mathrm{T}}$	5.9	-0.09	-0.07	6.0	-0.09	-0.11
9	lepton + second b-jet mass	5.8	+0.00	-0.01	6.5	-0.00	-0.08
10	top quark mass leading	5.7	-0.04	-0.01	6.9	-0.02	+0.00
11	$\cos\theta^*_{hel}$ leading	5.1	+0.04	-0.03	6.3	+0.10	+0.08
12	$\|\Delta\eta_{b-b}\|$	5.0	-0.00	-0.02	4.3	-0.02	-0.04
13	$\cos\theta^*_{hel}$ second	4.4	+0.17	+0.12	3.6	+0.04	-0.01
14	top quark mass second	4.4	-0.03	-0.05	4.2	-0.04	-0.05

Figure 5.11 shows the distribution of the discriminator: good agreement between data and MC.

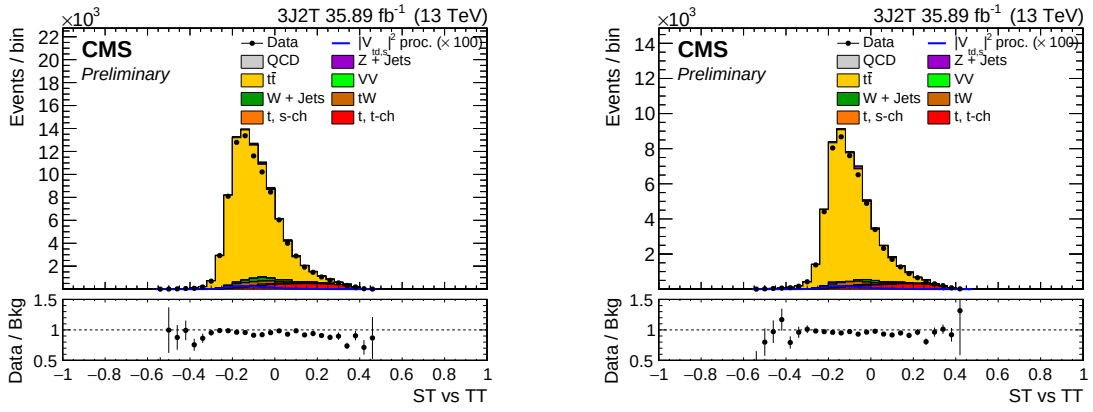

(a) (b)

Figure 5.11: Distribution of the discriminator in the 3-jets–2-tags region: (a) is for the muon channel while (b) is for the electron channel.

5.6.1 2D plots

For the 2-jets–1-tag and the 3-jets–1-tag, the MVA variables obtained from the BDTs trainings in the QCD-depleted-central and -forward regions are combined together in a 2D plot. This 2D distribution takes into account the correlations amongst the two variables, for each region, and it is then used in the fit; the exact fit procedure can be found in Sec. 5.7.

5.7 Fit procedure

The CKM matrix elements are extracted for the measured cross-section of the single top t-channel process. The tool used to perform the statistical inference makes use of RooStats for the calculations. The further details on RooStats can be found at [61]. A cascade fit is performed by dividing the 2-jets–1-tag region and in the 3-jets–1-tag region in three subregions. An additional handle is gained by adding the 3-jets–2-tags region to the fit.

The fit procedure is divided in three steps:

- In the first step the Maximum Likelihood fit is performed for the QCD scale factor extraction for each of the regions defined for the 2-jets–1-tag and for the 3-jets–1-tag regions. QCD events are absent in the 3-jets–2-tags and no fit is performed for this region. The scale factor is than used for the normalisation of QCD template.

- In the second step, the light quark distribution $|\eta_{j'}|$ and $m_{\mathrm{T}}^{\mathrm{W}}$ are used to define two regions, one in order to control the $\mathrm{t\bar{t}}$, $\mathrm{W}+\mathrm{jets}$ together with the t-channel, where $|\eta_{j'}| < 2.4$ and $m_{\mathrm{T}}^{\mathrm{W}} > 50$ GeV/c^2 are required, and one enriched in t-channel $\mathrm{V_{td}}$-$\mathrm{V_{ts}}$ events where $|\eta_{j'}| > 2.4$ and $m_{\mathrm{T}}^{\mathrm{W}} > 50$ GeV/c^2 are required. This selection is performed in both the 2-jets–1-tag and in the 3-jets–1-tag regions. No selection is performed in the 3-jets–2-tags region.

- In the last step, the Maximum Likelihood fit is performed simultaneously in the regions defined in step 2, while the QCD prior uncertainty and central value are taken from step 1. The presence of standard top quark decay products, $|\mathrm{V_{tb}}|$, is now one of the major background to the $|\mathrm{V_{td}}|$ or $|\mathrm{V_{ts}}|$ extraction.

5.7.1 Fit variables

The $m_{\mathrm{T}}^{\mathrm{W}}$ variable is used for a first estimation of the QCD-multijet background and the flat prior fitted is been used as scale factor for the QCD template. In the QCD-

depleted region a MVA analysis is performed in order to obtain two MVA variables in the QCD-depleted-central region and other two MVA variables in the QCD-depleted-forward region.

In particular for the 2-jets–1-tag and 3-jets–1-tag regions four different multivariate discriminators are defined with the use of a boosted decision tree algorithm. The choices of the processes to use as signal or background in the training are the same in both regions for the four discriminants:

- the first is obtained considering the single top t-channel as signal and the $t\bar{t}$ is considered as background in the QCD-depleted-central region;
- the second is obtained considering the single top t-channel as signal and the $W + jets$ is considered as background in the QCD-depleted-central region;
- the third is obtained considering the single top t-channel decaying to, or produced via s/d quarks and $t\bar{t}$ one of them decaying to s/d quarks as signal and the $t\bar{t}$ both of them decaying to b quarks and $W + jets$ are considered as background in the QCD-depleted-forward region;
- the fourth is obtained considering the single top t-channel decaying to, or produced via s/d quarks and $t\bar{t}$ one of them decaying to s/d quarks as signal and the the single top t-channel produced via and decaying to b quarks as background in the QCD-depleted-forward region.

At the end, for the 3-jets–2-tags, the multivariate analysis consists in only one MVA variable obtained considering the single top t-channel as signal and the $t\bar{t}$ is considered as background without any requirement.

The MVA variables trained in the same region are combined together in a 2D histogram in order to consider the correlations amongst them. After this step it is chosen an interesting region in the 2D histogram and this region is unrolled in a 1D histogram in the way that it can be fitted. Figure 5.12 shows an example of the histograms obtained with this procedure.

Figure 5.13 shows an example of the variable obtained by the combination of the two MVA variables in the 2-jets–1-tag for the QCD-depleted-forward region for a better understanding of the different shapes of the 2D histogram unrolled in a 1D histogram.

5.7.2 Maximum Likelihood fit

The Maximum Likelihood, ML, fit is performed simultaneously in the 2-jets–1-tag regions (central, forward), in the 3-jets–1-tag regions (central, forward), and in the 3-

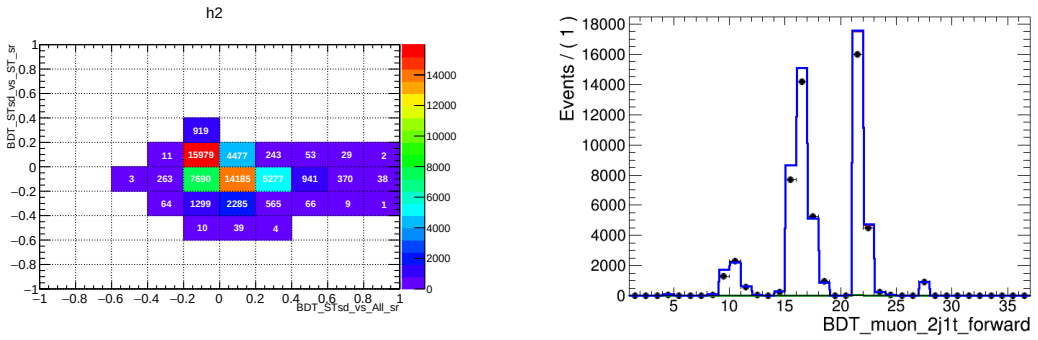

(a) (b)

Figure 5.12: Example of the histogram produced for the fit procedure.

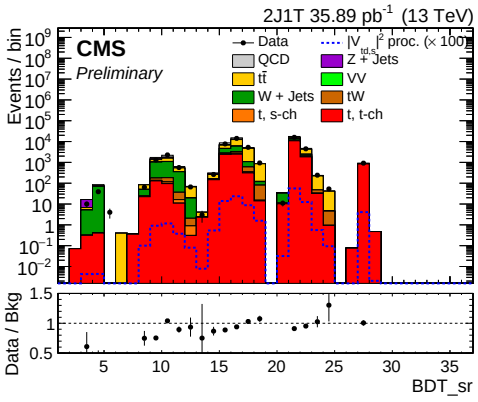

Figure 5.13: Stack of the variable obtained by the combination of the two BDTs in the 2-jets–1-tag for the QCD-depleted-forward region.

jets–2-tags region.

The t-channel, $t\bar{t}$, W + jets and QCD, splitted for the muon and the electron case, are floating with a flat prior, all systematic uncertainties are treated as nuisance parameters. The yield of minor backgrounds is left floating with the respective scale uncertainties.

5.7.3 Systematic uncertainties

The measurement of the cross section is affected by various sources of systematic uncertainty. Uncertainties are treated as nuisance parameters, performing an interpolation amongst templates corresponding to the variations of each systematic scenario is performed in order to define a smooth dependence of the likelihood function from each parameter. The following sources of systematic uncertainty are considered:

- **Jet energy scale (JES)**: All reconstructed jet four-momenta in simulated events are simultaneously varied according to the η- and p_{T}-dependent uncertainties in the JES [62]. This variation in jet four-momenta is also propagated to $\not{p}_{\mathrm{T}}$.
- **The b tagging**: b tagging and misidentification efficiencies are estimated from control samples in 13 TeV data [63]. Scale factors are applied to the simulated samples to reproduce efficiencies observed in data and the corresponding uncertainties are propagated as systematic uncertainties.
- **Lepton trigger and reconstruction**: Single muon and single electron trigger efficiency and reconstruction efficiency are estimated with a Tag and Probe method [64] from Drell–Yan events in the Z boson mass peak.
- **Pileup**: The uncertainty in the average expected number of pileup interactions is propagated as a source of systematic uncertainty to this measurement by varying the minimum bias cross section by $\pm 5\%$. The effect on the result is found to be negligible and is therefore not considered further.
- **Luminosity**: The integrated luminosity is known with a relative uncertainty of $35.89\ \mathrm{cm}^{-2}\mathrm{s}^{-1} \pm 2.7\%$ [65].
- **Signal modelling**: To estimate the influence of possible mismodelling of the signal process, alternative signal samples are used where the value of the hdamp parameter is halved or doubled.
- **$\mathrm{t\bar{t}}$ modelling**: For the estimation of the uncertainty due to possible mismodelling of the $\mathrm{t\bar{t}}$ background, the same procedure as for the signal modelling is applied. Alternative signal samples are used where the value of the hdamp parameter is halved or doubled.
- **Renormalisation and factorisation scale uncertainty ($\mu_{\mathrm{R}}/\mu_{\mathrm{F}}$)**: The uncertainties due to variations in the renormalisation and factorisation scales are studied for the signal process, tW, $\mathrm{t\bar{t}}$, and $\mathrm{W}+\mathrm{jets}$ by reweighting the distributions with different combinations of halved/doubled factorisation and renormalisation scales. The effect is estimated for each process separately.
- **PDF**: The uncertainty due to the choice of PDFs is estimated using reweighted histograms derived from all PDF sets of NNPDF 3.0 [66].

Several of the experimental sources of uncertainty are treated as nuisance parameters in the fit which results in a single uncertainty of the fit including also the statistical

contribution. By fixing all nuisance parameters the statistical uncertainty can be obtained, including the uncertainty due to the size of the samples of simulated events. The contribution due to the profiled experimental uncertainties is derived by subtracting the statistical term quadratically from the fit uncertainty.

5.8 Fit results and interpretation

The fit results are returned in term of *signal strength* μ defined as the ratio of the value of the fitted parameter before and after the fit. Table 5.11 shows the values of the central value and uncertainty on nuisance parameters ("pulls") with pseudo-data for any nuisance parameter, the ratio of error in the model before and after the fit and the correlation coefficient ρ between the signal strength μ and each nuisance parameter. The shift between the value of the parameter before and after the fit is referred to as Δx and the error in the model before and after the fit is referred to as σ_{in} and σ_{out}, respectively.

Table 5.11: Pulls with pseudo-data for any nuisance parameter, the ratio of error in the model before and after the fit and the correlation coefficient ρ between the signal strength μ and each nuisance parameter.

Systematic uncertainty	b-only fit		$b+s$ fit		$\rho(\theta\mu)$
	$\Delta x/\sigma_{\text{in}}$	$\sigma_{\text{out}}/\sigma_{\text{in}}$	$\Delta x/\sigma_{\text{in}}$	$\sigma_{\text{out}}/\sigma_{\text{in}}$	
b-tagging efficiency	+0.32	0.16	+0.24	0.17	+0.1953
t-channel modelling	+0.24	0.10	+0.24	0.10	+0.0023
$\mathrm{t\bar{t}}$ modelling	-0.51	0.06	-0.51	0.06	-0.0049
JES	-0.29	0.04	-0.29	0.04	-0.0161
lepton efficiency	-0.40	0.40	-0.42	0.40	+0.0168
luminosity	-0.76	0.93	-0.75	0.90	-0.0059
mistagging	-1.88	0.93	-1.84	0.93	-0.0118
PDF	+1.18	0.54	+1.17	0.54	+0.0104
μ_F t-channel	-0.38	0.09	-0.38	0.09	+0.0047
μ_F $\mathrm{t\bar{t}}$	-0.04	0.13	-0.04	0.13	+0.0098
pile up	-5.25	0.63	-5.22	0.63	-0.0173
μ_R t-channel	+1.55	0.44	+1.56	0.44	-0.0008
μ_R t-channel s/d	+0.01	0.99	-0.00	0.99	+0.0023
μ_R $\mathrm{t\bar{t}}$	+0.86	0.26	+0.86	0.26	+0.0002
μ_R W + jets	+1.93	0.15	+1.94	0.15	-0.0288

In Figure 5.14 are plotted the same parameters reported in the Table 5.11.

Figures 5.15 and 5.16 show the distributions of the MVA variables in the different

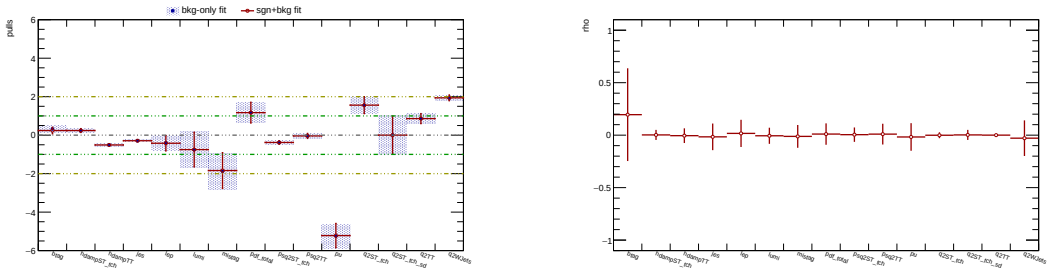

(a) (b)

Figure 5.14: Pulls with pseudo-data for each nuisance parameter and the correlation coefficient between the signal strength μ and for each nuisance parameter.

regions obtained after the fit for the muon and electron channels. The scale factor post/pre fit for the single top quark t-channel produced via and decaying to b quarks is:

$$\mu_{ST_{\mathrm{b,b}}} = 1.05 \pm 0.02.$$

For the single top quark t-channel decaying to, or produced via s/d quarks the fit returns the scale factor:

$$\mu_{ST_{\mathrm{b,q}}} < 5.02 \,\text{at}\, 95\%\,\text{C.L},$$

with an expected value of:

$$\mu^{exp}_{ST_{\mathrm{b,q}}} = 4.70.$$

By exploiting the relations:

$$\frac{\sigma^{\mathrm{obs}}_{t-\mathrm{ch.,b}} \times \mathrm{BR(t \to Wb)^{obs}}}{\sigma_{t-\mathrm{ch.,b}} \times \mathrm{BR(t \to Wb)}} = |\mathrm{V_{tb}}|^4 \tag{5.11}$$

$$\frac{\sigma^{\mathrm{obs}}_{t-\mathrm{ch.,b}} \times (\mathrm{BR(t \to Wd,s)})^{\mathrm{obs}}}{\sigma_{t-\mathrm{ch.,b}} \times (\mathrm{BR(t \to Wd,s)})} = \frac{(|\mathrm{V_{td}}|^2 + |\mathrm{V_{ts}}|^2)^{\mathrm{obs}}(|\mathrm{V_{tb}}|^2)^{\mathrm{obs}}}{(|\mathrm{V_{td}}|^2 + |\mathrm{V_{ts}}|^2)|\mathrm{V_{tb}}|^2} \tag{5.12}$$

$$\frac{\sigma^{\mathrm{obs}}_{t-\mathrm{ch.,s,d}} \times (\mathrm{BR(t \to Wb)})^{\mathrm{obs}}}{\sigma_{t-\mathrm{ch.,s,d}} \times (\mathrm{BR(t \to Wb)})} = \frac{(|\mathrm{V_{td,s}}|^2)^{\mathrm{obs}}(|\mathrm{V_{tb}}|^2)^{\mathrm{obs}}}{(|\mathrm{V_{td,s}}|^2)|\mathrm{V_{tb}}|^2} \tag{5.13}$$

$$\frac{\sigma^{\mathrm{obs}}_{\mathrm{t\bar{t}}} \times (\mathrm{BR(t\bar{t} \to WbWd,s)})^{\mathrm{obs}}}{\sigma_{\mathrm{t\bar{t}}} \times (\mathrm{BR(t\bar{t} \to WbWd,s)})} = \frac{(|\mathrm{V_{td}}|^2 + |\mathrm{V_{ts}}|^2)^{\mathrm{obs}}(|\mathrm{V_{tb}}|^2)^{\mathrm{obs}}}{(|\mathrm{V_{td}}|^2 + |\mathrm{V_{ts}}|^2)|\mathrm{V_{tb}}|^2}, \tag{5.14}$$

the results in terms of signal strength obtained in the fit procedure are converted in term

of results for the elements of CKM matrix, resulting in:

$$|V_{tb}| = 1.010 \pm 0.005 \tag{5.15}$$

$$|V_{tb}|^2 = 1.021 \pm 0.010 \tag{5.16}$$

$$|V_{ts}|^2 + |V_{td}|^2 \leq 0.009 \,\text{at}\, 95\% \,\text{C.L.} \tag{5.17}$$

The best estimation for the magnitude of the CKM matrix elements is the one obtained by the global fit of the SM:

$$|V_{tb}|^2 = 0.998239^{+0.000048}_{-0.000024} \quad |V_{ts}|^2 = 0.0016876^{+0.0000025}_{-0.0000047} \quad |V_{td}|^2 = 0.000074^{+0.000013}_{-0.000017}.$$

When $|V_{td}|^2$ and $|V_{ts}|^2$ are summed together one obtains:

$$|V_{td}|^2 + |V_{ts}|^2 = 0,0017611^{+0.0000028}_{-0.0000050}$$

The results obtained are in agreement with the estimations of the global fit of the SM and there is no significant deviations from the SM.

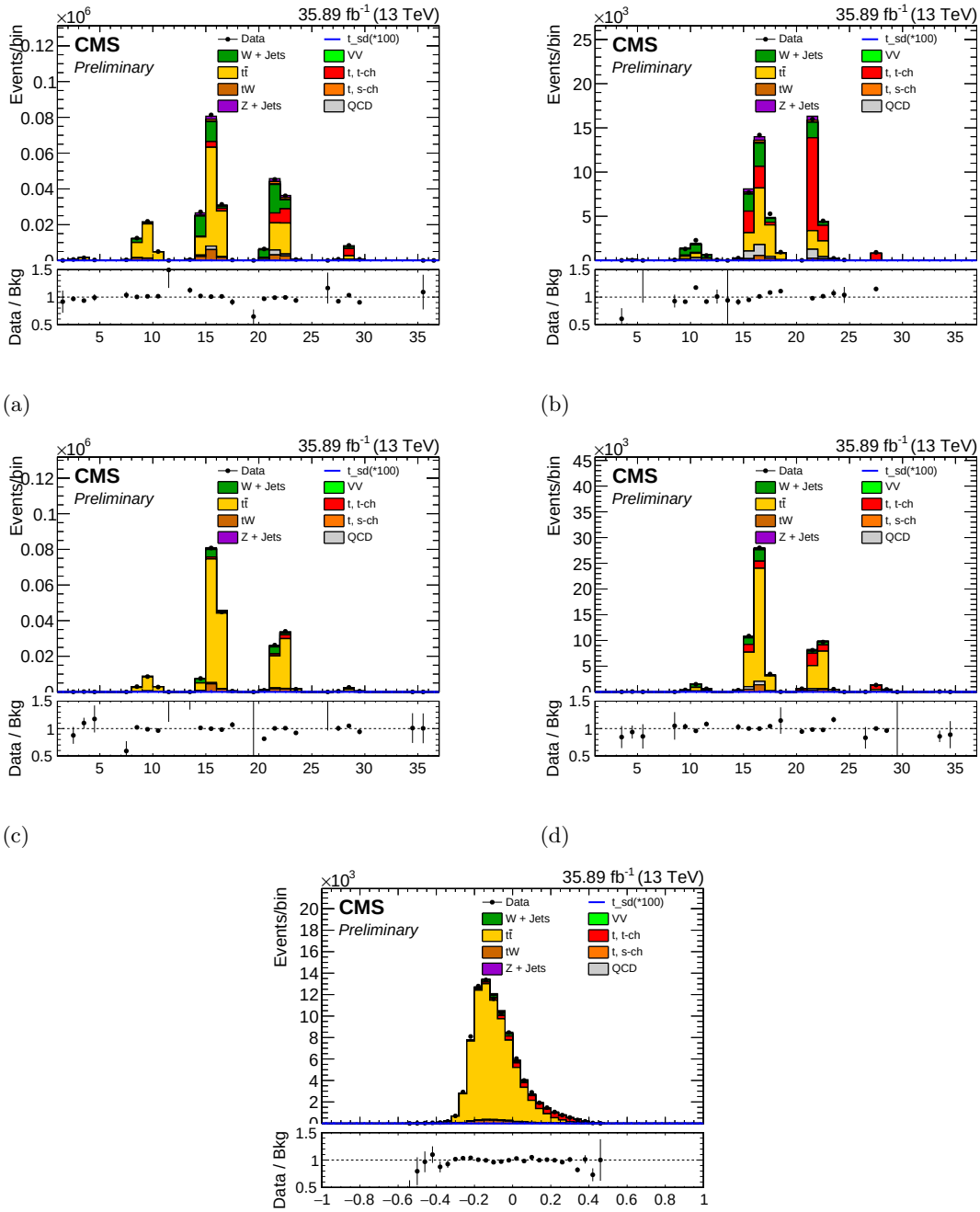

Figure 5.15: Stacks obtained after the fit procedure for muon channel: (a) shows the QCD-depleted-central region for the 2-jets–1-tag region, (b) shows the QCD-depleted-forward region for the 2-jets–1-tag region, (c) shows the QCD-depleted-central region for the 3-jets–1-tag region, (d) shows the QCD-depleted-forward region for the 3-jets–1-tag region and (e) shows the 3-jets–2-tags region.

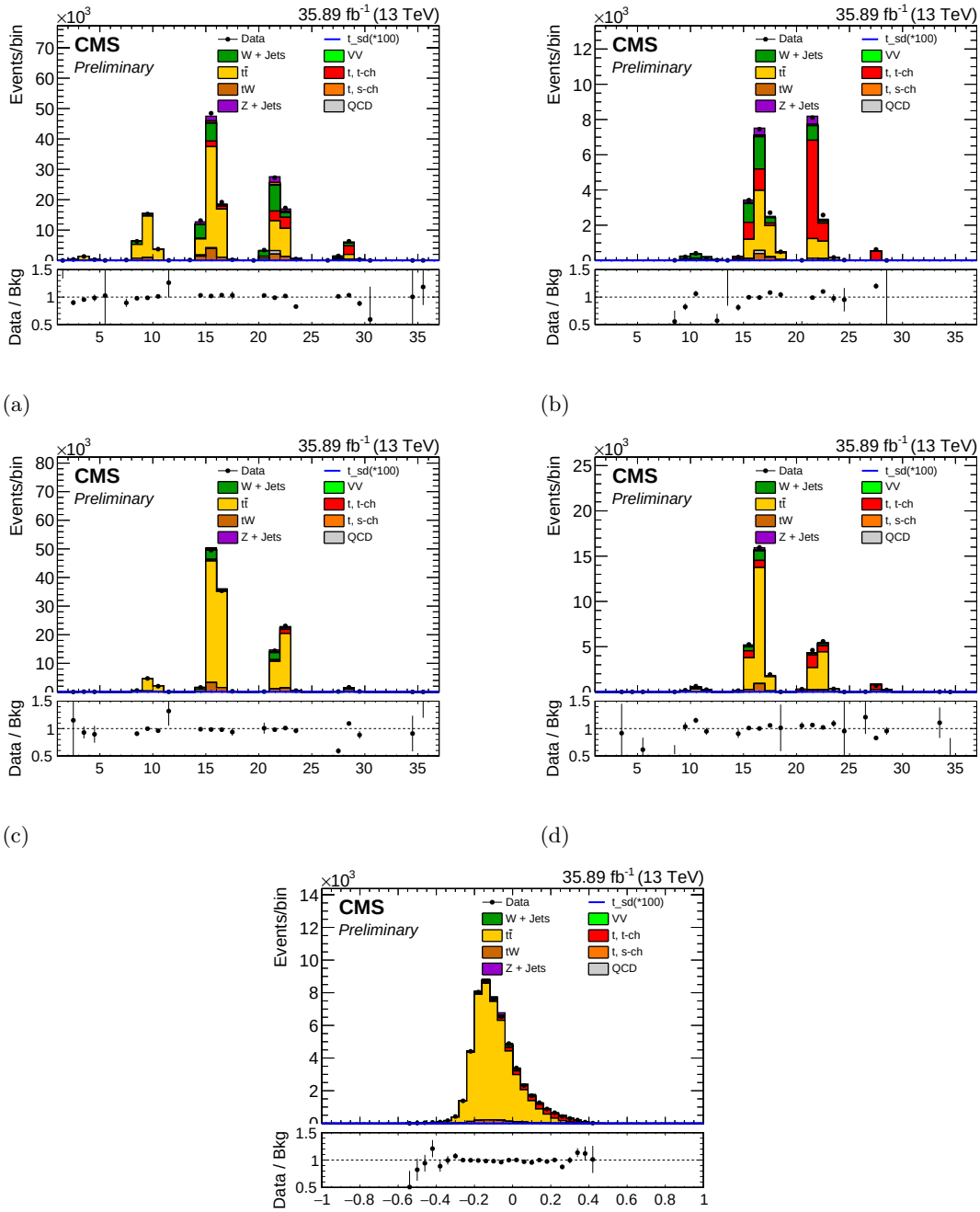

Figure 5.16: Stacks obtained after the fit procedure for electron channel: (a) shows the QCD-depleted-central region for the 2-jets–1-tag region, (b) shows the QCD-depleted-forward region for the 2-jets–1-tag region, (c) shows the QCD-depleted-central region for the 3-jets–1-tag region, (d) shows the QCD-depleted-forward region for the 3-jets–1-tag region and (e) shows the 3-jets–2-tags region.

Conclusions

In this thesis it is presented the first direct measurement of the Cabibbo-Kobayashi-Maskawa matrix elements $|V_{tb}|$, $|V_{ts}|$, and $|V_{td}|$, making use of single top quark t-channel events in proton-proton collision data with a centre-of-mass energy of 13 TeV, collected with the CMS experiment at the LHC. The subset of data analysed corresponds to an integrated luminosity of 35.89 fb^{-1}.

The dominant electroweak production mechanism for single top quarks is the t-channel and it features a tWq vertex, where q stands for b, s or d quarks, both in production and in decay. For this reason its cross section and branching fractions are sensitive to the strength of the electroweak coupling, making it a suitable channel for direct measurements of the magnitude of Cabibbo-Kobayashi-Maskawa matrix elements $|V_{tb}|$, $|V_{ts}|$, and $|V_{td}|$. A precise determination of the magnitude of these parameters of the Standard Model allows to search for hints of potential contributions from new physics beyond the Standard Model.

In the present analysis, a selection is performed by requiring one isolated lepton, muon or electron and two or three jets, one or two of which must pass the b-tagging requirement. The events are distinguished into three different categories according to the number of jets and b tagged jets. The signal is composed of single top t-channel produced via or decaying to s/d quarks and $t\bar{t}$ one of them decaying to s/d quarks. A data driven estimation technique is applied to obtain the QCD-multijets contribution directly from data.

For a further optimisation of the discrimination between signal and backgrounds the data set is divided into two regions, characterized by different event topologies for the categories with one b-jet. In each of these regions a multivariate analysis is performed in order to fully exploit the most important kinematic variables.

A simultaneous maximum likelihood fit to the multivariate distributions in all categories is performed in order to extract $|V_{tb}|^2$ and $|V_{ts}|^2 + |V_{td}|^2$. The results obtained with the

analysis presented are:

$$|V_{tb}| = 1.010 \pm 0.005 \qquad |V_{td}|^2 + |V_{ts}|^2 \leq 0.009 \text{ at } 95\% \text{ C.L.},$$

and no significant deviation from the prior Standard Model expectations is observed. This measurement could be improved by including the data to be collected by CMS during the full Run II at 13 TeV, thus increasing the data sample and improving the determination of the systematics, currently extracted in-situ from the data. Additionally, one could focus on the study of orthogonal samples to improve the determination of the main systematics, like the b-tagging. Finally, another improvement could be inclusion in the fit of direct constraints amongst the different Cabibbo-Kobayashi-Maskawa matrix elements $|V_{tb}|$, $|V_{ts}|$, and $|V_{td}|$ to allow for a wide variety of possible hypotheses to be tested.

Acknowledgements

Another chapter of my life ends today. This master thesis is the terminal of my master studies that had been very difficult to me. Luckily I had many people who supported me every day in each my weakness. I want to spend some lines to thank them all.

First of all, I'd like to thank my parents, without them I would not be here. They support me in each my choices by inciting me to do my best. I'd like also to thank my sisters, always present in all my decisions. This work is dedicated to them.

I'd like to thank Flavia, who is victim of my insanity every day but she is always ready to stand by me. I'm sure that I couldn't succeed in it without her.

I'd like to thank Orso, supervisor of this work, who is for me a guide and an example to follow. His help is not limited to this master thesis but he is always helpful in every situation and ready to give good advice.

I'd like to thank also Dr. Lista, Dr. Tramontano and Wajid for their proficient advice given to me during the writing of this thesis.

I can't forget all my friends of the study room $\hbar$ with whom I studied and I had fun.

Finally, I'd like to thank my flatmates, who made the cohabitation pleasant and who had been always helpful.

Bibliography

[1] S. Glashow, "Partial-symmetries of weak interactions", Nuclear Physics, 22:579-588, (1961).

[2] S. Weinberg, "A model of leptons", Phys. Rev. Lett., 19:1264-1266, (1967).

[3] A. Salam, N. Svalthrom ed., "Elementary particle theory: relativistic groups and analyticity", Nobel symposium. (1968)

[4] F. Englert and R. Brout, "Broken Symmetry and the Mass of Gauge Vector Mesons", Phys. Rev. Lett., 13:321-323, (1964).

[5] P.W. Higgs, "Broken Symmetries and the Masses of Gauge Bosons", Phys. Rev. Lett., 13:508-509, (1964).

[6] G.S. Guralnik, C.R. Hagen and T.W.B. Kibble, "Global Conservation Laws and Massless Particles", Phys. Rev. Lett., 13: 585–587, (1964).

[7] G. Zweig, "An SU(3) model for strong interaction symmetry and its breaking", Technical Report CERN-TH-401, CERN, Geneva, (1964).

[8] M.Y. Han and Y. Nambu, "Three-triplet model with double SU(3) symmetry", Phys. Rev., 139:B1006-B1010, (1965).

[9] O.W. Greenberg, "Spin and Unitary Spin Independence in a Paraquark Model of Baryons and Mesons", Phys. Rev. Lett., 13:598-602, (1964).

[10] H.D. Politzer, "Reliable perturbative results for strong interactions", Phys. Rev. Lett., 30:1346–1349, (1973).

[11] D.J. Gross and F. Wilczek, "Ultraviolet behavior of non-abelian gauge theories", Phys. Rev. Lett., 30:1343–1346, (1973).

[12] G. Arnison et al., Phys.Lett. 122B (1983) 103; 126B 398, (1983).

[13] M. Banner et al., Phys. Lett. 122B 476, (1983).

[14] P. Bagnaia et al., Phys. Lett. B129 130, (1983).

[15] Abe F. et al, CDF Collaboration, Phys Rev. D50 2966 and Phys. Rev. Lett. 73 225, (1994).

[16] ATLAS Collaboration, "Observation of a new particle in the search for the Standard Model Higgs boson with the ATLAS detector at the LHC". Phys.Lett.B, (2012).

[17] CMS Collaboration, "Observation of a new boson at a mass of 125 GeV with the CMS experiment at the LHC". Phys.Lett.B, (2012).

[18] P. Langacker, "Introduction to the Standard Model and Electroweak Physics", Phys.Lett. High Energy Physics-Phenomenology, (2009), `http://arxiv.org/abs/0901.0241`.

[19] C. Jarlskog, Phys. Rev. Lett. 55, 1039 (1985).

[20] The CKMfitter Group, "Updated results on the CKM matrix", ICHEP (2016).

[21] W.J. Marciano and A. Sirlin, Nucl. Phys. B93, 303 (1975).

[22] K.S. Babu, Z. Phys. C35, 69 (1987).

[23] "LHC machine", Journal of Instrumentation 3 no.8, (2008) S08001. `http://iopscience.iop.org/1748-0221/3/08/S08001`.

[24] CMS collaboration, "The CMS tracker system project: technical design report", CERN-LHCC-98-006, `http://cdsweb.cern.ch/record/368412`.

[25] CMS collaboration, "The CMS tracker: addendum to the technical design report", CERN-LHCC-2000-016, `http://cdsweb.cern.ch/record/490194`.

[26] PARTICLE DATA GROUP collaboration, S. Eidelman et al., "Review of particle physics", Phys. Lett. B 592 (2004) 1.

[27] F. Kircher et al., "Final design of the CMS solenoid cold mass", IEEE Trans. Appl. Supercond., 10 (2000) 407.

[28] CMS collaboration, "The TriDAS project, technical design report. Volume 1: The level-1 trigger", CERN-LHCC-2000-038, `http://cdsweb.cern.ch/record/706847`.

[29] CMS collaboration, "The TriDAS project, technical design report. Volume 2: Data acquisition and high-level trigger technical design report", CERN-LHCC-2002-026, http://cdsweb.cern.ch/record/578006.

[30] The ATLAS, CDF, CMS, D0 Collaborations, "First combination of Tevatron and LHC measurements of the top-quark mass", http://arxiv.org/abs/1403.4427, (2014).

[31] M. Czakon, P. Fiedler, and A. Mitov, "The total top quark pair production cross-section at hadron colliders through $\mathcal{O}(\alpha_s^4)$", Phys. Rev. Lett. 110 252004, https://arxiv.org/abs/1303.6254, (2013).

[32] M. Brucherseifer, F. Caola, and K. Melnikov, "On the NNLO QCD corrections to single-top production at the LHC", Phys. Lett. B 736 58–63, https://doi.org/10.1016/j.physletb.2014.06.075, https://arxiv.org/abs/1404.7116 (2014).

[33] N. Kidonakis, "Top Quark Production", https://arxiv.org/abs/1311.0283v1, (2013).

[34] J. Alwall et al., "MadGraph 5: Going Beyond", JHEP 06 128, https://arxiv.org/abs/1106.0522, (2011).

[35] E. Re, "Single-top Wt-channel production matched with parton showers using the POWHEG method", Eur. Phys. J. C71 1547, https://arxiv.org/abs/1009.2450, (2011).

[36] S. Alioli, P. Nason, C. Oleari, and E. Re, "A general framework for implementing NLO calculations in shower Monte Carlo programs: the POWHEG BOX", JHEP 06 043, https://arxiv.org/abs/1002.2581, (2010).

[37] S. Alioli, P. Nason, C. Oleari, and E. Re, "NLO single-top production matched with shower in POWHEG: s- and t-channel contributions", JHEP 09 111, https://arxiv.org/abs/0907.4076, (2009)

[38] S. Frixione, P. Nason, and C. Oleari, "Matching NLO QCD computations with Parton Shower simulations: the POWHEG method", JHEP 0711 070, https://arxiv.org/abs/0709.2092, (2007) .

[39] CMS collab., Phys. Lett. B 736 (2014) 33.

[40] V.M. Abazov et al. (D0 Collab.), Phys. Rev. Lett. 98, 041801 (2007).

[41] T. Aaltonen et al. (CDF Collab.), Phys. Rev. D88, 032003 (2013).

[42] G. Aad et al. (ATLAS Collab.), JHEP 11, 031 (2011).

[43] CMS Collab., CMS-PAS-TOP-11-031 (2011).

[44] V.M. Abazov et al. (D0 Collab.), Phys. Lett. B702, 16 (2011).

[45] CDF Collab., CDF conference note 10211 (2010).

[46] G. Aad et al. (ATLAS Collab.) Phys. Rev. D90, 112016 (2014).

[47] CMS Collab., CMS PAS TOP-13-015 (2013).

[48] CMS collaboration, "Measurement of top quark polarisation in t-channel single top quark production", `https://arxiv.org/abs/1511.02138`, (2016).

[49] A. Czarnecki, J.G. Korner and J.H. Piclum, "Helicity fractions of W bosons from top quark decays at NNLO in QCD", Phys. Rev. D 81 111503 `https://arxiv.org/abs/1005.2625`,(2010).

[50] The D0 Collaboration, "Measurement of the W boson helicity in top quark decays using 5.4 fb^{-1} of $\text{p}\bar{\text{p}}$ collision data", Phys. Rev. D83 032009, `https://arxiv.org/abs/1011.6549`, (2011).

[51] The CDF Collaboration, "Measurement of W-Boson Polarization in Top-quark Decay in $\text{p}\bar{\text{p}}$ Collisions at $\sqrt{s} = 1.96$ TeV", Phys. Rev. Lett. 105 042002, `https://arxiv.org/abs/1003.0224`, (2010).

[52] ATLAS Collab., JHEP 1206, 088 (2012).

[53] CMS collaboration, "Measurement of the W boson helicity in events with a single reconstructed top quark in pp collisions at $\sqrt{s} = 8$ TeV", JHEP 04 073, `https://arxiv.org/abs/1410.1154`, (2015).

[54] CMS Collaboration, "Particle–Flow Event Reconstruction in CMS and Performance for Jets, Taus, and $\not{E}_{\text{T}}$ ", CMS Physics Analysis Summary CMS-PAS-PFT-09-001, (2009).

[55] M. Cacciari, G. P. Salam, and G. Soyez, "The anti-k_{T} jet clustering algorithm", JHEP 04 063, `https://arxiv.org/abs/0802.1189`, (2008)

[56] T. C. collaboration, "Determination of jet energy calibration and transverse momentum resolution in CMS", Journal of Instrumentation 6, no. 11, P11002, (2011).

[57] Chatrchyan, S. and others, CMS Collaboration, "Measurement of the single-top-quark t-channel cross section in pp collisions at $\sqrt{s} = 7$ TeV", JHEP 12 035, `https://arxiv.org/abs/1209.4533`, (2012).

[58] Chatrchyan, S. and others, CMS Collaboration, "Measurement of the t-channel single-top-quark production cross section and of the $|V_{tb}|$ CKM matrix element in pp collisions at $\sqrt{s} = 8$ TeV", JHEP 06 090, `https://arxiv.org/abs/1403.7366`, (2014).

[59] Chatrchyan, S. and others, CMS Collaboration, "Cross section measurement of t-channel single top quark production in pp collisions at $\sqrt{s} = 13$ TeV", Phys. Lett. B 772 752, `https://doi.org/10.1016/j.physletb.2017.07.047`, (2017).

[60] A. Hoecker, P. Speckmayer, J. Stelzer, J. Therhaag, E. von Toerne, and H. Voss, "TMVA: Toolkit for Multivariate Data Analysis", PoS A CAT 040, `https://arxiv.org/abs/physics/0703039`, (2007).

[61] L. Moneta et al., "The RooStats Project", in 13^{th} *International Workshop on Advanced Computing and Analysis Techniques in Physics Research* (ACAT2010). SISSA, `https://arxiv.org/abs/1009.1003`, (2010).

[62] CMS Collaboration, "Determination of jet energy calibration and transverse momentum resolution in CMS", JINST 6 P11002, `https://arxiv.org/abs/1107.4277`, (2011) .

[63] CMS Collaboration, "Identification of b quark jets at the CMS Experiment in the LHC Run 2", CMS Physics Analysis Summary CMS-PAS-BTV-15-001, CERN, `http://cds.cern.ch/record/2138504`, (2015).

[64] CMS Collaboration, "Measurements of inclusive W and Z Cross Sections in pp Collisions at $\sqrt{s} = 7$ TeV", JHEP 01 080, (2011).

[65] CMS Collaboration, "Cms luminosity based on pixel cluster counting – summer 2013 update", CMS Physics Analysis Summary CMS-PAS-LUM-13-001, `https://arxiv.org/abs/1012.2466.`, (2013).

[66] M. Botje et al., "The PDF4LHC Working Group interim recommendations", `https://arxiv.org/abs/1101.0538`, (2011).